

**MEMBRANE-BASED TECHNOLOGIES FOR SALINITY  
GRADIENT POWER HARVESTING: ADVANCED MEMBRANES  
DEVELOPMENT**

A Dissertation  
Presented to  
The Academic Faculty

by

Haiping Gao

In Partial Fulfillment  
of the Requirements for the Degree  
Doctor of Philosophy in the  
School of Civil and Environmental Engineering

Georgia Institute of Technology

December 2019

**COPYRIGHT © 2019 BY HAIPING GAO**

**MEMBRANE-BASED TECHNOLOGIES FOR SALINITY  
GRADIENT POWER HARVESTING: ADVANCED MEMBRANES  
DEVELOPMENT**

Approved by:

Dr. Yongsheng Chen, Advisor  
School of Civil and Environmental  
Engineering  
*Georgia Institute of Technology*

Dr. Ching-Hua Huang  
School of Civil and Environmental  
Engineering  
*Georgia Institute of Technology*

Dr. John Crittenden  
School of Civil and Environmental  
Engineering  
*Georgia Institute of Technology*

Dr. Shuman Xia  
School of Mechanical Engineering  
Georgia Institute of Technology

Dr. Xing Xie  
School of Civil and Environmental  
Engineering  
*Georgia Institute of Technology*

Dr. Zhaohui Tong  
School of Agricultural and Biological  
Engineering  
*University of Florida*

Date Approved: August 22, 2019

*To my parents who has been the most supportive during my years of effort.*

*I love you all, forever.*

## ACKNOWLEDGEMENTS

First, I would like to express my great gratitude to my thesis advisor, Dr. Yongsheng Chen, who offered me the invaluable opportunity to kick off my Ph.D. journey at Georgia Tech. His precious and detailed guidance, support, and mentoring throughout my years of study has brought this thesis to fruition. His pertinent advice and guidance on my career development are also sincerely appreciated.

I would also like to thank my committee members Dr. John Crittenden, Dr. Ching-Hua Huang, Dr. Xing Xie and Dr. Zhaohui Tong for their time and precious comments on my research. I also express my special thanks to Dr. Guangxuan Zhu for his help on equipment training and technical assistance in the lab. Specially, I want to thank the China Scholarship Council (CSC) for partially financial support during my graduate studies.

My thanks go to my friends Jing Qiao, Xuan Zhang, Yajie Qian, Sujin Guo and Yamin Zhou for all the precious caring and help in my life. It's so grateful for every second I get to experience with you all. I also greatly appreciate my colleagues and collaborators, Bopeng Zhang, Xin Tong, Chunyan Xu, Liqing Yan, Lan Gan, Su Liu, Moyosore Afolabi, Thomas Igou, Wensi Chen, and Wenlong Zhang for their persistent help on my research. These amazing people made my Ph.D. journey much easier.

Last but foremost, my biggest thanks and deepest love go to my parents and my lovely sisters for all the love, support, guidance and laughter throughout my whole life. I truly wouldn't be the same without my family. I feel so blessed to have them with me through the hardest times and the happiest times. Without them, I cannot be where I am right now.

# TABLE OF CONTENTS

<b>ACKNOWLEDGEMENTS</b>	<b>iv</b>
<b>LIST OF TABLES</b>	<b>viii</b>
<b>LIST OF FIGURES</b>	<b>ix</b>
<b>LIST OF ABBREVIATIONS</b>	<b>xiii</b>
<b>SUMMARY</b>	<b>xvi</b>
<b>CHAPTER 1. INTRODUCTION</b>	<b>1</b>
1.1. Salinity gradient power	1
1.2. Reverse Electrodialysis	2
1.3. Pressure retarded osmosis	6
<b>CHAPTER 2. RESEARCH OBJECTIVES</b>	<b>10</b>
2.1. Research Objectives	10
2.2. Dissertation Overview	11
2.3. Originality and Merit of the Research	12
<b>CHAPTER 3. PERMSELECTIVITY AND CONDUCTIVITY OF CATION EXCHANGE MEMBRANES: A PERCOLATION SIMULATION OF MASS TRANSPORT</b>	<b>14</b>
3.1. Abstract	14
3.2. Introduction	15
3.3. Model Development	17
3.3.1. Simplified three-phase model	17
3.3.2. Percolation theory and microstructure simulation	21
3.3.3. Membrane Conductivity	23
3.3.4. Simulation Methodology	25
3.4. Materials and Methods	27
3.4.1. Materials	27
3.4.2. Preparation of cation exchange membranes	28
3.4.3. Membrane characterizations	29
3.5. Results and discussion	30
3.5.1. Membrane structure and electrochemical properties	30
3.5.2. Solvent-polymer interaction implication	31
3.5.3. Validation of implementation	34
3.5.4. Simulation of the effect of membrane thickness on permselectivity	36
3.5.5. Simulation of membrane thickness influence on membrane conductance	38
3.6. Conclusion	39

<b>CHAPTER 4. MONOVALENT - ANION SELECTIVE AND ANTIFOULING POLYELECTROLYTES MULTILAYER ANION EXCHANGE MEMBRANES FOR REVERSE ELECTRODIALYSIS</b>	<b>41</b>
<b>4.1. Abstract</b>	<b>41</b>
<b>4.2. Introduction</b>	<b>42</b>
<b>4.3. Experimental</b>	<b>45</b>
4.3.1. Materials	45
4.3.2. Surface modification of CJMA-2 membranes	46
4.3.3. Electrochemical properties characterization	47
4.3.4. Transport numbers	49
4.3.5. Antifouling potential	50
4.3.6. RED performance	51
<b>4.4. Results and Discussion</b>	<b>53</b>
4.4.1. Membrane surface characterization	53
4.4.2. Electrochemical properties characterization	58
4.4.3. Antifouling potential	62
4.4.4. Membrane performance in RED	64
4.4.5. Energy conversion efficiency	68
<b>4.5. Conclusions</b>	<b>69</b>
<b>CHAPTER 5. 2D MXENE/GO HYBRID MEMBRANES FOR HIGHLY EFFICIENT OSMOTIC POWER GENERATION</b>	<b>71</b>
<b>5.1. Abstract</b>	<b>71</b>
<b>5.2. Introduction</b>	<b>71</b>
<b>5.3. Experimental Section</b>	<b>75</b>
5.3.1. Materials	75
5.3.2. Fabrication of MXene/GO hybrid membranes	76
5.3.3. Characterization of 2D materials and membranes	77
5.3.4. Determination of membrane transport properties	78
5.3.5. Membrane performance in PRO tests	79
5.3.6. Water flux and the projected power density	81
5.3.7. Determination of antifouling potential of the membranes	83
<b>5.4. Results and discussion</b>	<b>84</b>
5.4.1. Characterization of 2D nanosheets and the membranes	84
5.4.2. Water and salt permeability coefficients of the membranes	88
5.4.3. Water flux and projected PRO power density	90
5.4.4. Antifouling potential of the membranes	94
<b>5.5. Conclusions</b>	<b>97</b>
<b>CHAPTER 6. MAJOR CONCLUSIONS AND FUTURE WORK</b>	<b>99</b>
<b>6.1. Major Conclusions</b>	<b>99</b>
<b>6.2. Future Work</b>	<b>101</b>
<b>APPENDIX A. SUPPORTING INFORMATION FOR CHAPTER 3</b>	<b>103</b>
<b>A.1 Detailed description of membrane characterization</b>	<b>103</b>
A.1.1 Permselectivity and ionic resistance	103
A.1.2 Ion exchange capacity (IEC)	104

<b>A.2</b>	<b>The properties for all the membrane.</b>	<b>106</b>
<b>A.3</b>	<b>Java codes for the Monte Carlo simulation</b>	<b>107</b>
<b>APPENDIX B. SUPPORTING INFORMATION FOR CHAPTER 4</b>		<b>113</b>
<b>B.1</b>	<b>The chemical structures of polyelectrolytes used</b>	<b>113</b>
<b>B.2</b>	<b>Surface zeta potential, membrane area resistance and permselectivity</b>	<b>114</b>
<b>B.3</b>	<b>AFM topography images of the membranes</b>	<b>118</b>
<b>B.4</b>	<b>Current-voltage (<i>I-V</i>) curves and the limiting current density</b>	<b>120</b>
<b>B.5</b>	<b>Transport numbers and measured OCV in a RED system</b>	<b>121</b>
<b>B.6</b>	<b>Energy conversion efficiency</b>	<b>122</b>
<b>APPENDIX C. SUPPORTING INFORMATION FOR CHAPTER 5</b>		<b>124</b>
<b>C.1</b>	<b>The membrane fabrication procedure and testing cell.</b>	<b>124</b>
<b>C.2</b>	<b>The membrane properties and the maximum power density.</b>	<b>126</b>
<b>REFERENCES</b>		<b>129</b>

## LIST OF TABLES

Table 1 - Reported percolation threshold from literature.	21
Table 2 - Hansen solubility parameters.	33
Table 3 - AEMs used in this work.	46
Table 4 - Composition of testing solutions used in RED power density measurements.	52
Table 5 - XPS elemental compositions for the membranes.	55
Table 6 - Surface roughness and contact angle of the membranes under investigation.	56
Table 7 - Transport number ratios for the membranes.	61
Table 8 - The properties for all the membranes.	106
Table 9 - Membrane hydrated thicknesses and permselectivity.	117
Table 10 - The mechanical properties of the membranes.	126
Table 11 - The intrinsic characteristics of the membranes.	126

## LIST OF FIGURES

- Figure 1 - Schematic diagram of a RED stack with two pairs of AEMs and CEMs. The redox pair is  $[\text{Fe}(\text{CN})_6]^{-3} / [\text{Fe}(\text{CN})_6]^{-4}$ . NaCl solutions at two different concentrations are utilized as the concentrated and diluted solutions, respectively. 3
- Figure 2 - Schematic diagram of a laboratory-scale PRO system. Crossflow mode of the feed and draw solutions is employed. 7
- Figure 3 - Schematic of a three-phase model for a charged IEM. 18
- Figure 4 - Simulation of percolation probability as a function of lattice thickness with at least 100 trials at each setting. In these exemplary lattice, width and length are set to 64 with periodic boundary condition, but the thickness varies from 16 to 512. The threshold moves from 0.22 to 0.31, close to the theoretical value of infinite lattice size. 23
- Figure 5 - Schematic of (a). a 3-D lattice and (b). the cross - section for the study of site percolation. Blue sites are defined as open sites and blank sites are closed to ion transport, so total volume of blues sites is the inter-gel phase volume. 27
- Figure 6 - Cross sections of SPPO membrane with (a) NMP, (b) DMF), (c) DMSO as solvents, respectively; and (d). Cross section of a commercial FKS membrane. 31
- Figure 7 - Permselectivity (a) and area resistance (b) for a series of CEMs as a function of membrane hydrated thickness. 34
- Figure 8 - The effect of simulation thickness and simulated inter-gel volume rate on percolative-to-inert volume ratio. (a) Zoomed-in details with void ratio between 0.315 to 0.38 of simulated thickness is from 150 to 5000 units. (b) zoomed-out of same thickness rang and void ratio between 0.315 to 0.8. 35
- Figure 9 - The inverse of permselectivity shows linear relationships to percolative-to-inert volume ratios for SPPO-NMP, SPPO-DMSO, and SPPO-DMF membranes. For commercial FKS membranes, the percolative-to-inert volume ratio remains at zero because all void ratios are below the 0.31 threshold. The FKS membranes are shown overlapping the red rectangle marks. The surface area ratio is defined as the ratio of the number of sites in percolating clusters to the number of sites on the rest of the surface. 37
- Figure 10 - Membrane conductance of SPPO and as a function of thickness. Solid lines are the simulation fitting value from the model. Symbols represent experimental data. 39
- Figure 11 - Schematic setup of a four-cell testing module. 48

Figure 12 - SEM images of cross-sections: (a) original CJMA-2 membrane (magnified 700 ×), (b) CJMA-2-7.5 membrane (magnified 700 ×), and (c) CJMA-2-7.5 membrane (magnified 11.0 k ×).	54
Figure 13 - Surface potential of the membranes as a function of coated bilayers.	58
Figure 14 - Area resistance and intrinsic area resistance of the membranes as a function of the coated bilayers. The dash lines work as the directional visual aids.	60
Figure 15 - Membrane potential as a function of time under fouling condition. The feed solution contained 0.1 M NaCl and 0.25 M SDBS. The applied direct current density was kept constant at 2.5 mA/cm <sup>2</sup> . The dashed arrows work as the directional visual aids. The inserted figure shows the transition times for CJMA-2, ACS and CJMA-2-7.5 membranes, respectively.	63
Figure 16 - Maximum gross power density harvested as a function of different flow rates: (a) pure NaCl solution as feed waters (0.51 M for concentrated feed water and 0.017 M for diluted feed water); (b) NaCl solution with 10 % Na <sub>2</sub> SO <sub>4</sub> as feed waters (total ions concentration of 0.51 M for concentrated feed water and total ions concentration of 0.017 M for diluted feed water).	65
Figure 17 - (a) Open circuit voltage as a function of time; (b) power density as a function of time. Humic acid (10 mg/L) and 10 % Na <sub>2</sub> SO <sub>4</sub> were present in both feed solutions. The feed solutions were supplied at a flow velocity of 0.38 cm/s. The dashed lines work as the directional visual aids.	67
Figure 18 - Energy conversion efficiency of modified membranes and ACS membrane compared to CJMA-2 membrane as a function of the number of bilayers. Solutions with mixtures of 0.05 M NaCl and 0.05 M Na <sub>2</sub> SO <sub>4</sub> were used. The applied current density was 4.0 mA/cm <sup>2</sup> .	69
Figure 19 - The schematic of PRO testing cell.	80
Figure 20 - A schematic diagram of the salt concentration profile across a PRO membrane.	82
Figure 21 - Morphology and structure of the <i>d</i> -Ti <sub>3</sub> C <sub>2</sub> T <sub>x</sub> and GO nanosheets. TEM images of (a) <i>d</i> -Ti <sub>3</sub> C <sub>2</sub> T <sub>x</sub> and (b) GO nanosheets. The HRTEM images of the (c) layers of the <i>d</i> -Ti <sub>3</sub> C <sub>2</sub> T <sub>x</sub> nanosheets and (d) the high crystallinity of the <i>d</i> -Ti <sub>3</sub> C <sub>2</sub> T <sub>x</sub> .	85
Figure 22 - The XPS survey spectra of <i>d</i> -Ti <sub>3</sub> C <sub>2</sub> T <sub>x</sub> and GO nanosheets.	86
Figure 23 - The XRD patterns of (a) MAX phase and <i>d</i> -Ti <sub>3</sub> C <sub>2</sub> T <sub>x</sub> powder and (b) pristine and hybrid MXene/GO membranes.	88
Figure 24 - Water permeability coefficient, A, as a function of (a) <i>d</i> -Ti <sub>3</sub> C <sub>2</sub> T <sub>x</sub> weight percentage in the hybrid membrane at an applied hydraulic pressure of 3.45 bar. (b) varied	

applied hydraulic pressure. For all the membranes, the parameter A was determined through the modified RO cell under crossflow mode. 90

Figure 25 - Water flux ( $J_w$ ) and reverse draw salt flux ( $J_s$ ) of  $d\text{-Ti}_3\text{C}_2\text{T}_x/\text{GO-45}$  and commercial CTA membranes. Tests were performed in an FO cell with effective membrane area of  $1\text{ cm}^2$  and a crossflow velocity of  $27.8\text{ cm s}^{-1}$  with different concentrations of NaCl as the draw solution and DI as the feed solution for 2h. At least three membranes testing were conducted at room temperature. 92

Figure 26 - The projected power density of the  $d\text{-Ti}_3\text{C}_2\text{T}_x/\text{GO-45}$  membrane as a function of the applied hydraulic pressure difference in a PRO system. Different concentrations of NaCl solution worked as draw solution and river water ( $0.0017\text{ M NaCl}$ ) as feed solution. 94

Figure 27 - The antifouling potential of the membrane against (a) the NOM (HA) and (b) the bacterium (*E. coli*). Stage I : The membrane under investigation was first compacted with DI water at 3.45 bar for 2 h to reach a steady water flux. Stage II : The feed solution was switched to an HA solution of 30 ppm, and the filtration was conducted for another 5 h under the same hydraulic pressure difference. Stage III : The fouled membrane was physically cleaned, and the pure DI water filtration was then performed for 1h. 97

Figure 28 - The scheme for membrane conductance distribution on a 3D lattice. 107

Figure 29 - The chemical structures of (a) PSS; and (b) PEI. 113

Figure 30 - Zeta potential of 1 g/L of PSS and 1 g/L of PEI as a function of pH. 114

Figure 31 - AFM images of membrane surface: (a) ACS membrane, (b) pristine CJMA-2 membrane, (c) CJMA-2-2.5 membrane, (d) CJMA-2-3.5 membrane, (e) CJMA-2-4.5 membrane, (f) CJMA-2-5.5 membrane, (g) CJMA-2-7.5 membrane, and (f) CJMA-2-10.5 membrane. 119

Figure 32 - Current-voltage ( $I\text{-}V$ ) curves obtained with mixtures of  $0.05\text{ M NaCl}$  and  $0.05\text{ M Na}_2\text{SO}_4$ . 120

Figure 33 - Time-dependent amounts of  $\text{Cl}^-$  and  $\text{SO}_4^{2-}$  in the diluted compartment, for (a) pristine CJMA-2 membrane, and (b) CJMA-2-7.5 membrane. 121

Figure 34 - Open circuit voltage with pure NaCl ( $0.5\text{ M}$ ) and with NaCl containing 10 % of  $\text{Na}_2\text{SO}_4$  (total concentration of  $0.5\text{ M}$ ) as feed solutions, respectively, under different flow velocities. 122

Figure 35 - The revised RO cell used to determine the membrane water and salt permeability coefficients. 124

Figure 36 - The fabrication procedure of the MXene/GO hybrid membranes. 125

Figure 37 - zeta potential of MXene/GO colloidal solutions as a function of GO contents. 125

Figure 38 - The theoretical power density as a function of applied hydraulic pressure difference. 127

Figure 39 - AFM images of membrane surface roughness (a)  $d\text{-Ti}_3\text{C}_2\text{Tx}/\text{GO}-0$ , (b)  $d\text{-Ti}_3\text{C}_2\text{Tx}/\text{GO}-15$ , (c)  $d\text{-Ti}_3\text{C}_2\text{Tx}/\text{GO}-25$ , (d)  $d\text{-Ti}_3\text{C}_2\text{Tx}/\text{GO}-45$ , and (e)  $d\text{-Ti}_3\text{C}_2\text{Tx}/\text{GO}-60$ . 128

## LIST OF ABBREVIATIONS

SGP	Salinity gradient power
RED	Reverse electrodialysis
PRO	Pressure retarded osmosis
CapMix	Capacitive mixing
IEMs	Ion exchange membranes
AEMs	Anion exchange membranes
CEMs	Cation exchange membranes
ICP	Internal concentration polarization
GO	Graphene oxide
TW	Terawatts
IEC	Ion exchange capacity
DI	Deionized
LBL	Layer by layer
PSS	Poly(styrenesulfonate)

PEI Poly(ethyleneimine)

SDBS Sodium dodecylbenzene sulfonate

AC Alternating current

EIS Electrochemical impedance spectroscopy

OCV Open circuit voltage

CMC Critical micelle concentration

PP Polypropylene

FE-SEM Field emission-scanning electron microscope

XPS X-ray photoelectron spectroscopy

AFM Atomic force microscopy

NOM Natural organic matter

PPO Poly(2,6-dimethyl-1,4-phenyleneoxide)

SPPO Sulfonated poly(2,6-dimethyl-1,4-phenyleneoxide)

SD Swelling degree

DMSO Dimethyl sulfoxide

NMP N-Methyl-2-pyrrolidone

DMF Dimethylformamide

DS Degree of sulfonation

IEC Ion exchange capacity

RO Reverse osmosis

FO Forward osmosis

SWRO Seawater reverse osmosis

AAO Alumina oxide

STEM Scanning transmittance electron microscopy

XRD X-ray diffraction

TFC Thin-film composite

TMP Trans-membrane pressure

HA Humic acid sodium salt

E. coli Escherichia coli

CFU Colony-forming unit

LB Luria-Bertani broth

## SUMMARY

The exploration of clean and renewable energy sources is one of the urgent global challenges to meet our growing energy demand. Salinity gradients have been recognized as a potential renewable energy source that has yet to be well tapped. Upon mixing two solutions with salinity difference, Gibbs free energy is released, which could be harnessed via membrane-based technologies as renewable energy. Reverse electrodialysis (RED) and pressure retarded osmosis (PRO) are two such feasible technologies possess great potential for capturing salinity gradient power (SGP). The objective of this work is to develop different types of membranes desired to the RED and PRO systems for efficient clean and renewable energy harvesting.

In a RED system, the core components are ion exchange membranes (IEMs) including anion exchange membranes (AEMs) and cation exchange membranes (CEMs). AEMs and CEMs are alternatively stacked to generate chemical potential with controlled ions transport through two types of IEM. The properties of IEMs, especially membrane conductivity and permselectivity, play crucial roles on RED system energy generation performance. This work advances the fundamental understanding on the correlation of membrane resistance and permselectivity with membrane microstructure through Monte Carlo simulation and experimental validation. The results suggest a fine-tuning approach on future membrane synthesis with anticipating membrane properties for success of RED power performance.

Most of the studies on RED performance focus on investigating standard IEMs with feed solutions containing only NaCl. However, it has been recognized that RED system

energy output is limited under natural water conditions, specifically the presence of multivalent ions and natural organic matters (NOM). With layer-by-layer (LBL) assembly of positively charged and negatively charged polyelectrolytes at a standard AEMs' surface, we are able to obtain desirable membrane with synergistically enhanced monovalent ion selectivity and anti-organic fouling potential. This work demonstrates the efficacy of LBL optimized AEMs for efficient RED power generation.

Differing from RED system, in a PRO system, the key elements are osmotic-driven membranes rather than IEMs. The progress in PRO power performance has been hampered by the absence of high-performance membranes possessing the essential transport and structural properties. In this work, we have developed freestanding 2D MXene/GO hybrid membranes showing necessary water stability and water permeability. With application of the self-standing, support-free thin membranes, the internal concentration polarization (ICP) is significantly reduced, and, hence, the effective driving force for water permeation largely increases. Consequently, the water flux and power density of the PRO system can be greatly enhanced. What's more, the hybrid thin membranes exhibit improved anti-organic fouling and anti-biofouling potential. The findings of this work shed light on a new platform in designing freestanding heterostructure membranes for advancing large-scale viability of PRO technique.

In summary, this dissertation presents deeper understanding of IEMs performance and advances membranes development for capturing renewable energy from salinity gradients via RED and PRO systems. Computational modeling and simulation results reveal insight into the relationship of IEMs' permselectivity and conductivity with their underlying characteristics. The fundamental study provides better optimization approaches

of high-performance IEMs for RED system. Specifically, most theoretical derivations and model simulations are generic for IEMs, and therefore, can potentially be applied to water desalination processes such as electrodialysis (ED) system. Additionally, the development of multifunctional IEMs and osmotic-driven membranes highlights the promise in large-scale viability of renewable salinity gradient energy harvesting techniques.

# CHAPTER 1. INTRODUCTION

## 1.1. Salinity gradient power

The rapid increasing global energy demands, and environmental issues such as climate change and air pollution caused by prolonged dependence on conventional fossil fuels have stimulated the development of clean and sustainable energy sources as alternatives. So far, remarkable progress has been made in capturing renewable energy from clean and sustainable sources such as solar energy, wind energy, hydrothermal energy, biomass energy, etc. [1]. However, to advance the current renewable energy generation techniques, more efforts are necessary to strive for attractive sustainable energy sources that have been overlooked.

Salinity gradients are such emerging candidates that holds a huge amount of untapped renewable and clean energy with significant low carbon footprint. The salinity gradient power (SGP) can be extracted upon mixing of two solutions with salinity difference [2]. In terms of the natural salinity gradients, SGP can be captured where fresh major rivers flowing into the oceans globally [3]. Alternatively, SGP can also be derived from anthropogenic streams by pairing desalination brine with wastewater treatment effluents [4-8]. Additionally, natural hypersaline waters (e.g., the Deas Sea, the Great Salt Lake and salt domes) are also attractive salinity gradients sources that can offer higher energy output [9, 10]. The technically harvestable SGP from global natural salinity gradients has been estimated to reach 0.983 terawatts [11], which is equivalent to approximately 36.8% of the net electricity production in 2015 worldwide (234,00 TW h). The free energy of mixing is irreversibly lost in entropy if the two solutions are mixed in

an uncontrolled way. Thus, to convert the released free energy to useful work, the controlled mixing is required through engineered energy production processes. Several techniques have been proposed to harvest sustainable energy from salinity gradients, including RED [12, 13], PRO [14, 15], capacitive mixing (CapMix) [16, 17], and nanofluidic osmotic power generators [18], etc. Among all the technologies, membrane-based RED and PRO technologies have been acknowledged as the leading candidates [15, 19].

## **1.2. Reverse Electrodialysis**

The concept of electricity production from mixing fresh and salty water by a RED system was first proposed in 1954 [20]. For a RED system, the core components are IEMs, which are prepared with polymer blocks containing active ion exchange functional groups. In terms of CEMs, the negatively charged functional groups allow the cations to transport across the membrane while repelling the anions. With respect to the AEMs, the positively charged functional groups show inverse ion transport manner in comparison to the CEMs. In RED system, repeating pairs of negatively charged CEMs and positively charged CEMs are alternatively arranged in series to regulate selective ion transport across membranes. In detail, when fresh and salty water are pumped into the RED system continuously, the chemical potential difference drives cations to transport across AEMs from the salty feed water side to the freshwater side, and anions to transport across AEMs from the salty water to the fresh water. Consequently, the net ionic flux is generated through the whole membrane pack. Then, the ionic flux is converted to an electric current via redox reaction occurring at the two end electrodes when introducing an external circuit configured with power-harnessing devices. The schematic of a RED process is shown in Figure 1.

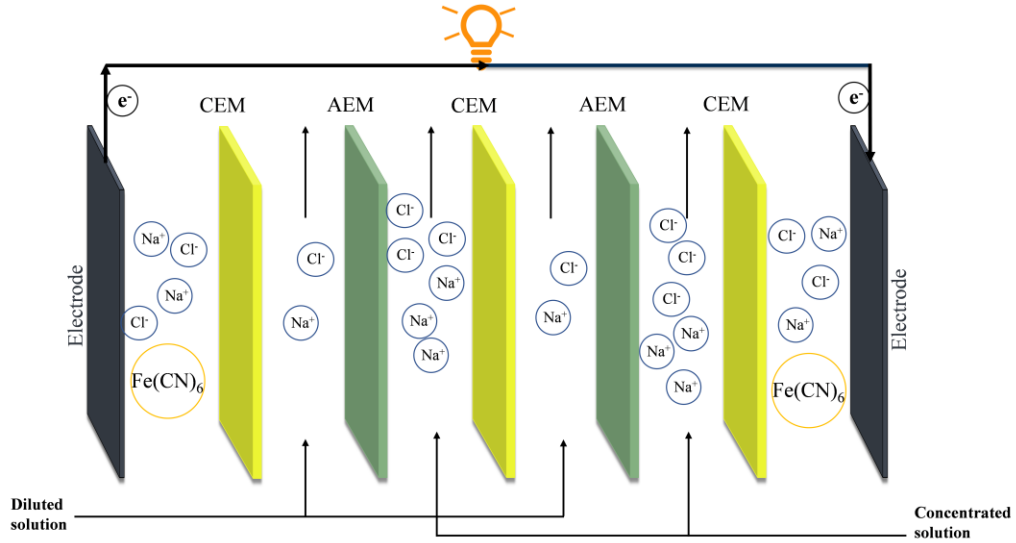


**Figure 1 - Schematic diagram of a RED stack with two pairs of AEMs and CEMs. The redox pair is  $[\text{Fe}(\text{CN})_6]^{-3}/[\text{Fe}(\text{CN})_6]^{-4}$ . NaCl solutions at two different concentrations are utilized as the concentrated and diluted solutions, respectively.**

Considering the IEMs as the key elements in a RED system, the effectiveness and energy efficiency of the system are primarily determined by the IEMs properties including membrane permselectivity, ionic resistance, ion exchange capacity [21] [21], etc. Permselectivity indicates the ability of an IEM to exclude co-ions from permeating across the membrane while allowing counter-ions to pass through. Practically, the apparent permselectivity of a membrane determines the achievable open circuit voltage (OCV) throughout the RED stack under given salinity gradients as following [22]:

$$E_{stack} = N\alpha \frac{RT}{F} \ln\left(\frac{\alpha_c}{\alpha_d}\right) \quad (1)$$

where  $\alpha$  is the apparent permselectivity of a membrane,  $N$  is the total pairs of IEMs used in a RED stack,  $R$  is the gas constant ( $\text{J mol}^{-1}\text{K}^{-1}$ ),  $T$  is the absolute temperature (K), and  $\alpha_c$ ,  $\alpha_d$  are the activities ( $\text{mol L}^{-1}$ ) for the concentrated solution and the diluted solution, respectively.

The gross RED power output is calculated based on the Kirchoff's law as follows:

$$W = I^2 R_L = \frac{E_{stack}^2 R_L}{(R_{stack} + R_L)^2} \quad (2)$$

where  $R_{stack}(\Omega)$  is the overall stack resistance arising from all the components in a RED stack,  $R_L(\Omega)$  is the external load resistance. Thus, the maximized power density is achieved when  $R_{stack}(\Omega)$  is equivalent to  $R_L(\Omega)$  [23]:

$$P_{max} = \frac{E_{stack}^2}{4R_{stack}} \quad (3)$$

The overall  $R_{stack}$  is the summation of resistances rising from all the components in a RED stack with  $N$  pairs of IEMs, which is expressed as [24]:

$$R_{stack} = N(R_m + R_{\Delta C} + R_{DBL}) + R_{electrode} \quad (4)$$

where  $R_m$  is the membrane ionic resistance ascribed to the ions transporting through IEMs,  $R_{\Delta C}$  is the resistance caused by the change in the bulk solution concentration,  $R_{DBL}$  is the diffusion boundary layer resistance in relation to concentration polarization, and  $R_{electrode}$  is the resistance of two electrodes. The contributions of the resistance from different parts to the overall stack resistance have been well investigated by combining theoretical and experimental results in the literatures [25, 26]. It has been clearly suggested that the  $R_{stack}$  largely depends on ionic resistance of the IEMs and resistance from feed solution especially the diluted solution [26].

According to the governing equations abovementioned for RED power density, the membrane permselectivity and ionic resistance are specifically considered as two predominant parameters to maximize the RED power performance. Amounts of research have focused on developing and optimizing IEMs with anticipated properties i.e. low ionic resistance and high permselectivity. However, limited attention has been paid to the fundamental understanding on the correlation of membrane properties with its underlying characteristics and membrane microstructures. A deeper fundamental understanding on membrane properties determining factors would be potentially instructive to future materials selection and development of high-performance IEMs for electrochemical process.

So far, RED system has been intensively investigated with artificial feed solutions containing only NaCl under lab-scale conditions. However, the major salinity gradients for the large-scale application of RED technology come from the natural streams (e.g. river waters and sea water), which contain not only monovalent ions but also multivalent ions. Although the fraction of multivalent ions, such as  $\text{SO}_4^{2-}$ ,  $\text{Mg}^{2+}$ , and  $\text{Ca}^{2+}$ , is relatively less than that of  $\text{Na}^+$  and  $\text{Cl}^-$  in natural waters, their influences on the RED power output are noteworthy [23, 24, 27]. Previous studies have reported that the presence of multivalent ions, especially in a diluted solution, results in a sacrificed open circuit voltage across the membranes and in turn, decreasing power generation [28-31]. This lowering effect can be ascribed to the increased ohmic resistance of RED stack and the uphill transport of multivalent ions, i.e., the transport of multivalent ions against their concentration gradients [28, 29]. Due to the difference in valence, the electromotive force given by the Nernst equation for  $\text{Cl}^-$  is larger than that for  $\text{SO}_4^{2-}$ . Therefore, to maintain the electroneutrality at

both sides of an IEM, one  $\text{SO}_4^{2-}$  transports from the diluted solution side to the concentrated solution side in exchange of two  $\text{Na}^+$  in an opposite direction. Typically, the standard IEMs have no specific selectivity towards monovalent ions, which is unfavorable to the scaling up of RED application. Hence, it is critical to design membranes with the preferential selectivity for monovalent ions while eliminating the permeation of divalent ions. In addition, the field application of the RED system is also limited by membrane fouling, which affects the membrane performance and reduces the effective lifetime of the membrane [32, 33]. Considering the fouling mechanism, AEMs are more prone to membrane fouling triggered by the presence of natural organic matters (NOM). The negatively charged and hydrophobic NOM, such as humic acids, will shield the positively charged groups in AEMs resulting in a decrease of the apparent permselectivity and an increase in the membrane resistance. Consequently, the obtained power output and energy efficiency decreases rapidly when natural sources of feed water are used [32].

### **1.3. Pressure retarded osmosis**

With respect to the working principles, PRO system is fundamentally different with RED system. In a PRO system, water permeation across a semipermeable membrane is driven by the osmotic pressure difference between the concentrated draw solution and the diluted feed solution. An external hydraulic pressure lower than the osmotic pressure difference is applied to pressurize the draw solution. The draw solution volume gets expanded with water permeating through the salt - rejecting membrane from the feed solution side. Then, the useful work can be generated by partially releasing the diluted, pressurized draw solution through a mechanical energy conversion device such as a hydro-turbine. The driving force for water permeation in PRO is the osmotic pressure difference,

which increases almost proportionally to the increased salinity gradients. While, it is not so for RED system with Nernst potential being as the driving force of ions transport. Hence, the PRO system is suitable to take advantage of the greater salinity gradients, whereas the contribution of larger salinity gradients to RED power performance is not remarkable [19]. The schematic of a PRO system is demonstrated in Figure 2.

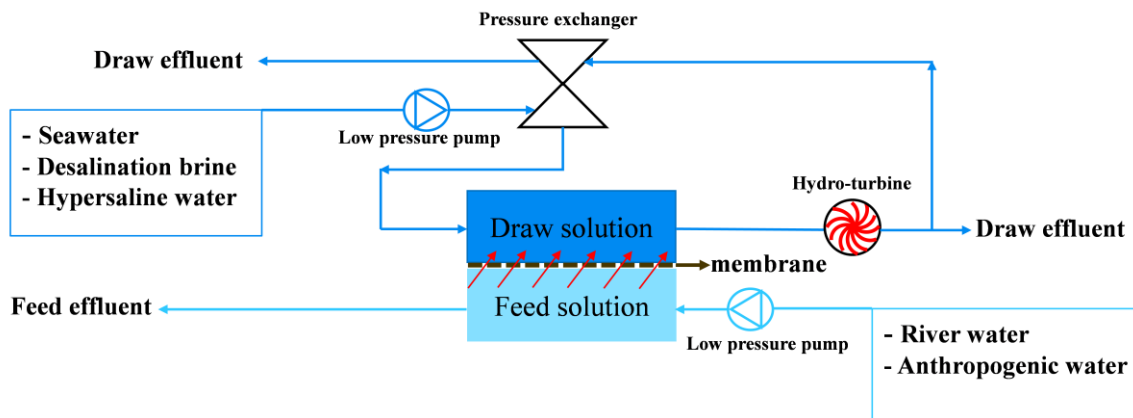


**Figure 2 - Schematic diagram of a laboratory-scale PRO system. Crossflow mode of the feed and draw solutions is employed.**

Theoretically, the obtainable osmotic power is calculated by the product of water flux across a membrane and the applied hydraulic pressure at the draw solution [34]. In a PRO process, the water flux is governed by the transport and structural properties of the membrane [35, 36]. The commonly used PRO membranes are thin-film composite (TFC) flat-sheet and hollow fiber membranes, which consist of a thin active layer and a thick porous support layer [37-41]. In the PRO process, the active layers of TFC membranes are typically placed to face the draw solution and the support layers are facing the feed solution. The draw solution is diluted with water permeating through the support layer from the feed solution, while the reverse diffusion of the draw solute across the support layer to compensate the diluted draw solution [36]. However, the compensating process is largely restricted due to the thick and tortuous support layer of TFC membrane, which results in the internal concentration polarization (ICP) [42, 43]. It has been showed that the ICP is primarily responsible for the relatively low water flux of TFC membranes, especially, at higher concentrations of draw solution. Hence, it is beneficial to develop high performance PRO membranes with minimized ICP. To realize this goal, TFC membranes with thin and highly porous support layers have been fabricated [35, 39]. Although the PRO system with thin TFC membranes showing the power density higher than the commercialization benchmark of  $5 \text{ W m}^{-2}$ , the PRO power performance is still limited by the ICP and the relatively low water permeability [4, 44].

Additionally, membrane fouling also greatly limits the PRO power performance, particularly with wastewater effluents as the feeds [7, 45-47]. With water transporting across the TFC support layer, the foulants as well as the microbials in the feeds are easily trapped inside the porous structure, which leads to dramatical increase in ICP and critical

decrease in effective osmotic driving force for water permeation [48-51]. Therefore, to develop PRO membranes with effective antifouling potential is highly anticipated for the commercialization of PRO application.

## **CHAPTER 2. RESEARCH OBJECTIVES**

Considering the background, the principles and the challenges presented in the previous chapter, I will demonstrate my research objectives and the rationale in this chapter.

### **2.1. Research Objectives**

The overall objective of this work is to advance the reverse electrodialysis (RED) and pressure retarded osmosis (PRO) technologies for gradient power (SGP) harvesting. Throughout the research, the efforts have been focused on developing novel membranes with desired properties that give rise to highly efficient RED and PRO power output. Statistical method based on Monte-Carlo concept is developed to provide guidance for future design of membranes. To realize the viability of large-scale of sustainable energy capturing, membranes exhibiting high-performance under real water conditions are urgently needed. Two-dimensional (2D) materials such as graphene oxide (GO) and emerging class of transition metal carbide (MXene) offer great opportunities in water treatment due to its excellent properties in accelerated water transport and superior ion selectivity. Considering the working principles in the PRO system, the 2D materials hold a great potential in osmotic energy harvesting. Therefore, to strive for harvesting economically attractive SGP, 2D materials-based membranes with more efficient mass transport remains to be explored.

The specific objectives of this dissertation are to:

1. Explore the correlation of ion exchange membranes properties, specifically permselectivity and ionic resistance, with membranes underlying characteristics by statistical simulation coupled with experimental validation.

2. Develop anion exchange membranes (AEMs) rendering monovalent-ions selectivity as well as antifouling potential to achieve considerable RED power output under a complicated water matrix condition closer to the real waters.

3. Take advantages of the unique properties of 2D materials to develop MXene/GO hybrid thin membranes to remarkably minimize the internal concentration polarization (ICP) and greatly accelerate the PRO power output.

## **2.2. Dissertation Overview**

The dissertation is organized into 6 chapters. Chapter 1 introduces the salinity gradients as an emerging clean and renewable energy production source and two leading technologies for SGP harvesting. The performance-determining components and its anticipating properties, the working principles and the remaining challenges are highlighted in this chapter. Chapter 2 specifies the research objectives and the organization of the dissertation.

Chapter 3 explores the relationship between membrane properties and membrane underlying characteristics. The membrane permselectivity and conductivity are successfully modelled on a series of SPPO membranes prepared using three different organic solvents as well as commercial Fumatech FKS membranes. The statistical simulation shows good agreement with the experimental results. In this work, the trend of membrane permselectivity and conductivity varies upon membrane thickness is well explained by combing the three-phase model and the percolation theory. This study offers

potential guidance for future development of IEMs with desired properties for membrane-based technologies.

Chapter 4 demonstrates a study on the fabrication of monovalent-ion selective AEMs by taking advantages of layer-by-layer (LBL) assembly of polyelectrolytes on standard AEMs surface. The physiochemical and electrochemical properties of the membranes have been comprehensively characterized. The ion transport properties and the RED power performance are thoroughly investigated. The results in this work indicate that the LBL modification is a versatile method rendering membranes anticipating properties for more efficient RED power output towards commercialization benchmark.

Chapter 5 develops the freestanding MXene/GO hybrid thin membranes for the PRO system. It turns out that the water flux is largely enhanced, and the resultant power output is significantly increased attribution to the apparent reduction in ICP. In addition, the hybrid membranes with smaller MXene/GO ratio exhibit good stability and improved antifouling potential. This work opens the route to design high-performance membranes showing great application prospects in osmotic-driving process including PRO but not limited to PRO.

Chapter 6 sums up the main findings throughout the research and suggests the perspectives on the future research and the application of membrane-based technologies.

### **2.3. Originality and Merit of the Research**

The studies of this dissertation are original and advance the membrane-based technologies referred to RED and PRO system for SGP production. Specifically, the findings gained throughout the research is dedicated to developing membranes with

satisfying properties for clean and renewable energy harvesting technologies from the following aspects:

1. Tuning the membrane permselectivity and conductivity based on the statistical simulation;

2. Developing monovalent-ion selective membranes with enhanced antifouling potential to satisfy the requirements for practical application of membrane-based technologies;

3. Enabling application viability of advanced materials-based membrane technologies for efficient osmotic energy harnessing.

# **CHAPTER 3. PERMSELECTIVITY AND CONDUCTIVITY OF CATION EXCHANGE MEMBRANES: A PERCOLATION SIMULATION OF MASS TRANSPORT**

## **3.1. Abstract**

Ion exchange membranes (IEMs) have been widely applied in water desalination/separation and sustainable energy generation. In these applications, two of the most important properties of IEMs, ionic conductivity and permselectivity, draw the most attention from researchers. However, a favorable high permselectivity is usually achievable at a sacrifice of membrane conductance, as the latter is a function of membrane thickness. Theoretical guidance is still lacking on where to find the optimized membrane properties in applications that are sensitive to both conductance and permselectivity. In this study, we have proposed a novel modeling and simulation of IEM microstructure and associated the microstructure with membrane permselectivity and conductance. Using open and closed sites to represent the polymeric and interstitial electrolyte phases of the membrane matrix, membrane permselectivity and conductivity can be successfully modeled and simulated on a set of sulfonated poly(2,6,-dimethyl-1, 4-phenylene oxide) (SPPO) membranes prepared using different organic solvents (N-Methyl-2-pyrrolidone, dimethylformamide and dimethyl sulfoxide), and commercial Fumatech FKS membranes. The resulting simulation provides good agreement with experimental observations. Notably, the decrease in permselectivity upon decreasing membrane thickness is well explained by the model considering the combined effects resulting from the membrane void ratio and the percolative states of the lattice structure. When the membrane void ratio is below the

critical threshold of 0.31, almost no sacrificing of permselectivity is observed with decreased membrane thickness, while for membranes with a void ratio significantly larger than the threshold, permselectivity is low and conductance is high. The effect of different organic solvents on membrane synthesis can be well explained by solvent-polymer interaction. This work potentially provides fundamental guidance in developing high-performance IEMs.

### **3.2. Introduction**

The core components for membrane-dependent techniques such as reverse electrodialysis (RED) [52, 53], electrodialysis (ED) [54, 55], flow batteries [56, 57] etc. are ion exchange membranes (IEMs). The IEMs have been intensively investigated to achieve desired membrane performance in the above-mentioned processes [56, 58-60]. Membrane performance is determined by both the membrane's physicochemical properties (e.g., thickness, water content and hydrophilicity) and its electrochemical properties (e.g., permselectivity, area resistance, and ion exchange capacity (IEC)). Among these properties, permselectivity and area resistance have emerged as the two essential ion transport properties [53, 61].

Permselectivity measures the relative preference of membranes to permeate different ionic species (usually cations versus anions). Area resistance, or the inverse of a membrane's conductance, characterizes the ability to conduct ionic flow. Not surprisingly, these key membrane properties are inherently related to the microstructure of IEMs. Typical IEM microstructure consists of a polymeric matrix impregnated with negatively charged or positively charged functional groups. Such a charged membrane has traditionally been treated as a micro-heterogeneous system consisting of three phases (i.e.,

a hydrophobic inert polymer, an active ion exchange zone, and an interstitial zone) [62, 63]. The ionic conductivity of a membrane is mainly governed by the active ion exchange phase and the interstitial phase, whereas the permselectivity is governed by the mobility differences of counter- and co-ions in different membrane phases [63]. Many studies have focused on membrane conductivity associated with membrane microstructure [62]. However, limited consideration has been given to the correlation between permselectivity and microstructure of membranes. Attempts have been reported to associate permselectivity with ion exchange capacity, swelling degree, and other macro parameters of membranes [64]. However, when it comes to the interesting phenomenon where ultra-thin membranes suffer from lowered permselectivities, a fundamental understanding is still lacking.

When we consider membrane transport properties from the perspective of the percolative nature in their membrane microstructure, an intriguing correlation emerges. Modern percolation theory has been widely used in modeling continuous macroscopic objects. Randomly distributed sites or bonds are studied in their two- or three-dimensional connectivity. If different types of sites in the percolation lattice represent different phases in the membrane matrix, a natural combination of the three-phase model with the percolation theory emerges, and in fact, has been reported in the study of IEMs [62, 65, 66]. These studies focused primarily on the percolative behavior of membrane conductivity. Hence, when the conductive site ratio in the lattice surpasses a threshold, the membrane conductivity dramatically changes. However, the plentiful structural information implied by percolation modeling is often omitted or untraceable.

In this study, a computational simulation of the percolation lattice representing different membrane phases has been implemented; therefore, the structural information generated was able to be retrieved and analyzed. Multiple experimental trials based on the Monte Carlo approach ensured statistically valid results. With the aid of simulation, various parameters involved in membrane transport phenomena can be obtained. From this perspective, membrane transport properties are modeled to explain the mechanisms of observed trends in conductivity and permselectivity with respect to membrane void ratio, which are calculated from the membrane thickness and water content.

### **3.3. Model Development**

#### *3.3.1. Simplified three-phase model*

The microstructure of an ion exchange membrane is assumed to be simulated based on the classical three-phase model. This three-phase model is a theoretical approach to model IEMs, which assumes three different phases existing within an ion exchange membrane matrix. As demonstrated in Figure 3, the three phases/regions can be classified into: 1) polymer molecular backbones that do not have contact with electrolytes but occupy the inner space of the polymer matrix (inert phase,  $f_{11}$ ); 2) active functionalized sites (e.g., sulfonated polymer chain sites) on the surface of polymer chains (pure gel phase,  $f_{12}$ ); and 3) electroneutral electrolyte solution filling the voids between inert phases (inter gel phase,  $f_2$ ) [62, 67]. In this work, the pure gel phase for SPPO cation exchange membranes (CEMs) is the functionalized  $\text{SO}_3^-$  groups on the poly(phenylene oxide) (PPO) polymer backbones. Because ions can transport through two distinct phases, the gel phase and the inter-gel phase with different electrochemical properties, we can simplify the microstructure by

working with only two distinct phases in the following modelling procedure. The gel phase, which represents the selective phase, is favourable to counter-ions transport; meanwhile, the inter-gel phase is not limited to the permeation of counter-ions. The inter-gel phase provides an opportunity for co-ions to transport through the membrane. Furthermore, because membrane permselectivity and conductivity in a salt solution is of concern, we will focus only on these two properties. In addition, we assume the cross-section of the membrane microstructure in Figure 3 goes through the membrane thickness. Therefore, only the inter-gel phase (the light blue area) connecting the upper and lower surfaces of the membrane is considered “percolated” in the following discussion.

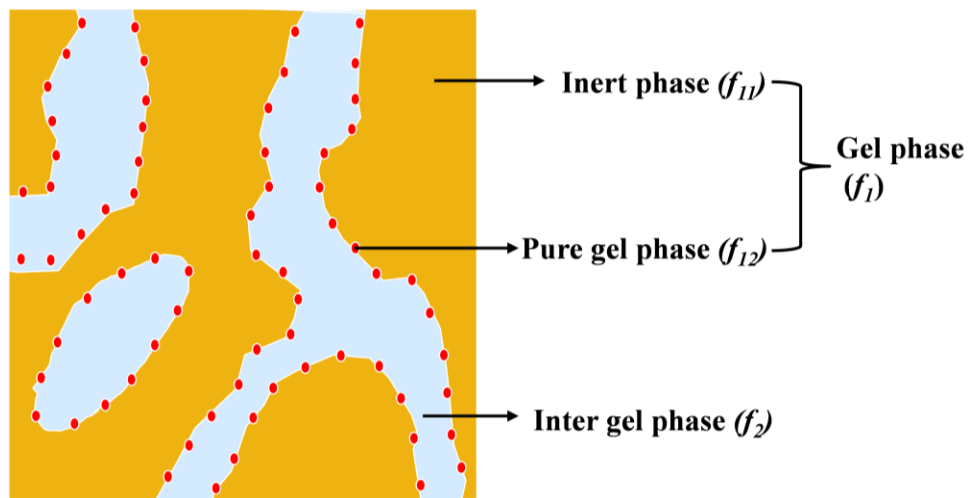


**Figure 3 - Schematic of a three-phase model for a charged IEM.**

Membrane permselectivity is defined as the ratio of the flux of counter-ions to the total ionic flux (i.e., current density) through the membrane under a given driving force. This driving force can be due to a salinity gradient or electrical potential. In the case of permselectivity measurement, salinity gradient (0.5 M over 0.1 M NaCl solution) is the driving force. Therefore, the transport number of counter-ions and co-ions of a CEM (transporting majorly cations) must have a relationship as expressed in Equation 5 [67].

$$\frac{t_+}{t_-} = \frac{V_1 J_+^G + V_2 J_+^S}{V_1 J_-^G + V_2 J_-^S} \quad (5)$$

where  $J$  indicates flux ( $\text{mol m}^{-2} \text{s}^{-1}$ ); superscript  $G$  denotes the gel-phase ( $f_1$ ) parameters, and superscript  $S$  denotes the electrolyte phase filling the interstitial voids within the membrane matrix ( $f_2$ );  $V$  denotes the cross-section volume of different phases in the membrane matrix; positive (+) and negative (-) signs denote counter-ion and co-ion, respectively.

Considering the definition of flux, we have:

$$\frac{t_+}{t_-} = \frac{V_1 D_+^G \Delta c_+^G + V_2 D_+^S \Delta c_+^S}{V_1 D_-^G \Delta c_-^G + V_2 D_-^S \Delta c_-^S} \quad (6)$$

where  $D$  and  $\Delta c$  denote diffusivity and ion concentration of different ions in different phases, respectively. Ion valence has been omitted assuming we have sodium chloride as the model electrolyte with a 1:1 charge ratio. Then, an approximation is made here that the leakage of co-ions is majorly through interstitial electrolytes ( $f_2$ ), because of the significant low concentration of co-ions on the inter-gel phase surface. Therefore, Equation 6 can be simplified as follows:

$$\frac{t_+}{t_-} = \frac{V_1 \frac{D_+^G \Delta c_+^G}{D_-^S \Delta c_-^S} + V_2 \frac{D_+^S \Delta c_+^S}{D_-^S \Delta c_-^S}}{V_2} \quad (7)$$

Furthermore, in the NaCl solution, which is a concern in this study, we can assume:

$$D_+^s \Delta c_+^s \cong D_-^s \Delta c_-^s \quad (8)$$

Also, the definition of permselectivity ( $P$ ) and the relationship between counter-ions and co-ions can be expressed as [68]:

$$P = 2t_+ - 1 \quad (9)$$

$$t_+ + t_- = 1 \quad (10)$$

Then, we can finally show a linear relationship between the reciprocity of permselectivity and the volume of different phases as:

$$\frac{1}{P} \cong \frac{2D_-^s \Delta c_-^s}{D_+^s \Delta c_+^s} \cdot \frac{V_2}{V_1} + 1 \quad (11)$$

The relationship listed in Equation 11 indicates that, at a given membrane material and salinity gradient, the ratio of volumes of different membrane phases (defined as percolative-to-inert volume ratio) will show a linear relationship with the inverse of permselectivity. Membrane permselectivity can be measured experimentally. However, to obtain this volume ratio of different phases, direct experimental measurement is not feasible. Essentially, the volume of percolated sites, or the number of sites belonging to the percolative clusters  $V_1$ , is a function of microstructure parameters as shown in:

$$V_1 = 1 - V_2 = \varphi(f_2, \delta) \quad (12)$$

where  $f_2$  is the inter-gel phase site number, and  $\delta$  is the membrane thickness.

The relationship between the percolated sites and the inter-gel phase and membrane thickness is non-trivial. There is no known analytical relationship between  $V_1$  with  $f_2$  and the  $\delta$  of the function due to the complexity of percolative and non-percolative distribution with respect to inter-gel phase and membrane thickness. The focus of the next section is to discuss this complexity and how a Monto Carlo approach can help simulate the relationship depicted in Equation 12.

### 3.3.2. Percolation theory and microstructure simulation

Percolation theory originates from the study of flow through porous media [69]. Mathematically, given a lattice of side length,  $L$ , let randomly chosen sites be of conductivity,  $b$  (or open) with a probability,  $p$ . Accordingly, the probability of a site having the conductivity of  $a$  (or closed) is  $1 - p$ . If  $b \gg a$ , the observed system conductivity characteristics change abruptly (or an infinite connected cluster appears) when  $p$  is larger than the critical threshold. In the context of ion transport through a CEM, the percolation threshold is a statistically defined minimum fraction of open volume (or a ratio of sites opening), to allow for the desired transport. If the transport of co-ions through the membrane is of concern, percolation happens when there is at least one connected pathway for co-ions to mitigate across the membrane. Table 1 summarizes percolation thresholds reported in the literature. For example, for a lattice matrix represented by continuous site cubes, a randomly distributed open site reaches about 31.2% of the total sites. Percolation pathway exists with a probability of higher than 50%. When pass the threshold, percolation probability rapidly increases to almost 100%, i.e., a percolative pathway exists for certain.

**Table 1 - Reported percolation threshold from literature.**

<b>Dimensionality</b>	<b>Bond</b>	<b>Site</b>	<b>References</b>
2D squares	0.500	0.593	[70]
3D cubes	0.249	0.312	[71, 72]

There is another interesting property having to do with the size of the threshold arising from percolation theory. If percolation is defined as occurring when a continuous connection of upper- and bottom-layer sites exists, then, the number of sites on the length and width dimensions is also an essential component in determining the threshold [71]. Specifically, as seen in Figure 4, the percolation threshold increases with increasing lattice thickness. Variations in the membrane phase distribution near the threshold develop roots from this property and reflect the dependency of percolated fractures on membrane thickness in Equation 12.

A sharp increase of percolation probability near the threshold exists, i.e., no matter how thick the lattice; moreover, a small change in open site probability near the threshold would transit from no percolation at all to almost surely percolated. When the open site fraction becomes significantly higher than the threshold, finding the percolation pathway is certain, and the number of open sites belonging to percolated clusters increases with the open site fraction.

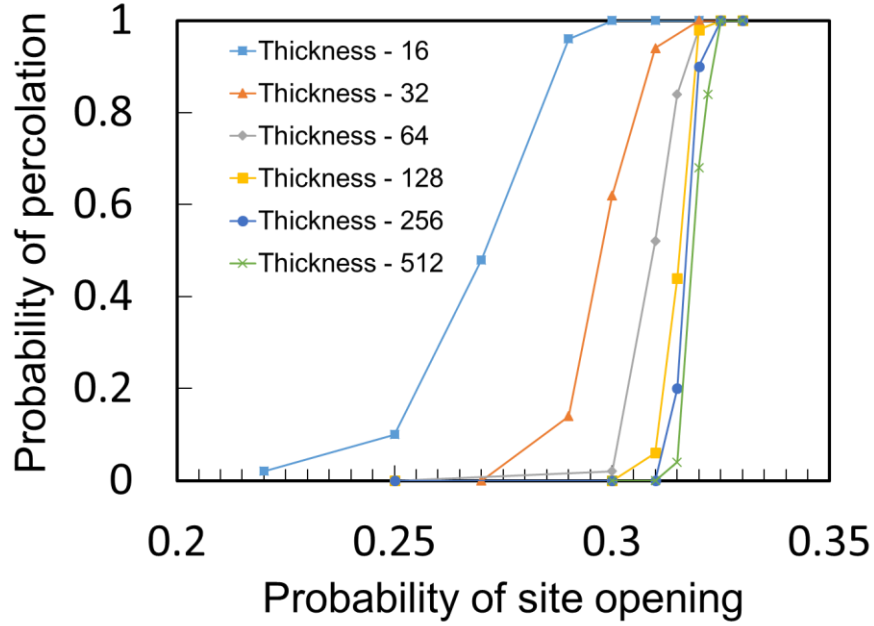


**Figure 4 - Simulation of percolation probability as a function of lattice thickness with at least 100 trials at each setting. In these exemplary lattice, width and length are set to 64 with periodic boundary condition, but the thickness varies from 16 to 512. The threshold moves from 0.22 to 0.31, close to the theoretical value of infinite lattice size.**

### 3.3.3. Membrane Conductivity

Other than membrane permselectivity, membrane conductivity is also related to ion transport in the membrane matrix. The governing Nernst-Planck equation shows how the flux of ions can be expressed as:

$$J_k = -D_k \frac{dC_k}{dx} - u_k C_k \frac{d\varphi}{dx} = -D_k \frac{dC_k}{dx} - D_k \frac{C_k F}{RT} \frac{d\varphi}{dx} \quad (13)$$

where  $J_k$  is the flux of ions ( $\text{mol} \cdot \text{m}^{-2} \cdot \text{s}^{-1}$ ) in the solution;  $D_k$  is the diffusivity of an ion species ( $\text{m}^2 \cdot \text{s}^{-1}$ );  $\varphi$  is the external electrical potential applied to the system (V);  $u_k$  is the

mobility of ions ( $\text{m}^2 \cdot \text{V}^{-1} \cdot \text{s}^{-1}$ );  $R$  is the gas constant;  $F$  is the Faraday constant, and  $T$  is the temperature (K). Moreover, the diffusion term can be further defined such that the current density is [73]:

$$\mathbf{i} = F \sum_k \mathbf{J}_k = -F^2 \sum_k \frac{c_k D_k}{RT} \left( \frac{RT}{c_k F} \frac{dc_k}{dx} + \frac{d\phi}{dx} \right) = -F^2 \sum_k \frac{c_k D_k}{RT} \left[ \frac{d}{dx} \left( \frac{RT}{F} \ln c_k \right) + \frac{d\phi}{dx} \right] \quad (14)$$

Both terms in the bracket have the dimension of potential gradient and can, thus, further be expressed in a combined form (the electrochemical potential gradient if the pressure components are neglected). Let the combined potential be  $\Phi$  (V); then, considering gel phase and solution phase, we have:

$$\mathbf{i} = -\frac{F^2}{RT} (c_i^G D_i^G + c_i^S D_i^S) \frac{d\Phi}{dx} \quad (15)$$

However, Ohm's law states that the conductivity  $\kappa$  ( $\text{S} \cdot \text{m}^{-1}$ ) is:

$$\mathbf{i} = \kappa \frac{d\Phi}{dx} \quad (16)$$

Thus, by substituting Equation 14 into Equation 15, the conductivity of the membrane phase solution is:

$$\kappa = \frac{F^2}{RT} (c_i^G D_i^G + c_i^S D_i^S) \quad (17)$$

The superscript  $i$  indicates either a counter-ion or co-ion. Note that the minus sign only indicates the direction of the current in Equation 14 and is neglected in Equation 15. Finally, for a membrane with a thickness of  $h$ , the overall membrane resistance, or inverse of conductivity, is the summation of all resistance from all parts of either the gel phase or solution phase:

$$R_m = \int_0^h \frac{dx}{\kappa} = \int_0^h \frac{RT}{F^2 (c_i^G D_i^G + c_i^S D_i^S)} dx \cong \sum_{\Delta x} \frac{RT \Delta x}{F^2 (c_i^G D_i^G + c_i^S D_i^S)} \quad (18)$$

The integral is necessary in case of considering both gel-phase and solution phase. However, with the simulation, a discrete volume with a known phase can be used to sum

up the overall resistance of membrane bulk. This approach provides another method to validate the simulation.

#### 3.3.4. *Simulation Methodology*

The percolation theory is used not only to study the transport behavior of membranes near the threshold, but also to simulate the distribution of gel-phase ( $f_1$ ) and inter-gel phases ( $f_2$ ). The spatial distribution of sites provides additional information that can be used to derive membrane properties in combination with the three-phase model. For example, the volume ratio of the membranes that are part of the percolation clusters can be obtained from the simulation.

Moreover, a detailed differentiation of site and cluster types is also enabled. For example, randomly distributed sites or clusters connect to upper or lower surfaces but are not part of the percolated clusters (i.e., “dead ends”). Inert open sites also exist surrounded by closed sites that are usually counted toward  $f_2$  in conventional percolation studies. Because transport properties are of concern in this study, these differentiations are reflected in the simulation and are treated accordingly. In permselectivity analysis, since a percolated cluster is assumed to enable co-ion transport, only opening sites on both surfaces belonging to percolating clusters are counted towards  $V_2$ . However, in terms of membrane conductance, an alternating current (AC) is applied to determine it. Then, an explicit calculation of conductance is made possible by considering the in-series connection of sites in the depth dimension and in-parallel conducting pathways of the length and width dimensions.

Simulation of a 3-D lattice was implemented in Java (jdk1.8.0\_141) on IntelliJ IDEA 2017.2.3 on a personal computer with 16 GB memory, using an Intel i7 – 6700HQ

processor. A 3-D multi-layer of cubes were initially generated with all sites set to closed. To model the membrane, the depth dimension was explicitly layered in accordance with a real sample thickness with 1 cube representing 15 nm x 15 nm x 15 nm of volume (as shown in Figure 5). Due to limitations in computational capacity, periodic boundary conditions were applied on the width and length dimensions with 64 sites representing each dimension. Simple algorithm implementation of sets unification and testing operations were efficient in processing open- or closed-site information. A Monte Carlo approach was adopted to tackle statistical variation among different experiments. At least 100 simulations were run representing different slices of membrane pillars and reflecting the effect of average percolation probability over the larger membrane area. Randomly selected sites were opened until the desired open site number was reached. The resulting open and closed sites represent a membrane layer with electrolytes as open sites and the inert phase (polymeric backbone) as closed sites. In addition to spatial information, the number of sites that were in the cluster connecting upper and lower surfaces was also obtained and considered an inter-gel phase. Conductance of the membrane was also calculated based on the conductance of each single site.

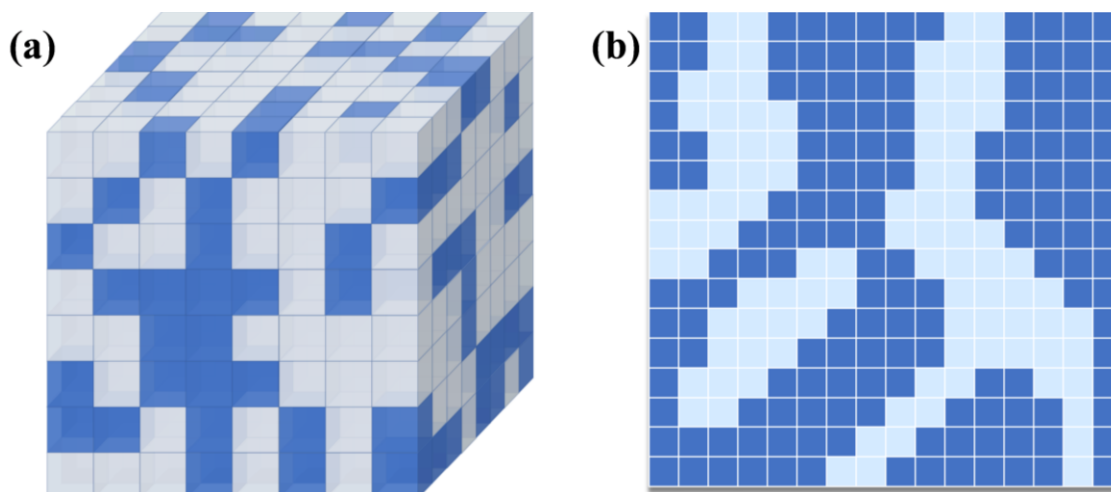


**Figure 5 - Schematic of (a). a 3-D lattice and (b). the cross - section for the study of site percolation. Blue sites are defined as open sites and blank sites are closed to ion transport, so total volume of blues sites is the inter-gel phase volume.**

### **3.4. Materials and Methods**

#### *3.4.1. Materials*

Poly (2, 6-dimethyl-1, 4-phenyleneoxides) (PPO, Mw 30000 and Mn 20000, MilliporeSigma, Burlington, MA, USA) were used as the polymer block. Additionally, 98% of chlorosulfuric acid (MilliporeSigma, USA) was applied for the sulfonation reaction. All of the following were also purchased from MilliporeSigma: 99.5% anhydrous N-methyl-2-pyrrolidone (NMP), anhydrous 99.8% dimethylformamide (DMF), and 99.9%

ACS reagent dimethyl sulfoxide (DMSO), all of which were selected as organic solvents. Furthermore, 99% anhydrous chloroform and 99.9% methanol for HPLC were purchased from MilliporeSigma and used as received. Deionized (D.I.) water was generated from by a NANOpure Diamond™ Ultrapure water system (Barnstead International, Dubuque, IA, USA).

#### 3.4.2. *Preparation of cation exchange membranes*

The sulfonation of poly 2, 6-dimethyl-1, 4-phenyleneoxides (PPOs) was conducted based on the protocol of previous work [74]. Briefly, PPO was dissolved into chloroform (9.6 wt%) with a magnetic stirring at room temperature. Further, chlorosulfonic acid dissolved in chloroform at a ratio of 1:12 (v/v) was slowly added into the PPO solution using a pressure-equalizing dropping funnel while stirring. The resulting precipitate was filtered and washed several times with deionized (DI) water, until the pH reached an approximately neutral value. The obtained SPPO was then redispersed into methanol, and the solution was poured into a Pyrex glass tray to dry at room temperature.

Next, solution casting and phase inversion methods were used to synthesize SPPO CEMs. Each batch of polymer solution was prepared by dissolving certain amounts of SPPO into NMP and DMF with a volume ratio of 1:2.5, respectively. For the solvent, DMSO, the SPPO to DMSO volume ratio used is 1: 4.0. The polymer solution was stirred for 48 hours at room temperature to get a homogeneous solution. The resulting polymer solution was cast onto glass plates using a doctor's blade with precise control of thickness. Then, the cast membranes were dried in air at ambient temperature together with the glass plates. After drying, the membranes were peeled off from the glass plates, and were immediately soaked into 1 M HCl solution for 24 h. Finally, the obtained CEMs were

stored in 0.5 M NaCl solution for future use. The prepared membranes were labeled SPPO-X, where X denotes the organic solvents used in this work.

### 3.4.3. Membrane characterizations

Cross sections of different CEMs were characterized by a Hitachi SU8010 field emission scanning electron microscopy (FE-SEM). To determine membrane thickness under wet conditions, a Hitach S-3700N variable pressure SEM (VPSEM,) was used. With an additional measurement of the cut-away sample of the membrane area, the total volume of the wet membrane can be calculated and used to calculate the void ratio of a membrane sample. The void ratio was used as the ratio of open sites in the simulation [64].

The membrane's apparent permselectivity was measured using a static potential method with at least three replicates. For the conductance measurement, a resistance reading at an AC frequency of 1000 Hz and an amplitude of  $1.8 \text{ A m}^{-2}$  was used with at least six replicates. The appendix A depicts the experimental setup, measurement of the membrane's apparent permselectivity, and conductance (reciprocal of area resistance) using AC, which are all based on previous work [26, 75].

Membrane water content is usually reported in the literature [53, 76]. However, in this study, the simulation input is the void volume ratio within a swelled membrane matrix, i.e., membrane material expanded naturally in a wet status. Membrane pieces with a known wet status were removed from stock solution before measurement. Their surface water was carefully wiped off with Kimtech wipes and immediately weighed. After the wet weight was recorded, the dry weight was measured after drying in an oven at  $60^\circ\text{C}$  for at least 24 hours. Then, the void volume ratio of the membrane sample was calculated as follows:

$$\mathbf{Void\% = 100\% - \frac{(w_{wet} - w_{dry})/\rho_w}{A \times \delta} \times 100\%} \quad (19)$$

where,  $w_{wet}$  and  $w_{dry}$  are the membrane sample's wet and dry weight, respectively.  $\rho_w$  is the water density at 25 °C;  $A$  is the membrane area, and  $\delta$  is the wet thickness of the membrane sample.

### **3.5. Results and discussion**

#### *3.5.1. Membrane structure and electrochemical properties*

The polymer structure of SPPO membranes prepared with different organic solvents and commercial Fumasep<sup>®</sup> FKS membranes (FuMA-Tech GmbH, Bietigheim-Bissingen, Germany) appeared in the cross-sectional images. As seen in Figure 6, a dense polymer matrix covers the NMP-based and DMF-based membranes, which is similar to the structure of commercial FKS membranes, while the membranes prepared from DMSO exhibit a relatively loose structure. The structure difference might potentially be attributed to the polymer-solvent interactions, also termed as polymer-solvent affinities.

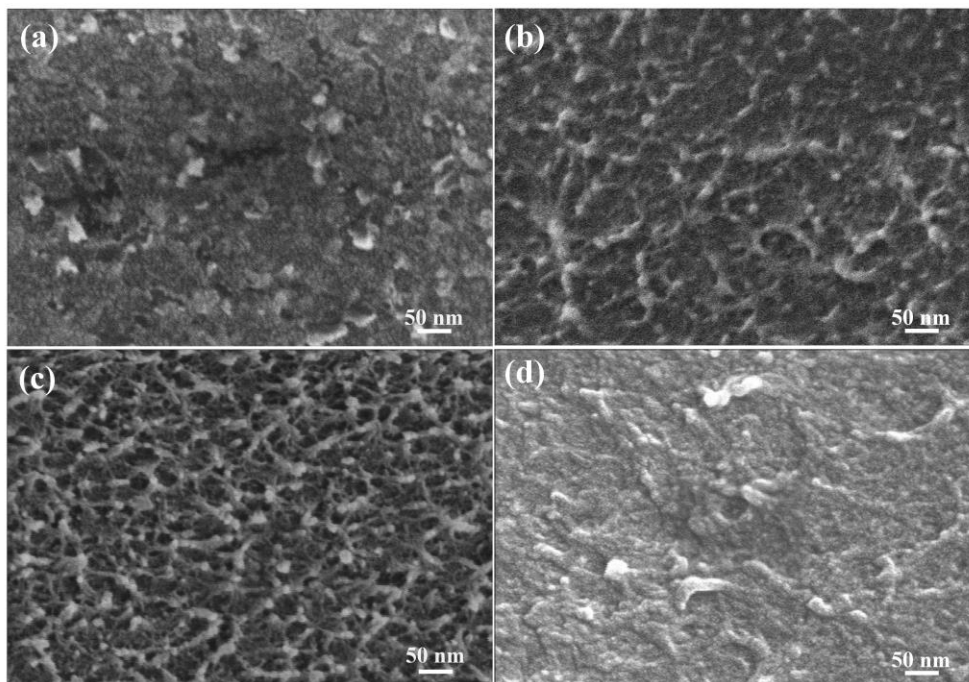


**Figure 6 - Cross sections of SPPO membrane with (a) NMP, (b) DMF), (c) DMSO as solvents, respectively; and (d). Cross section of a commercial FKS membrane.**

### *3.5.2. Solvent-polymer interaction implication*

The difference between Hansen solubility parameters (HSP) of polymer and organic solvents has been widely used to evaluate the solvent-polymer affinity [77]. The smaller differences between the solubility parameters of polymer and solvent suggests stronger polymer-solvent interactions. The relative strength of polymer-solvent interactions determines the properties of the casting solution and presumably the

morphology of the final membrane [78]. The Hansen solubility parameter difference between polymer and solvent can be calculated as [78]:

$$D_{p,s} = \sqrt{(\delta_{p,D} - \delta_{s,D})^2 + (\delta_{p,P} - \delta_{s,P})^2 + (\delta_{p,H} - \delta_{s,H})^2} \quad (20)$$

where  $p$  and  $s$  indicate polymer and solvent, respectively. Moreover,  $\delta_D$ ,  $\delta_P$ , and  $\delta_H$  represent the dispersion forces, dipolar interactions and hydrogen bonding forces, respectively.

The IEC of the SPPO used in this work was determined to be 1.89 meq/g by the acid-base titration method. The detailed methods for IEC measurement was demonstrated in the Appendix A. Then, the degree of sulfonation (DS), i.e., the average number of sulfonic groups present in the SPPO, was calculated to be 26.7 % as a result of the followed relationship [79]:

$$DS = 120 IEC / (1000 + 120 IEC - 200 IEC) \quad (21)$$

While using HSP, the miscibility for SPPO in different organic solvents was compared as listed in Table 2. The HSP differences between SPPOs have shown similar values, while SPPO in DMSO has a larger value indicating a smaller affinity of SPPO for DMSO, which in turn results in the relatively loose structure shown in Figure 6c. Since the ion transport properties are largely related to the microstructure of the membrane, the differences in membrane structure will potentially influence the membrane permselectivity and area resistance (as demonstrated in Figure 7). Apparently, the area resistance decreased almost linearly with reduced hydrated membrane thickness, while the permselectivity showed a decreasing trend only at a membrane thickness below a certain value.

**Table 2 - Hansen solubility parameters.**

	$\delta_D$ (MPa) <sup>1/2</sup>	$\delta_P$ (MPa) <sup>1/2</sup>	$\delta_H$ (MPa) <sup>1/2</sup>	$\delta_t$ (MPa) <sup>1/2</sup>	$D_{p,s}$
SPPO	17.8	4.0	9.1	20.4	-
NMP[80]	18.0	12.3	7.2	23.1	8.52
DMF[80]	17.4	13.7	11.3	24.9	9.98
DMSO[81]	18.4	16.4	10.2	26.7	12.51

Permselectivity and ionic resistance of the set of CEMs investigated in this work were well determined. As shown in Figure 7a, the area resistance for the set of SPPO membranes shows an apparent decreasing trend upon the hydrated membrane thickness. While, permselectivity of the commercial FKS membrane is less sensitive to membrane thickness. With relatively large thickness, the permselectivity of membranes prepared with NMP and DMF is closer to the that of the FKS membrane. However, the permselectivity of membranes fabricated with DMSO is much lower even for thick membranes. With respect to the ionic resistance, thinner membrane thickness is favorable to both SPPO membrane and commercial FKS membrane as shown in Figure 7b, which shows good agreement with the findings reported in the literatures. Based on the trends demonstrated as Figure 7, there's apparent trade-off between membrane permselectivity and area resistance. The thinner membrane thickness renders a membrane lower ionic resistance which the permselectivity is largely sacrificed.

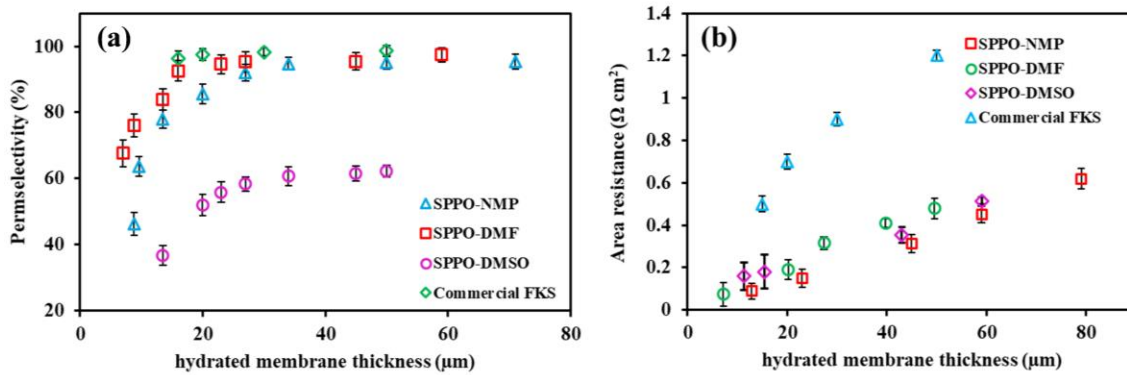


**Figure 7 - Permselectivity (a) and area resistance (b) for a series of CEMs as a function of membrane hydrated thickness.**

### 3.5.3. Validation of implementation

As shown in Figure 8, the volume of sites that relate to a percolation path is highly affected by void ratio and lattice thickness. First, void ratio is the major determinate of the percolated area ratio. When void ratio is in the range of 0.3 to 0.4 (Figure 8a), the percolation probability effect is manifested. The number of sites that belongs to percolated pathways connecting the top and bottom of a simulated lattice decreases rapidly and soon hits zero (i.e., no longer able to form any connecting pathway from top to bottom or vice versa). This is in accordance with the simulated percolation probability of 0.31 in Figure 4. When the void ratio is higher than 0.4 (Figure 8b), the percolated surface area rapidly becomes level to void ratio values. A high void ratio results in all open sites connecting to the percolation paths. The probability of finding such open sites on the surface is the same

as simulated inter-gel volume ratio (i.e., void ratio). Second, the effect of lattice thickness draws a much more subtle effect. Only in the range of 0.31 to 0.38 will a thinner lattice appear in some percolated areas compared to none for thicker lattices. However, this effect is insignificant when the void ratio is large enough.

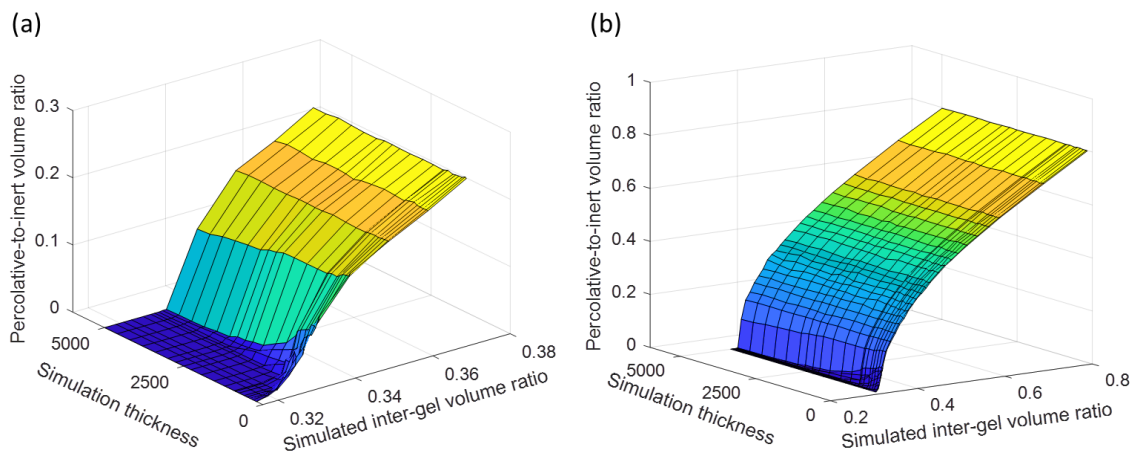


**Figure 8 - The effect of simulation thickness and simulated inter-gel volume rate on percolative-to-inert volume ratio. (a) Zoomed-in details with void ratio between 0.315 to 0.38 of simulated thickness is from 150 to 5000 units. (b) zoomed-out of same thickness rang and void ratio between 0.315 to 0.8.**

#### 3.5.4. *Simulation of the effect of membrane thickness on permselectivity*

The permselectivity of membranes with various thicknesses and a void ratio which was measured (as listed in Table 8). Plotting the inverse of permselectivity against the percolative-to-inert volume ratio (shown as Figure 9) has revealed a linear trend as predicted in Equation 11. The percolative-to-inert volume ratio is defined as the ratio of number of sites in percolating clusters to the number of sites belonging to the non-percolative gel-phase. Note that in Table 8, the void ratio alone is not able to explain the drop in the permselectivity of the thinner membranes. The void ratio of the thicker membranes was slightly higher than the 3-D infinite site percolation threshold; therefore, in this range, the membrane thickness plays a role in determining the number of percolated sites through the membrane matrix as illustrated in the simulation results (Figure 9). From this result, the observed permselectivity variation is well explained as percolated cluster pathways through the membrane matrix change, along with changes in the void ratio and membrane thickness. As the void ratio significantly increases over the percolation threshold, the effect of different membrane thicknesses does not respond to the same degree as when void ratio is near the percolation threshold.

Additionally, as seen from Figure 9, different organic solvents used to prepare the membranes will finally affect the ion conductivity for different membrane phases, but to a limited extent [82]. Therefore, slopes of two linear lines for SPPO-NMP and SPPO-DMF are quite close to each other due to the relatively similar Hansen solubility difference as listed in Table 2. Intersections of lines are close to unity, indicating the extreme condition where a perfect membrane without any co-ion pathway would have perfect permselectivity.

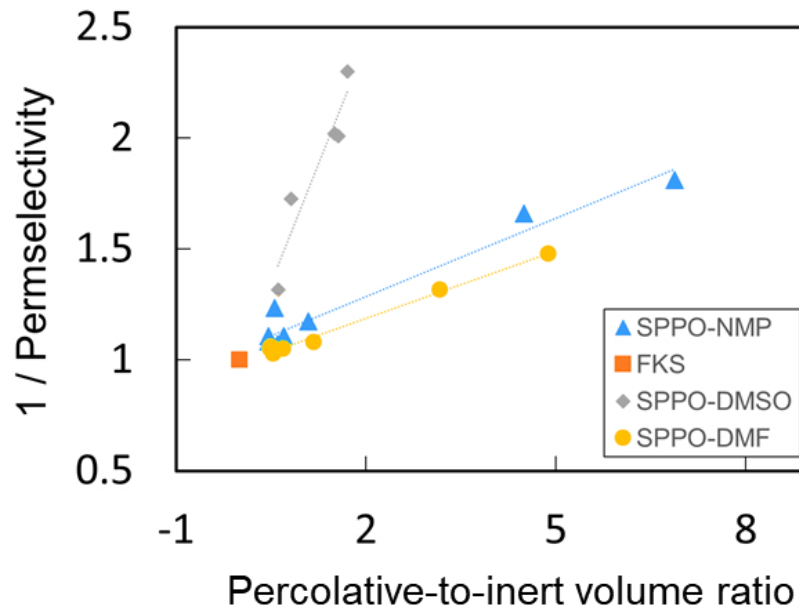


**Figure 9 - The inverse of permselectivity shows linear relationships to percolative-to-inert volume ratios for SPPO-NMP, SPPO-DMSO, and SPPO-DMF membranes. For commercial FKS membranes, the percolative-to-inert volume ratio remains at zero because all void ratios are below the 0.31 threshold. The FKS membranes are shown overlapping the red rectangle marks. The surface area ratio is defined as the ratio of the number of sites in percolating clusters to the number of sites on the rest of the surface.**

### 3.5.5. *Simulation of membrane thickness influence on membrane conductance*

Using the same set of thickness and water uptake data, the simulated membrane conductance showed good agreement as the experimentally measured data as shown in Figure 10. Total membrane conductivity was explicitly calculated using two different conductivities in two types of sites and applying conductance in a series along the depth dimension and conductance, in parallel along the length and width dimensions (as shown in Figure 28). This result is also in agreement with theoretical derivations from previous studies [83].

One may notice that the membrane resistance (the reciprocal of conductance) varied almost linearly with membrane thickness. However, a slight change of slope was observed due to changes in void ratio (i.e., the ratio of different types of sites). A significantly different conductivity of two site types contributed to this effect. Note that this effect was not affected by percolation states as much as those seen in the permselectivity case —when close to the percolation threshold, a void ratio created a significant change in the percolated site number. In the case of conductance measurements, since the AC mode was utilized and drives ions to migrate locally, both totally enwrapped inert sites as well as “dead end” sites (i.e., sites connecting both membrane surfaces but not thorough), contributed to the conductance from interstitial electrolytes. Therefore, abrupt changes due to percolation states were not as pronounced.

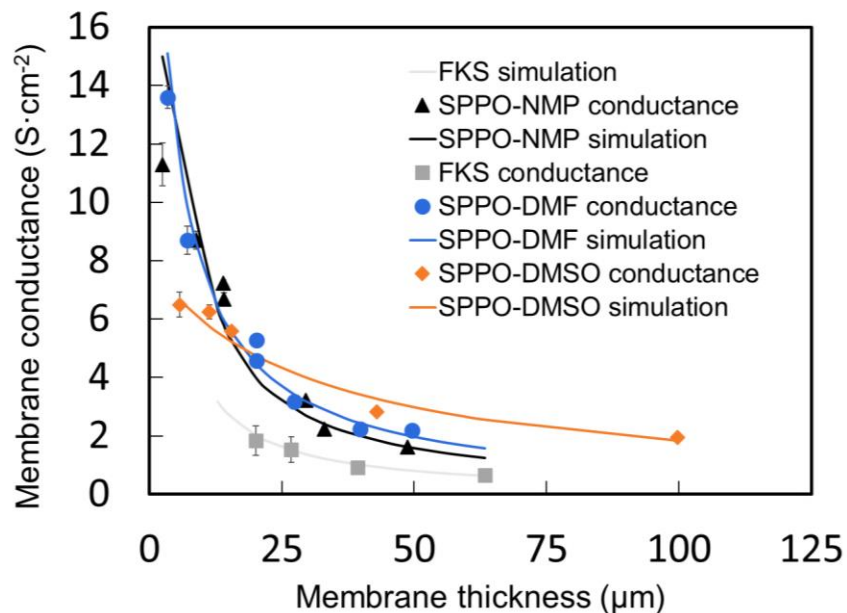


**Figure 10 - Membrane conductance of SPPO and as a function of thickness. Solid lines are the simulation fitting value from the model. Symbols represent experimental data.**

### 3.6. Conclusion

Two of the most important membrane properties, ionic conductivity and permselectivity, have been successfully modeled on a set of SPPO membranes of varying thicknesses prepared with three different organic solvents as well as a commercial FKS membrane. The membrane matrix was represented by a 3-D cube lattice. Combining the three-phase model and percolation properties of the lattice, the graduate loss of

permselectivity was well explained and validated by experimental data. In addition, membrane conductance can be fitted with spatial information from simulation to appropriately describe conductivities in different phases. With the help of simulation and modeling results, a deeper fundamental understanding of the balance of membrane permselectivity and conductance will facilitate future membrane synthesis with the anticipated properties for IEM-based electrochemical processes.

# **CHAPTER 4. MONOVALENT - ANION SELECTIVE AND ANTIFOULING POLYELECTROLYTES MULTILAYER ANION EXCHANGE MEMBRANES FOR REVERSE ELECTRODIALYSIS**

## **4.1. Abstract**

Reverse electrodialysis (RED) is an emerging membrane - based technology that can be used to capture renewable energy released from mixing seawater and river water. When natural waters are used as feed solutions, the presence of multivalent ions and natural organic matter (NOM) results in a lower open circuit voltage (OCV) and power density. In this research, we modified the surface of standard anion exchange membranes (AEMs) via the facile layer-by-layer (LBL) deposition of poly(styrenesulfonate) (PSS) and poly(ethyleneimine) (PEI). Only moderate increase was introduced to the membrane area resistance. The modified membranes exhibited monovalent - anion selectivity comparable to that of commercial monovalent-ion selective membranes, and largely improved anti-organic fouling potential simultaneously. When tested in a RED process with feed waters containing not only chloride but sulfate and humic acid, the maximum gross power density generated was improved by up to 17 % with polyelectrolyte-modified membranes. Also, the energy conversion efficiency of the modified membranes could be prominently increased by 3 times compared with standard AEM conversion. The results indicate significant efficacy of AEMs with polyelectrolyte multilayers on their membrane surface for RED application.

## 4.2. Introduction

Salinity gradient power (SGP) is recognized as one of the emerging sustainable and clean energy sources, which can be generated from mixing two aqueous solutions with different salinities [12, 59, 84, 85]. Based on the global river discharges to the ocean, a total power potential has been theoretically estimated to range from 1.4 to 2.6 TW [86, 87]. Considering the energy conversion efficiency, the technically harvestable SGP is assessed at approximately 0.983 TW, which is equivalent to 36.8 % of the world's net electricity generated in 2015 (234,00 TW h) [85, 88]. Reverse electrodialysis (RED) is one of the most attractive technologies used to harness SGP [59, 89]. RED is a membrane – based system with anion exchange membranes (AEMs) and cation exchange membranes (CEMs) alternatively stacked to allow selective ions transport.

RED has been increasingly investigated with artificial feed solutions containing only NaCl under lab-scale testing. However, the practical application of RED requires the use of natural freshwater and seawater or brine, which are composed of a mixture of monovalent and multivalent ions. Although the fraction of multivalent ions, such as  $\text{SO}_4^{2-}$ ,  $\text{Mg}^{2+}$ , and  $\text{Ca}^{2+}$ , is relatively small in comparison with that of  $\text{Na}^+$  and  $\text{Cl}^-$  in natural waters, their impacts on the power generation is noteworthy [28-31]. Previous studies have shown that the presence of multivalent ions, especially in a diluted solution, results in a decreased stack voltage and power generation [28, 29]. This lowering effect can be ascribed to the increasing ohmic resistance of a stack and the uphill transport of multivalent ions, i.e., the transport of multivalent ions against their concentration gradients [28]. However, for AEMs, the presence of  $\text{SO}_4^{2-}$  leads to a negligible increase on the membrane ionic resistance [30]. The uphill transport of  $\text{SO}_4^{2-}$  might be dominant in the lowering effect.

Typically, the standard AEMs have no specific selectivity towards monovalent ions. Therefore, one of the key membrane properties determining RED performance is the preferential selectivity for monovalent ions while eliminating the permeation of divalent ions.

Besides the presence of multivalent ions, the field application of the RED process is also limited by membrane fouling, which affects the membrane performance and reduces the effective lifetime of the membrane [32, 33]. Negatively charged natural organic matter (NOM), such as humic acids, will shield the positively charged groups in AEMs resulting in a decrease of the apparent permselectivity and an increase in membrane resistance [90]. The obtained power output and energy efficiency decreases rapidly when natural sources of feed water are used [32].

The mechanisms for mono/multivalent ions selectivity are mainly governed by size exclusion and electrostatic repulsion [91]. Based on these mechanisms, various methods have been proposed to achieve monovalent ion selectivity by membrane surface modification, mainly including the introduction of specific anion exchange groups controlling the hydrophilicity of the base membrane, the formation of a highly cross-linked layer on the membrane surface, and the formation of a weakly basic anion exchange group layer on the membrane surface [54, 92]. These approaches have been effective in changing the relative permselectivity between monovalent and divalent ions. However, most materials used for the above membrane modifications, such as polyaniline, polypyrrole etc., are generally hazardous or having high cost. Also, some of the methods such as introducing a highly cross-linked layer will result in undesired high membrane resistance,

which is detrimental to RED performance. Furthermore, none of these studies had a primary objective of obtaining specific antifouling properties simultaneously.

Sata et al. reported that the permselectivity for specific anions through AEM mainly depends on the negatively charged layer on the membrane surface [54]. The key factors to improving antifouling potential are to achieve relatively high hydrophilicity, and also a negatively charged membrane surface [93]. Guler et al. developed a monovalent-ion selective membrane with antifouling potential by copolymerization to form a highly negatively charged surface layer [94]. However, it was not found to be very effective for RED performance [94]. Recently, Mulyati et al. found that the simultaneous improvement of the monovalent-ion selectivity and antifouling potential of an AEM can be achieved by creating a strong negative charge on the membrane surface through layer-by-layer assembly of oppositely charged polyelectrolytes [95, 96]. The electrostatic repulsion between multivalent anions and a negative surface potential is greater than that between monovalent anions and a negative surface potential according to Coulomb's law, which means that multivalent anions are less likely to transport onto the membrane surface than monovalent anions [96, 97]. On the other hand, because of the electrostatic repulsion between the negative surface potential and the negatively charged organic foulants, accompanied by the increase of hydrophilicity of the membrane surface, the antifouling property could be significantly improved [95]. Layer-by-layer (LBL) assembly of polyelectrolytes is an attractive facile method without organic solvent used in the process [98]. This approach has been used to achieve high mono/divalent ions selectivity in direct methanol fuel cells (DMFCs), flow batteries, etc. [99-102]. To promote the LBL process,

external driving forces such as electric field, electric-pulse have been introduced to assist the LBL assembly to achieve high monovalent-ions selectivity [103, 104].

In the present work, we aim to obtain the simultaneous improvement of monovalent –anion selectivity and antifouling potential via LBL assembly of PSS and PEI at standard grade AEMs surface. For the first time, we evaluated the efficacy of this method for RED power generation and characterized the physiochemical and electrochemical properties of the membranes before and after modification. Also, we investigated the antifouling potential improvement of the membranes after coating. Finally, we assessed the energy conversion efficiency and the performance of modified membranes in the RED system with feedwaters containing  $\text{SO}_4^{2-}$  and NOM besides  $\text{Cl}^-$ .

### **4.3. Experimental**

#### *4.3.1. Materials*

The membranes used in this study are listed in Table 3. The CJMA-2 (Hefei Chemjoy Polymer Material Co., Ltd., Hefei, China) membrane is a standard AEM with no specific selectivity towards monovalent anions. Neosepta ACS (ASTOM, Tokyo, Japan) membranes are the commercial AEM having monovalent – ion selectivity on both sides of its surface. The strong polyelectrolytes, poly(ethyleneimine) (PEI,  $M_w = 750,000$  g/mol, ~ 50 % in water, MilliporeSigma) and poly (4-styrenesulfonate) (PSS,  $M_w = 70,000$  g/mol, MilliporeSigma) were selected as the oppositely charged polyelectrolytes to form LBL multilayers on the CJMA-2 membrane surface. PSS can be fully charged in aqueous solutions, and PEI might achieve high protonation based on solution pH. The chemical structures of PEI and PSS are shown in Figure 29. Sodium dodecylbenzene sulfonate

(SDBS, technical grade, MilliporeSigma) and humic acid sodium salt (technical grade, MilliporeSigma) were used as the model organic foulants. Sodium chloride (99.0 %, MilliporeSigma) and sodium sulfate (99.8 %, Chem-Impex Int'l Inc., USA) were utilized for most of the membrane properties measurements. Potassium hexacyanoferrate (III) ( $K_3Fe(CN)_6$ , 99.0 %, MilliporeSigma) and potassium hexacyanoferrate (II) trihydrate ( $K_4Fe(CN)_6 \cdot 3H_2O$ , 98.5 %, MilliporeSigma) were used to make electrode solutions for RED performance tests.

**Table 3 - AEMs used in this work.**

<b>Membranes</b>	<b>Trademark</b>	<b>Type</b>	<b>Reinforcement</b>
CJMA-2	Chem Joy	Standard	no
ACS	Neosepta	Monovalent-ion selective	PVC
CJMA-2-N <sup>a</sup>	Custom-made	Monovalent-ion selective	no

a: the number of PSS/PEI bilayers.

#### 4.3.2. Surface modification of CJMA-2 membranes

The coating solution was made by dissolving 1.0 g/L PSS or PEI in 1.0 M NaCl solution at room temperature. Based on the zeta potential of the PEI solution (shown in

Figure 30), the pH value of the PEI solution was adjusted to 5.0 with 1.0 M HCl. No adjustment was made for the pH value of PSS solution. The CJMA-2 membranes were first exposed to a PSS solution for 30 min, followed by a PEI solution for another 30 min. The remaining coating layers were formed by treating CJMA-2 with alternating PSS and PEI solutions for 20 min each. Membranes were thoroughly rinsed with DI water for approximately three minutes after each coating process. Only one side of the membrane surface was modified. The modified membranes were designated as CJMA-2-N, where N is the number of PSS/PEI bilayers. In this work, N denotes the number of bilayers, therefore, is always a number ending in half as PSS is always the top layers. The membranes were air-dried, and their thicknesses were measured using a Digimatic micrometer (Mitutoyo Corporation, Kawasaki, Japan).

#### *4.3.3. Electrochemical properties characterization*

Apparent permselectivity of the membranes were determined by monitoring the potential differences across membrane generated between two NaCl solutions at concentrations of 0.5 M and 0.1 M. Area resistance measurements were carried out in a custom-made four-cell module (Figure 11), where the membranes under investigation were placed in the center, and two same commercial CEMs, Fumasep FKS membranes (Fumatech GmbH, Germany) were used as shield membranes. A 0.5 M NaCl solution and a 0.5 M Na<sub>2</sub>SO<sub>4</sub> solution were used as testing solution and electrolyte, respectively. Electrochemical impedance spectroscopy (EIS) measurement using alternating current was applied to analyze membrane resistance.

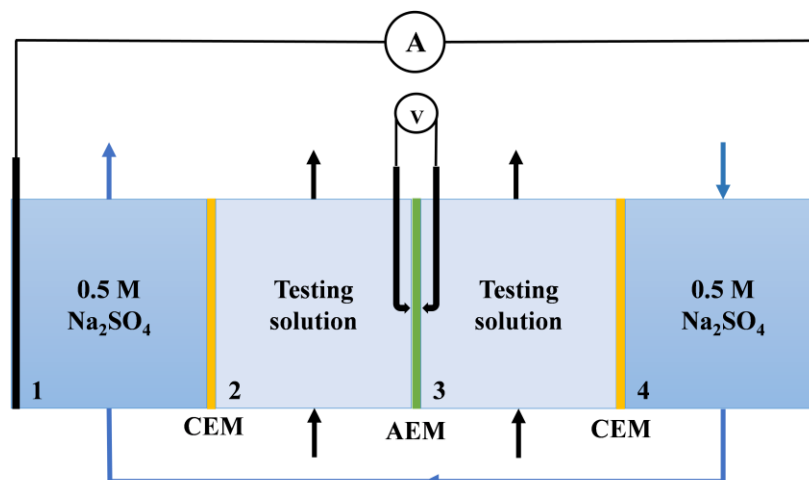


**Figure 11 - Schematic setup of a four-cell testing module.**

To investigate limiting current density of different membranes, chronopotentiometry was conducted with a mixture of 0.05 M NaCl solution and 0.05 M  $\text{Na}_2\text{SO}_4$  solution under direct current conditions to yield current-voltage ( $I$ - $V$ ) curve in the same four-compartment modules (Figure 11). A 0.5 M  $\text{Na}_2\text{SO}_4$  solution was used as the electrolyte. The solutions in each cell were circulated individually at a flow rate of 100 mL/min by a Masterflex L/S peristaltic pump (Cole-Parmer Instrument Company, USA). The applied current was raised step by step (i.e., 0, 5, 10, ..., 320 mA every 20s) and was provided by a power supply (Model 1665 DC power supply, BK Precision Corporation). The potential over the membrane between custom-made Haber - Luggin capillaries was recorded. The  $I$ - $V$  curve was plotted by current density versus voltage across membrane.

For the RED system, the maximum power generation is usually captured below the over-limiting current density region. Thus, current density in the under-limiting range was applied for transport numbers and the antifouling potential test.

#### 4.3.4. Transport numbers

The monovalent-ion selectivity of the membranes is indicated by the transport number ratio between monovalent and divalent ions. In this case, the ions are the monovalent chloride and divalent sulfate. To get the bulk transport numbers, the ionic fluxes of  $\text{Cl}^-$  and  $\text{SO}_4^{2-}$  through the membranes with time elapsed were measured in the same four-compartment cell (Figure 11). A mixture of 0.05 M NaCl and 0.05 M  $\text{Na}_2\text{SO}_4$  was used as the testing solution, and 0.5 M  $\text{Na}_2\text{SO}_4$  was used as the electrolyte. The current density applied was held constant at 4.0 mA/cm<sup>2</sup> with the effective membrane area of 7.91 cm<sup>2</sup>. The solutions were circulated individually for each compartment at a flow rate of 100 mL/min. 2 mL of testing solutions were taken from compartments 2 and 3 every 30 min. The concentrations of  $\text{Cl}^-$  and  $\text{SO}_4^{2-}$  were analyzed by a Dionex AS50 Autosampler in the Dionex DX-500 ion chromatography system (Dionex Corp., Sunnyvale, CA, USA). The corresponding ion flux of  $\text{Cl}^-$  and  $\text{SO}_4^{2-}$  passing through the membrane ( $J_i$ ) is calculated based on the ions concentration change with time ( $dC_i/dt$ ) in the dilute compartment as follows:

$$J_i = \frac{V \left( \frac{dC_i}{dt} \right)}{A} \quad (22)$$

where V is the volume of the circulated testing solution (cm<sup>3</sup>) and A is the effective membrane area (cm<sup>2</sup>).

To evaluate the improvement of monovalent-ion selectivity of the membranes after modification, the transport number ratio between  $\text{Cl}^-$  and  $\text{SO}_4^{2-}$  ( $P_{\text{SO}_4^{2-}}^{\text{Cl}^-}$ ) was determined based on Equation 23 [105].

$$P_{\text{SO}_4^{2-}}^{\text{Cl}^-} = \frac{t_{\text{Cl}^-}/t_{\text{SO}_4^{2-}}}{c_{\text{Cl}^-}/c_{\text{SO}_4^{2-}}} \quad (23)$$

where  $t_{\text{SO}_4^{2-}}$  and  $t_{\text{Cl}^-}$  are transport numbers of  $\text{SO}_4^{2-}$  and  $\text{Cl}^-$  ions, respectively;  $C_{\text{SO}_4^{2-}}$  and  $C_{\text{Cl}^-}$  are the average concentrations of  $\text{SO}_4^{2-}$  and  $\text{Cl}^-$  ions in the dilute solution, respectively. The transport number of ion ( $i$ ),  $t_i$  is defined by Equation 24 [96, 100].

$$t_i = z_i J_i / \sum z_i J_s \quad (24)$$

where  $\sum J_s$  denotes the total ion flux through the membrane. The flux used in Equation 22 is the absolute value. The transport of cations i.e.  $\text{Na}^+$  was not considered in the present work.

#### 4.3.5. Antifouling potential

The antifouling potential testing of the membranes was also conducted in the same four-compartment module shown in Figure 11. A mixture of 0.1 M NaCl acting as an electrolyte and 0.25 M sodium dodecylbenzene sulfonate (SDBS) as a model organic foulant was used as feed solution in compartment 2 and 3. Organic fouling is highly dependent on the concentration of foulants [106]. Membrane fouling occurs rapidly with foulant concentrations above their critical micelle concentration (CMC). To thoroughly investigate the antifouling potential of the membranes, the concentration of SDBS was chosen to be half of its CMC (0.5 M in 1.0 M NaCl) [106]. The solutions for each

compartment were circulated individually at a flow rate of 100 mL/min. The membrane surface with modification faced the dilute compartment. The applied direct current density was kept constant at 2.5 mA/cm<sup>2</sup>, which provided a total current of 19.775 mA. The potential difference across the membrane ( $\Delta E$ ) was monitored over time during the fouling process. At the beginning of the fouling experiment, the membrane potential increases gradually. When fouling takes place,  $\Delta E$  starts to increase rapidly. The time recorded until the occurrence of rapid  $\Delta E$  increase is called the transition time ( $t_{tran}$ ) [94]. The transition time is related to the membrane antifouling potential. For membranes with high antifouling potential,  $t_{tran}$  should be relatively large.

#### 4.3.6. RED performance

The power generation performance of the membranes under investigation in a RED system was evaluated in a RED stack as described in our previous work [107]. We used a polypropylene (PP) module with two titanium mesh electrodes (4 cm × 9 cm) coated with iridium plasma (FT-ED-40, Fumatech GmbH, Germany). Five and a half pairs of Fumasep FKS CEMs (Fumatech GmbH, Germany) and the investigated AEMs were alternately installed in the stack. CEMs and AEMs were separated by 500  $\mu$ m thick nonconductive spacers (Fumatech GmbH, Germany). A solution mixture of 0.05 M K<sub>3</sub>Fe(CN)<sub>6</sub>, 0.05 M K<sub>4</sub>Fe(CN)<sub>6</sub>·3H<sub>2</sub>O, and 0.25 M NaCl was used as the electrode rinse solution, which was circulated through the two electrode compartments at a flow rate of 150 mL/min. The sixth FKS CEM worked as the shielding membrane to prevent poisoning induced by hexacyanoferrate compounds to AEMs. The feed solutions used to evaluate membrane performance in RED are listed in Table 4.

Power generation performance was determined using a Vertex potentiostat (Ivium Technologies, Eindhoven, the Netherlands). A chronopotentiometry method with current density increasing from 0 to 17.92 mA/cm<sup>2</sup> in 44 levels was applied for power density measurements. Feed solutions were continuously pumped into the concentrated and dilute compartments at the same flow rate. Theoretically, the maximum obtainable gross power density (W/m<sup>2</sup>) by a RED system can be given by the open circuit voltage (OCV) and the stack resistance ( $R_{stack}$ ) as Equation 25. The generated maximum gross power was obtained from the product of measured voltage and current. The maximum gross power density was thus calculated by dividing the gross power by the total effective membrane area used in testing.

$$P_{max} = \frac{OCV^2}{4N_m R_{stack}} \quad (25)$$

where  $N_m$  is the total number of membranes used in a RED stack.

**Table 4 - Composition of testing solutions used in RED power density measurements.**

<b>Tests</b>	<b>Diluted Solution</b>	<b>Concentrated Solution</b>
Test 1	0.017 M NaCl	0.51 M NaCl
Test 2	0.0153 M NaCl, 0.017 M Na <sub>2</sub> SO <sub>4</sub> <sup>a</sup>	0.459 M NaCl, 0.051 M Na <sub>2</sub> SO <sub>4</sub> <sup>a</sup>
Test 3	0.0153 M NaCl, 0.017 M Na <sub>2</sub> SO <sub>4</sub> <sup>a</sup> 10 mg /L humic acid sodium salt	0.459 M NaCl, 0.051 M Na <sub>2</sub> SO <sub>4</sub> <sup>a</sup> 10 mg/L humic acid sodium salt

<sup>a</sup>10% molar fraction of Na<sub>2</sub>SO<sub>4</sub> to the total amount of dissolved salt. The molar percentage is equivalent for both feed solutions.

## 4.4. Results and Discussion

### 4.4.1. Membrane surface characterization

Figure 12 shows the cross-sections of the pristine CJMA-2 membrane and the chosen modified CJMA-2-7.5 membrane. For the membranes with a high number of coated layers, the LBL multilayer assembly was obvious at the surface as shown in Figure 12b and Figure 12c. With fewer coated layers, the very thin thickness made it hard to clearly determine via SEM. It has been reported that the increment in film thickness per bilayer is smaller for the first few deposited layers [108]. SEM image with higher magnification in Figure 12c shows a different inner structure of the pristine membrane and the coated layers. The native membrane has a nonporous dense matrix, while the coated layers exhibit a compactly layered lamellar structure. The detectable thickness of surface-coated films ranged from 0.88  $\mu\text{m}$  to 1.20  $\mu\text{m}$ . The thickness in the range of 3  $\mu\text{m}$  ~ 3.8  $\mu\text{m}$  with LBL coated layers above 9 layers has been reported in previous studies [100, 109]. The differences in thickness might be caused by the deposition conditions, such as the polyelectrolytes concentration, and deposition time.

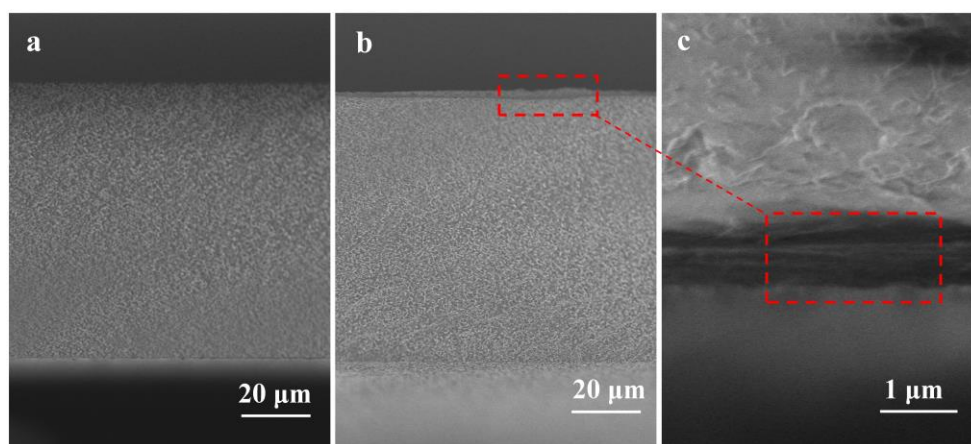


**Figure 12 - SEM images of cross-sections: (a) original CJMA-2 membrane (magnified 700 ×), (b) CJMA-2-7.5 membrane (magnified 700 ×), and (c) CJMA-2-7.5 membrane (magnified 11.0 k ×).**

When a thin multilayer thickness forms on the membrane surface, XPS is useful in determining the successful alternating deposition of PSS and PEI on a CJMA-2 membrane surface. Table 3 shows how the elemental composition (F, N, S, C, O) detected near the membrane surface obviously changed with successive coating processes. Since the CJMA-2 membrane is a standard-grade AEM, only a trace amount of S was detected at the surface before coating. Because of the sulfonic acid ( $-\text{SO}_3\text{H}$ ) and tertiary ammonium ( $-\text{NH}_2$ ) groups carried by PSS and PEI, the atomic concentration of S and N became larger as surface coated layers continued to increase. Moreover, the increased O content and decreased C/O ratio also revealed integration of the sulfonic acid ( $-\text{SO}_3\text{H}$ ) group to the membrane surface.

**Table 5 - XPS elemental compositions for the membranes.**

Membranes	Atomic Concentration (%)					
	C 1s	S 2p	N 1s	O 1s	S/N	C/O
CJMA-2	63.41	0.33	2.63	5.75	0.12	11.03
CJMA-2-4.5	68.85	1.97	3.04	9.03	0.66	7.62
CJMA-2-5.5	72.36	2.51	3.54	9.62	0.71	7.52
CJMA-2-7.5	73.76	3.61	4.95	14.12	0.73	5.22
CJMA-2-10.5	70.06	4.33	6.98	15.29	0.62	4.58

Mean surface roughness ( $S_a$ ) of the membranes provided by AFM are listed in Table 6. The surface roughness apparently increased with the number of coated layers. As shown in the surface morphology images (Figure 31), the surface of a CJMA-2 membrane is uneven, which hindered the regular complexation of PSS and PEI with the surface, and then resulted in rougher membrane surface. It has been suggested that the resultant larger contact zone of a rougher membrane surface might be beneficial for ion adhesion [110]. Compared to CJMA-2 membrane and the membranes with surface modification, ACS membrane has a much lower surface roughness due to its highly cross-linked surface layer and the uniform woven reinforcement [94].

**Table 6 - Surface roughness and contact angle of the membranes under investigation.**

<b>Membranes</b>	<b>Contact Angle [73]</b>	<b>Mean Surface Roughness (Sa, nm)</b>
CJMA-2	82.47 ± 0.93	20.13 ± 0.80
CJMA-2-1.5	76.17 ± 1.46	22.57 ± 1.60
CJMA-2-2.5	75.80 ± 0.72	25.93 ± 1.75
CJMA-2-3.5	72.68 ± 2.52	29.50 ± 2.68
CJMA-2-4.5	69.57 ± 0.88	31.80 ± 1.84
CJMA-2-5.5	69.46 ± 1.25	32.03 ± 2.42
CJMA-2-7.5	68.63 ± 0.86	32.31 ± 0.89
CJMA-2-10.5	71.20 ± 0.50	33.43 ± 2.02
ACS	72.32 ± 2.48	11.90 ± 1.48

To determine the resultant changes on hydrophilic property after surface modification, water contact angle measurements were conducted. The contact angles for the membranes with different coated layers are listed in Table 6. Since the terminated polyelectrolyte was PSS, the negatively charged sulfonic groups carried by the PSS resulted in smaller contact angles for modified membranes than that of the original CJMA-2. The contact angle for some modified membranes is slightly lower than that for the ACS membranes. The contact angle decreased to reach an optimal value at 7.5 coated bilayers, and then increased somewhat. This finding indicated that the substrate membrane was fully covered above 7.5 coated bilayers. The trend in contact angle changes has also been reported in the literature [96, 100, 111]. The decreased contact angle indicates an improved hydrophilicity of the membranes after surface modification, which will take the membranes less prone to fouling [95].

The LBL assembly of polyelectrolytes is random when there is no external force, such as an electrical field. Then, excess charge might be generated within the multilayer thin film attributing to the polyelectrolytes interpenetrating several layers [112]. Figure 13 displays the surface potential of the membranes as a function of the number of coated bilayers. The CJMA-2 and ACS membranes had a positive surface potential above 33.0 mV. The surface potential then became negative and at 4.5 coated surface layers, it hit a low point of -16.3 mV, but ascended to a minimum value of -29.65 mV at 7.5 bilayers. The surface potential is supposed to be associated with the absorbed amount of PSS and PEI at the surface [95, 96]. The tendency in surface potential showed a good agreement with the S/N ratio listed in Table 3. This suggest that the deposited amounts of polyelectrolytes in each coated layer above 7.5 bilayers were higher than that of coated samples in each of the first several layers. Moreover, the overcompensation level of PEI was likely higher than that of PSS [96] [113]. This behavior was consistent with the decrease of S/N ratio above 7.5 bilayers and explained the increasing in contact angle with 10.5 bilayers.

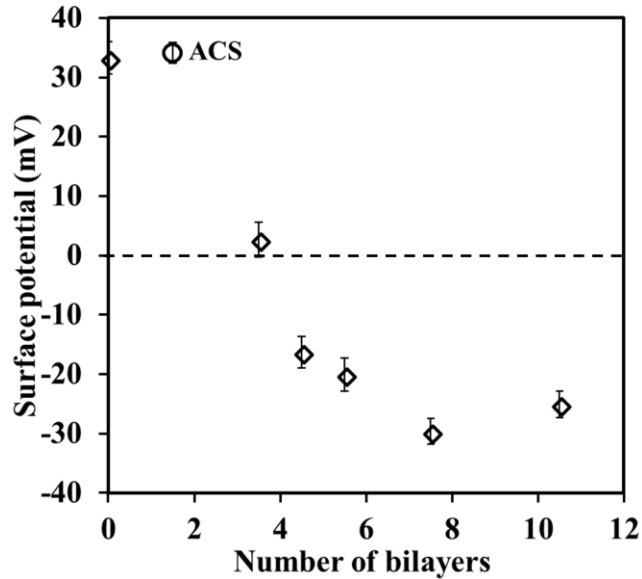


**Figure 13 - Surface potential of the membranes as a function of coated bilayers.**

#### 4.4.2. Electrochemical properties characterization

Membrane resistance and permselectivity are two important parameters determining RED power generation. The impact of surface coated layers on area resistance and permselectivity were evaluated. As listed in Table 9, after surface modification with up to 10.5 bilayers, no apparent changes to permselectivity occurred owing to the very thin multilayer thicknesses. The minimal change to permselectivity indicates that the surface coated layers can have negligible influence on  $\text{Cl}^-$  transport through the surface. As seen in Figure 14, the area resistance increased somewhat as the deposited surface layers increased. The area resistance of commercial ACS membrane was also shown for comparison. The

area resistance of ACS membrane is much higher than that of original CJMA-2 and modified membranes. As suggested by previous studies, the area resistance is highly dependent on membrane thickness [64, 114, 115]. To mimic the effect of membrane thickness on area resistance, an intrinsic property of the membrane, i.e. the intrinsic area resistance ( $\Omega$  cm), was considered (refer to Figure 14). The intrinsic area resistance was obtained from dividing the membrane area resistance by the total hydrated membrane thickness [64]. As shown in Figure 14, the intrinsic area resistance decreased after surface modification, and the optimal intrinsic area resistance was obtained at coated bilayers of 7.5. Most of the intrinsic area resistance for the modified membranes is better than that of the ACS membrane.

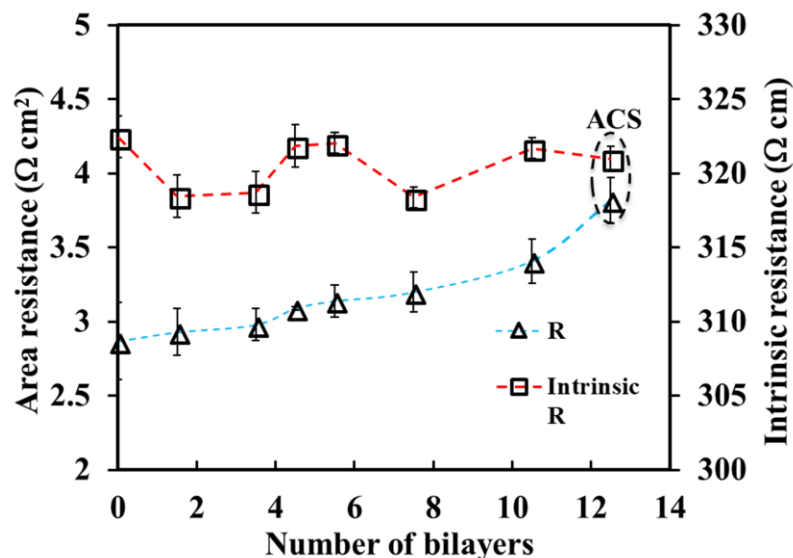


**Figure 14 - Area resistance and intrinsic area resistance of the membranes as a function of the coated bilayers. The dash lines work as the directional visual aids.**

To investigate the monovalent-ion selectivity of the membranes, the transport number ratio  $P_{SO_4^{2-}}^{Cl^-}$  was calculated based on Equation 23. In general, the current density in a typical RED system is around 2.0 - 4.0 mA/cm<sup>2</sup>. As depicted in Figure 32, the limiting current density for the membranes under investigation is around 20 mA/cm<sup>2</sup>. For all the transport number measurements, the current density of 4.0 mA/cm<sup>2</sup> (20 % of the limiting current density) was applied. The larger  $P_{SO_4^{2-}}^{Cl^-}$  value is corresponding to the better monovalent-ion selectivity [94]. As listed in Table 7, the modified membranes have decreased sulfate flux and larger  $P_{SO_4^{2-}}^{Cl^-}$  values, i.e., the improved monovalent-ion

selectivity. With 7.5 bilayers, the membrane achieved an optimal  $P_{SO_4^{2-}}^{Cl^-}$  of 2.44, which is comparable with 2.70 of commercial ACS membranes. With coated layers above 7.5 bilayers, the  $P_{SO_4^{2-}}^{Cl^-}$  value was getting lower. The tendency for the  $P_{SO_4^{2-}}^{Cl^-}$  is in good agreement with the surface potential (Figure 13). Since the Donnan-exclusion repulsive force produced by a negatively charged surface against  $SO_4^{2-}$  is stronger than that against  $Cl^-$  [116], the negatively charged coated layers on the surface rejected  $SO_4^{2-}$  more intensively than  $Cl^-$ . The negligible impacts on the apparent permselectivity and  $Cl^-$  flux suggest that the negatively charged surface introduced by LBL deposition exerted a weak repulsive force on  $Cl^-$  [117]. For ACS membranes, the lower sulfate flux and larger  $P_{SO_4^{2-}}^{Cl^-}$  can be primarily attributed to the steric exclusion mechanism due to its highly cross-linked structure on the negatively-charged surface [118].

**Table 7 - Transport number ratios for the membranes.**

Membranes	$J_{Cl^-}$ <sup>a</sup>	$J_{SO_4^{2-}}$ <sup>a</sup>	$t_{Cl^-}$	$t_{SO_4^{2-}}$	$P_{SO_4^{2-}}^{Cl^-}$
	( $10^{-8}$ mol/(cm <sup>2</sup> s))	( $10^{-8}$ mol/(cm <sup>2</sup> s))			
CJMA-2	10.32	9.53	0.52	0.48	1.10
CJMA-2-3.5	10.29	7.65	0.59	0.41	1.33
CJMA-2-4.5	10.26	6.29	0.62	0.38	1.45
CJMA-2-5.5	10.65	5.01	0.68	0.32	1.67
CJMA-2-7.5	10.60	4.33	0.72	0.28	2.44
CJMA-2-10.5	8.55	4.21	0.67	0.33	1.89
ACS	10.53	3.51	0.75	0.25	2.70

<sup>a</sup>A mixture of 0.05 M NaCl and 0.05 M Na<sub>2</sub>SO<sub>4</sub> was used as the testing solution.

#### 4.4.3. Antifouling potential

To evaluate the antifouling potential of the modified membrane, we look at the changes of transition time. The time used until fouling occurred under constant direct current, i.e., the transition time, was measured to evaluate the antifouling potential [95]. As shown in Figure 15, the transition time increased to around 52.05 ( $\pm 0.45$ ) minutes with 7.5 coated bilayers after surface coating compared to 37.60 ( $\pm 1.1$ ) minutes with no coating. This indicates that the antifouling potential could be enhanced by up to 38.43 % due to surface modification. Also, the transition time for CJMA-2-7.5 is greater than the 39.95 ( $\pm 0.65$ ) minutes for the commercial ACS membrane, which indicates a 30.29 % improvement on antifouling potential.

In terms of organic fouling, the AEM antifouling potential is generally determined by the negative surface potential, and surface hydrophilicity [119]. Since the model foulant, SDBS, is negatively charged, a negative surface potential would reduce the adsorption of negatively charged foulants through electrostatic repulsion. On the other hand, a high surface hydrophilicity also contributes to improved antifouling potential by reducing the hydrophobic interactions between organic foulants with membrane fixed charge groups. It has been demonstrated that surface roughness also affects membrane fouling [120]. Membranes with rougher surface are usually more sensitive to fouling, specifically for colloidal fouling like silica-related fouling [121]. However, for the organic fouling discussed in this work, the surface roughness increase caused by polyelectrolytes modification was shown capable of playing a minute role in membrane fouling. Dominantly, the minimal negative surface potential and high hydrophilicity resulted in largely improved antifouling potential of CJMA-2-7.5 membrane. Obviously, for

polyelectrolytes-modified membranes, especially with 7.5 bilayers, the monovalent-anion selectivity and anti-organic fouling potential were elevated simultaneously, which were expected to have better performance in the RED process.

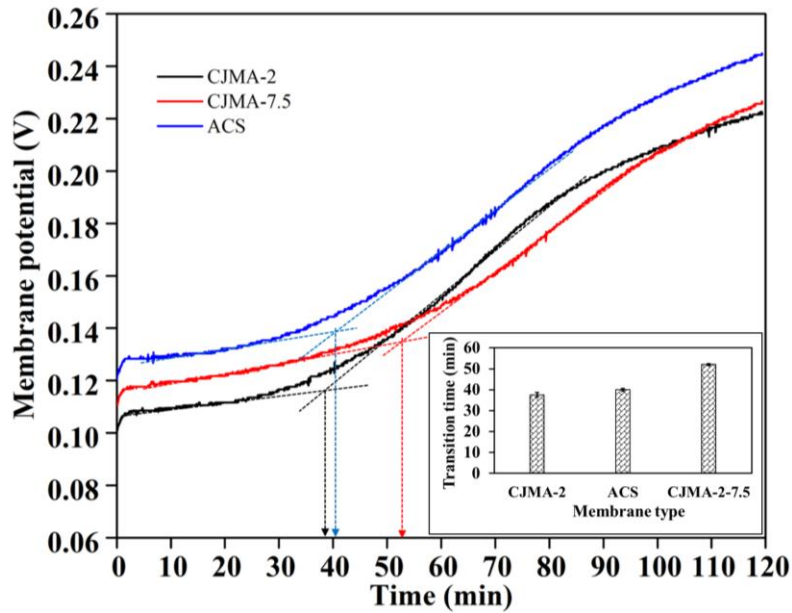


**Figure 15 - Membrane potential as a function of time under fouling condition. The feed solution contained 0.1 M NaCl and 0.25 M SDBS. The applied direct current density was kept constant at 2.5 mA/cm<sup>2</sup>. The dashed arrows work as the directional visual aids. The inserted figure shows the transition times for CJMA-2, ACS and CJMA-2-7.5 membranes, respectively.**

#### 4.4.4. Membrane performance in RED

The OCV and power generation were measured in three RED tests (listed in Table 4) at flow velocities of 0.38 cm/s, 0.76 cm/s, and 1.09 cm/s, respectively. Specifically, the OCV and gross power density for the CJMA-2, CJMA-2-7.5 and ACS membranes were compared. The OCV decreased for all three types of membranes when 10 % Na<sub>2</sub>SO<sub>4</sub> was present in the feed waters. The 10 % molar fraction of Na<sub>2</sub>SO<sub>4</sub> has been reported as the typical percentage in natural seawater and river water [28]. This decreasing tendency has been reported by other researchers [28, 29]. With comparable  $P_{SO_4^{2-}}^{Cl^-}$ , OCV measured in RED stacks with CJMA-2-7.5 membranes was close to that measured in a system with ACS membranes (Figure 34). The OCVs for CJMA-2-7.5 membranes were higher than that for CJMA-2 membranes owing to the improved monovalent-ion selectivity. When using pure NaCl as feed solutions, the gross power density obtained using CJMA-2 membranes was much higher than that obtained using the CJMA-2-7.5 and the ACS membranes (Figure 16a).

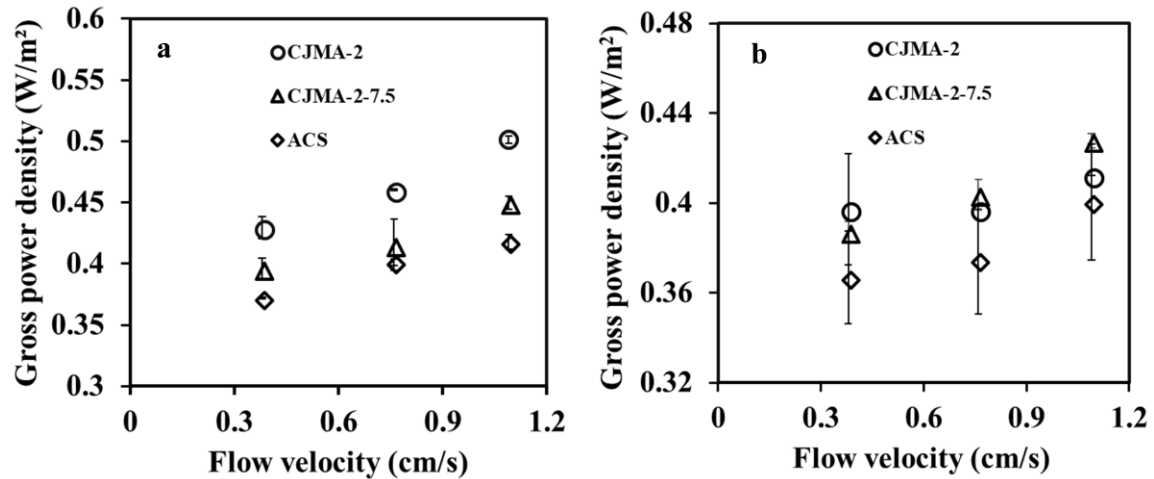


**Figure 16 - Maximum gross power density harvested as a function of different flow rates: (a) pure NaCl solution as feed waters (0.51 M for concentrated feed water and 0.017 M for diluted feed water); (b) NaCl solution with 10 % Na<sub>2</sub>SO<sub>4</sub> as feed waters (total ions concentration of 0.51 M for concentrated feed water and total ions concentration of 0.017 M for diluted feed water).**

This result might be ascribed to the relatively larger resistance of CJMA-2-7.5 and ACS membranes than that of CJMA-2 membranes. However, as shown in Figure 16b, the gross power density in RED stacks with CJMA-2 membranes dropped by 17.8 % at a higher flow velocity of 0.76 cm/s. The power generation performance of CJMA-2-7.5 membranes was getting better results than that of CJMA-2 membranes with an increasing flow rate. Many other factors, especially membrane resistance, influenced the membrane power performance regardless of the monovalent-ion selectivity and antifouling potential

[94]. The CJMA-2 membranes used in this research had a relatively large thickness and high area resistance, which explains why no significant enhancement of power production occurred with modified membranes.

When both  $\text{Na}_2\text{SO}_4$  and NOM (10 mg/L of humic acid in this case) were present in the NaCl solution feed, the OCV and power density were a function of running time as depicted in Figure 17. The OCVs for all three of the membranes under investigation decreased as expected as time elapsed, due to the uphill transport of  $\text{SO}_4^{2-}$  and membrane fouling. The stack with CJMA-2-7.5 membranes showed higher OCV compared to the stack with CJMA-2 membranes, and higher than that for the stack using ACS membranes to a lesser extent (Figure 17). Since the power density is dependent on the OCV square as expressed in Equation 25, the lowering effect was more pronounced in the obtained gross power density as shown in Figure 17b. On the other hand, the slightly increase in the stack's ohmic resistance because of the presence of sulfate and increased membrane resistance induced by membrane organic fouling also resulted in decreased gross power density based on Equation 25 [30], [122]. With much better monovalent-ion selectivity and improved antifouling potential, the stack with CJMA-2-7.5 membranes exhibited up to 17 % increased gross power density than that achieved in the stack with CJMA-2 membranes during the whole running time as shown in Figure 17b. The power density achieved with CJMA-2-7.5 membranes was not that much different from that achieved with ACS membranes. Even though the CJMA-2-7.5 membranes had a smaller area resistance and greater antifouling potential in comparison with ACS membranes, the relatively better monovalent-ion selectivity of ACS membranes somewhat compensated for the decrease in gross power density. Nevertheless, RED systems with CJMA-2-7.5 membranes did

achieve around 10% higher power density compared to the ACS membranes system. Based on the power performance of the membranes under three different RED testing conditions, the CJMA-2-7.5 membranes were much more advantageous than the standard AEM CJMA-2 and the commercial monovalent-ion selective ACS membranes when operated with natural waters, especially those seawater and river water samples containing NOM.

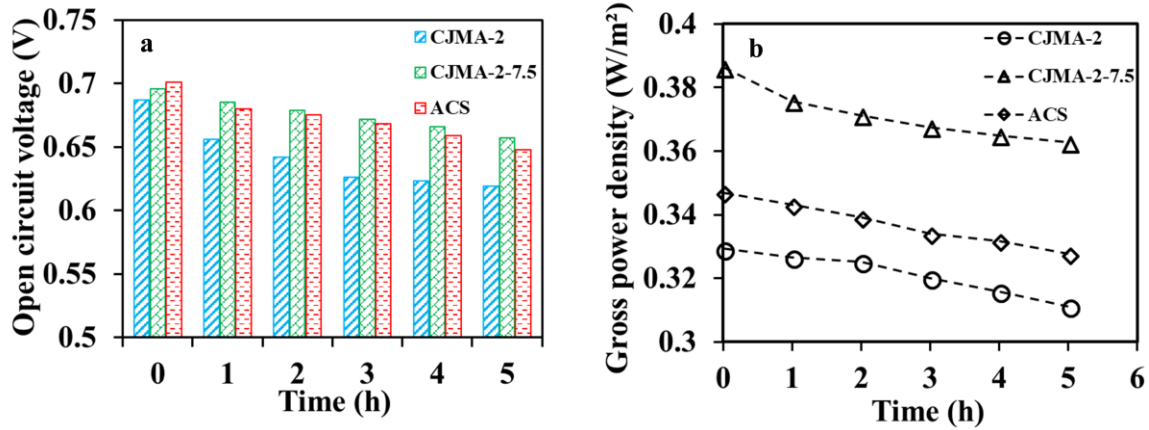


**Figure 17 - (a) Open circuit voltage as a function of time; (b) power density as a function of time. Humic acid (10 mg/L) and 10 % Na<sub>2</sub>SO<sub>4</sub> were present in both feed solutions. The feed solutions were supplied at a flow velocity of 0.38 cm/s. The dashed lines work as the directional visual aids.**

#### 4.4.5. Energy conversion efficiency

In addition to the harnessed gross power density, the maximum gross power density ( $P_{max}$ ) corresponded energy conversion efficiency ( $\eta$ ) was also evaluated for the membranes. The energy conversion efficiency is the fraction of the extractable energy to the released Gibbs free energy ( $\Delta G_{mix}$ ) by mixing feed solutions. The energy conversion efficiency is expressed as follows [123, 124]:

$$\eta = \frac{((\frac{3}{2})t_{Cl^-} - (\frac{1}{2}))^2}{2} \quad (26)$$

The equations for deriving Equation 26 were listed in equations 38 - 40. In this work, the energy conversion efficiency was calculated based on the transport numbers. The calculation is conducted based on the assumption that the influence of co-ions is negligible. Since standard-grade CJMA-2 membranes had no specific selectivity towards  $Cl^-$ , the energy conversion efficiency with CJMA-2 membranes was as low as 3.92 % (as shown in Figure 18). After surface modification,  $\eta_{max}$  was significantly increased and reached a maximum value at 7.5 bilayers. With these 7.5 coated bilayers, the energy conversion efficiency was enhanced by 3 - fold compared to the standard CJMA-2 membrane. Owing to the similar monovalent anion selectivity to that of ACS membrane, the system stacked with the CJMA-2-7.5 membranes showed comparable energy efficiency to the system equipped with ACS membranes. Combined with the enhanced antifouling potential and gross power density, the elevated energy conversion efficiency recommends the use of monovalent-ion selective and antifouling membranes as most beneficial in practical RED applications.

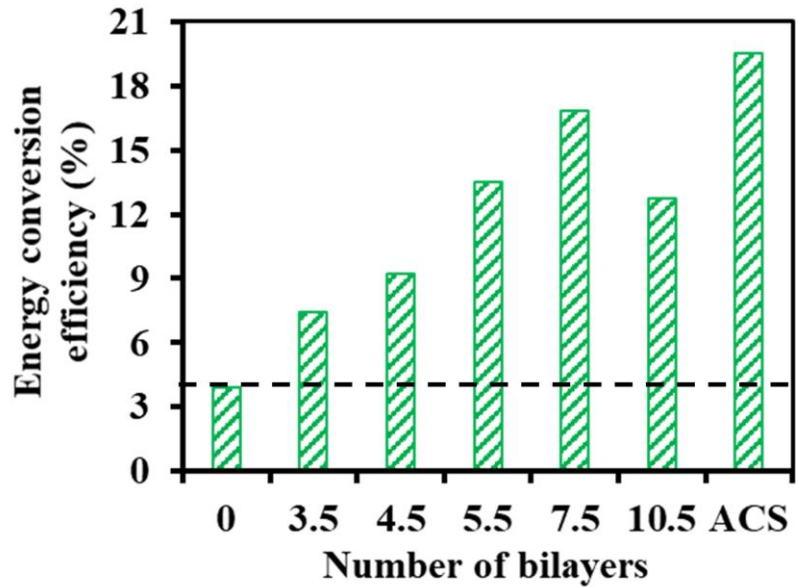


**Figure 18 - Energy conversion efficiency of modified membranes and ACS membrane compared to CJMA-2 membrane as a function of the number of bilayers. Solutions with mixtures of 0.05 M NaCl and 0.05 M Na<sub>2</sub>SO<sub>4</sub> were used. The applied current density was 4.0 mA/cm<sup>2</sup>.**

#### **4.5. Conclusions**

In this work, the surface of a standard AEM (CJMA-2) was modified with an LBL assembly of negatively charged PSS and positively charged PEI to form thin surface multilayers. The surface characteristics and electrochemical properties of the membranes were determined. After surface modification, simultaneous improvement of monovalent -

anion selectivity and anti-organic fouling potential was achieved. The simultaneous enhancement might be attributed to the strongest negatively charged surface potential and hydrophilicity of the CJMA-2-7.5 membrane. The modified membrane with 7.5 bilayers (CJMA-2-7.5) showed monovalent-anion selectivity comparable to that of the commercial ACS membranes. In terms of anti-organic fouling potential, the CJMA-2-7.5 membrane exhibited 38.43 % and 30.29 % higher than the standard CJMA-2 membrane and the commercial ACS membrane, respectively. These improved properties made the CJAM-2-7.5 membrane perform the best in a RED system. The power generation was increased by up to 17 % when running in a RED stack with the mixture of NaCl, Na<sub>2</sub>SO<sub>4</sub>, and HA as feed waters. Moreover, the energy conversion efficiency improved significantly after surface modification. The LBL modified membranes were proven to be effective in RED applications.

Because the power generation of a RED system is highly dependent on membrane area resistance, thinner membranes with lower resistance should be much better. On the other hand, if the monovalent-anion selectivity and enhanced antifouling potential can be achieved by modifying the membrane matrix instead of the surface, we could synthesize much thinner membranes with much lower area resistance. Then, RED power performance would be clearly improved.

## CHAPTER 5. 2D MXENE/GO HYBRID MEMBRANES FOR HIGHLY EFFICIENT OSMOTIC POWER GENERATION

### 5.1. Abstract

Salinity gradients have emerged as one of the more promising candidates for clean and renewable energy sources. However, the commercialization viability of present osmotic power harvesting technologies, specifically pressure retarded osmosis (PRO) in this work, are severely hindered by the unsatisfactory performance of accessible semipermeable membranes. Herein, we demonstrate the freestanding transition metal carbides (MXene) (and graphene oxide (GO) hybrid membranes as high-performance PRO membranes. Due to the elimination of internal concentration polarization (ICP), the freestanding hybrid membrane can now achieve a record-high power density up to approximately  $56.4 \text{ W m}^{-2}$  with 2.0 M NaCl as the draw solution and river water (0.017 M) as the feed water at an applied hydraulic pressure difference of 9.66 bar. In addition, the hybrid membranes exhibit enhanced antifouling potential as well as antibacterial activity. The facile fabrication of MXene and GO lamellar membranes coupled can provide a scale-up feasibility and shed light on a new membrane development platform for the highly anticipated osmotic power harvesting technologies.

### 5.2. Introduction

The intensive dependence on consumption of fossil fuels for current energy production is unsustainable due to the uncertain future of coal due to its role as a major pollutant, health hazard, and cause of global environmental issues [125]. Exploring clean and sustainable energy sources to minimize reliance on fossil fuels has been one of the

biggest global challenges. The development of a broad range of renewable energy technologies has made promising progress in clean energy production [126]. Among these technologies, salinity gradient power (SGP), also termed as osmotic energy, is an emerging renewable energy resource that has not been fully tapped. When two solutions with different salinities are mixed, Gibbs free energy is released which can be harvested as clean energy through membrane-based technologies [2, 34, 127]. Considering the major rivers flowing into the oceans globally, the SGP has been estimated to hold a potential up to 2000 TWh/year [44, 128]. Pressure retarded osmosis (PRO) has been identified as a promising technology to harness SGP from both natural and anthropogenic streams with a controlled mixing process [9, 10]. In addition to the river water and seawater as the input streams, solution pairs with larger salinity gradients arising from the desalination brine/wastewater effluent, and hypersaline water (Dead Sea or Salt Lake), and river water have been proposed to increase osmotic power [4-8, 129]. In a PRO system, the osmotic pressure difference is exploited to drive water permeation from a diluted solution (feed) to a concentrated solution (draw) through a semipermeable membrane. A pressure exchanger is utilized to apply a hydraulic pressure less than the osmotic pressure difference to the draw solution, and the mechanical energy generated from the expanding of draw solution volume is extracted as electricity by a mechanical energy conversion device such as a hydro-turbine [10]. The power output from a PRO system can be obtained by the applied hydraulic pressure difference to the draw solution ( $\Delta P$ ) multiplied by the volume through the hydro-turbine, which is equivalent to the volume of solution across the membrane ( $\Delta Q$ ) [130].

Despite PRO holding great potential for sustainable energy production, the advancement of this technique has been hindered by limited accessibility to the desirable membranes. Many efforts have been made to design effective PRO membranes such as thin film composite (TFC) flat sheets and hollow-fiber PRO membranes [37]. The porous support layers of TFC membranes induce severe internal concentration polarization (ICP), which cause a dramatic decrease in the effective water permeation driving force across the active layer of the membrane [131]. Hence, the water flux is significantly reduced and consequently, the generated energy is much lower than expected. Although the power density achieved through PRO system with TFC membranes has been reported as higher than the commercialization viability benchmark of  $5 \text{ W m}^{-2}$ , the PRO performance is still limited by the presence of ICP and relatively low water permeability. Recently, support-free, freestanding membranes have been proposed to significantly mitigate the ICP [132], which is highly favorable for PRO application.

In addition, PRO membranes appear to suffer from severe membrane fouling, especially, when using the combination of wastewater effluent and seawater reverse osmosis (SWRO) as feed and draw streams [133, 134]. Typically, state-of-the-art PRO membranes hold a porous support layer facing the feed solution in a PRO system. Thus, foulants and microbes in feed water can be easily transported into the porous structure and accumulate in it, which deteriorates the ICP [135]. Consequently, this membrane fouling becomes detrimental to the membrane water flux, the achievable PRO power production, and the membrane lifetime. The organic fouling is partially reversible with backwash cleaning, while the biofouling is hard to be reversed even with chemical cleaning

procedures [7, 136, 137]. So far, limited studies have been performed on developing PRO membranes with enhanced anti-fouling potential.

Due to its versatile chemical modification, facile fabrication, strong mechanical strength, ultrafast water transport and superior ion selectivity, graphene oxide (GO) membranes have opened a new stage of two-dimensional (2D) material assembled thin membranes for applications in water desalination and separation [138, 139]. However, the poor water stability of GO membranes has potentially restricted the scale-up viability. In the last several years, an emerging family of 2D transition metal carbides and nitrides, referred to as MXene, has attracted increasing attention. The functional groups (O, -OH, and -F) are introduced evenly at the nanosheet surface through in-situ etching and exfoliating processes [140, 141]. The abundant functional groups render MXene nanosheets as negatively charged units with a hydrophilic surface, which remarkably facilitates the water and ion transport through the ordered nanochannels. More importantly, MXene membranes have been reported to resist disintegration in water [21, 142]. In a previous work [143], freestanding GO membranes indicated a potential in PRO power harvesting. However, the membrane performance in the PRO system is potentially limited by relatively low water permeability as well as low burst pressure due to the disintegration of GO membranes. The fabrication of heterostructures by assembling different building blocks emerge as an attractive strategy to combine the advantages and mitigate the shortcomings of the individual materials [144]. In recent years, the 2D heterostructures have been increasingly investigated as beneficial to energy storage due to their excellent capacitance and electronic conductivity [145]. The attention being paid to the application

of 2D heterostructures in water separation and osmotically driven membrane processes is rather limited.

Herein, to the best of our knowledge, this is the first work on the fabrication of freestanding MXene/GO hybrid lamellar membranes as high-performance PRO membranes for harvesting osmotic energy. The hybrid membranes were fabricated with 2D MXene and GO nanosheets as two building blocks by a vacuum-assisted filtration. The combination of MXene and GO nanosheets endows the hybrid membranes with enhanced water stability and resultant burst pressure. The mass transport properties of the membranes and the PRO power output were determined in detail. Additionally, the membrane antifouling potential against macromolecular foulants and microbial foulants were also well investigated. Our findings in the present work highlight the promise of practical application viability of MXene/GO hybrid membranes as a highly anticipated osmotic power generation platform.

### **5.3. Experimental Section**

#### *5.3.1. Materials*

MAX ( $\text{Ti}_3\text{Al}_2$ ) powder was obtained from Luoyang Tongrun Info Technology Co., Ltd, China. Lithium fluoride (LiF, 99.85 %, metals basis) was purchase from Alfa Aesar, Ward Hill, MA, U.S. Hydrochloride (HCl, 37%, ACS reagent), Sodium chloride (NaCl, 99.0%) and humic acid sodium salt were supplied by Millipore Sigma, Billerica, MA, U.S. All the chemicals were used as received. The Anodic membranes (AAO) were purchased from Whatman (GE Healthcare, U.S.). Deionized (DI) water produced by a Barnstead nanopure system (Thermo Scientific, U.S.) was used for all the experiments.

### 5.3.2. Fabrication of MXene/GO hybrid membranes

LiF of 1.32 grams was dissolved in 20 mL of 6 M HCl solution under stirring for 10 min. Then, 2 g  $\text{Ti}_3\text{AlC}_2$  powder (MAX) was slowly added to avoid initial overheating of the exothermic reaction [146]. After etching at 40 °C for 60 h under magnetic stirring, the resulting solution was washed with D.I. water through several cycles of centrifugation (5 min for each cycle at 3500 rpm), until the pH value of the supernatant reached ~ 6. To delaminate  $\text{Ti}_3\text{C}_2\text{T}_x$  into 2D nanosheets (*d*- $\text{Ti}_3\text{C}_2\text{T}_x$ , MXene), the obtained sediments were redispersed into 100 mL of DI water followed by ultrasonication for 2 h under flowing Argon gas. The stable MXene colloidal solution in a dark green color was collected after centrifuge at 3500 rpm for 1h.

Graphene oxide (GO) was synthesized based on a modified Hummer's method. The synthesis steps in detail are as follows: 3g of graphite and 1.5 g of sodium nitrate were added into 75 mL concentrated sulfuric acid under stirring in an ice bath at 0 °C for 1h. Afterwards, 9.0 g  $\text{KMnO}_4$  was carefully added over the course of 20 min with temperature kept below 20 °C. The temperature was subsequently increased to 35 °C and kept at  $35 \pm 3$  °C for 30 min. Afterwards, 150 mL DI water was added slowly into the mixture with an elevated temperature of 98 °C for another hour under stirring. Finally, the mixture was cooled to room temperature followed by the addition of 400 mL DI water and 9 mL  $\text{H}_2\text{O}_2$  (30% wt %) to stop the oxidation reaction. The obtained product was washed with 1 M HCl solution and a large amount of DI water until reaching a pH ~ 5. The yellowish GO colloidal solution was collected with the aid of a centrifuge at 3000 rpm for 30 min.

A specific amount of MXene solution ( $0.5 \text{ mg mL}^{-1}$ ) was mixed with various portions of GO solution ( $0.1 \text{ mg mL}^{-1}$ ), followed by sonication in an ice bath for 10 min to

obtain homogenous MXene/GO solutions. The resulting mixture was filtered onto the Anodic inorganic filters (AAO, average pore size 0.2  $\mu\text{m}$  and a diameter of 47  $\mu\text{m}$ ) via vacuum-assisted filtration. The flexible and freestanding membrane could be easily detached from the substrate after drying. The obtained membranes are named as  $d\text{-Ti}_3\text{C}_2\text{T}_x/\text{GO-X}$ , where X denoting the weight percentage of GO contents in the hybrid membrane.

### 5.3.3. Characterization of 2D materials and membranes

High-resolution transmission electron microscopic images and a selective area electron diffraction pattern of  $d\text{-Ti}_3\text{C}_2\text{T}_x$  and GO nanosheets were captured using a scanning transmission electron microscope (HD 2700, Hitachi High Technologies America, Inc., Schaumburg, IL, U.S.). The atomic compositions were examined by Thermo  $\text{K}\alpha$  X-ray photoelectron spectroscopy (Thermo Scientific, Waltham, MA, U.S.). The inter-layer spacing of the membranes were analyzed by the X' Pert PRO Alpha-1 X-ray diffraction (XRD) with Cu  $\text{K}\alpha$  radiation at the step scan of 0.02  $^\circ$ , with an overstep time of 0.05 s. The surface morphology and roughness of the membranes was characterized using the Agilent 5500 atomic force microscopy (AFM, Agilent Technologies, Inc., Santa Clara, CA, U.S.). The tensile stress characterization was performed on a Model Q800DMA tester (TA Instruments Co., New Castle, DE, U.S.) with a loading rate of 2 N/min. The membrane samples were cut into stripes with a length of 30 mm and a width of 4 mm. The Young's modulus was calculated by the slope of the linear region of the stress-strain curves. The zeta potential of MXene and GO solutions (0.01  $\text{mg mL}^{-1}$ ) was carried out on a Malvern Zetasizer Nano S (Malvern Instruments, Inc., Westborough, MA, U.S.).

#### 5.3.4. Determination of membrane transport properties

To better mimic the membrane transport properties and accurately predict the harvestable power density in the PRO operation, pure water permeability coefficient ( $A$ ), salt permeability coefficient ( $B$ ) and salt rejection ( $R$ ) of the investigated membranes were determined through a modified reverse osmosis (RO) test cell (Figure 35). In the modified RO cell, the porous frit on the permeate side of a membrane was replaced by a feed spacer with two layers of strands (Figure 35) to simulate the deformation condition of the pressurized membranes in a PRO test [147]. The feed and permeate channels in the revised RO experiment were used as the draw solution and feed channels of the PRO test cell. The effective membrane area in the RO cell was  $4.1 \text{ cm}^2$ . The feed solution (i.e., pure DI water) was circulated at a flow rate of  $0.38 \text{ L min}^{-1}$ . The permeate was collected and measured by a digital balance to obtain the water flux ( $J_w$ ), from which the water permeability coefficient was determined over various hydraulic pressure differences from 3.45 to 13.79 bar with 1.38 bar increments. The tested membrane was first compacted with DI water at an applied hydraulic pressure of 3.45 bar for 2h to reach a steady state permeate flux. Water permeability was calculated from dividing the measured pure water flux by the applied hydraulic pressure ( $\Delta P$ ) as shown in Equation 27 [148]. The salt permeability coefficient was given based on Equation 28 [43]:

$$A = \frac{J_w}{\Delta P} \quad (27)$$

$$B = \frac{A(1-R)}{R} (\Delta P - \Delta \pi) \quad (28)$$

where  $R$  is the rejection of 0.05 M NaCl determined through the modified RO test at an applied hydraulic pressure of 8.28 bar, which was calculated from the concentration of feed

solution ( $C_F$ ) and the permeate ( $C_P$ ). The concentrations were obtained from the measured electrical conductivity of the solutions using a conductivity meter (Extech Instruments Corp., Waltham, MA, USA).

#### 5.3.5. *Membrane performance in PRO tests*

The membrane mass transport properties in the PRO process were evaluated in a PRO testing cell under crossflow mode without external hydraulic pressure (shown as Figure 19). NaCl solutions with a concentration in the range of 0.5 M - 2.0 M and DI water were employed as draw solution and feed solution, respectively. Throughout the tests, the draw solutions and feed solutions were circulated, separately. The effective area of the membranes under testing was shaped to 1 cm<sup>2</sup>, and the velocity was maintained at 27.8 cm s<sup>-1</sup>. In terms of the commercial CTA membrane, the active layer was placed to face the draw solution for the PRO tests. The weight changes of the feed solution were recorded every 2 min, and the average stable water flux was calculated after over 3 h of testing.

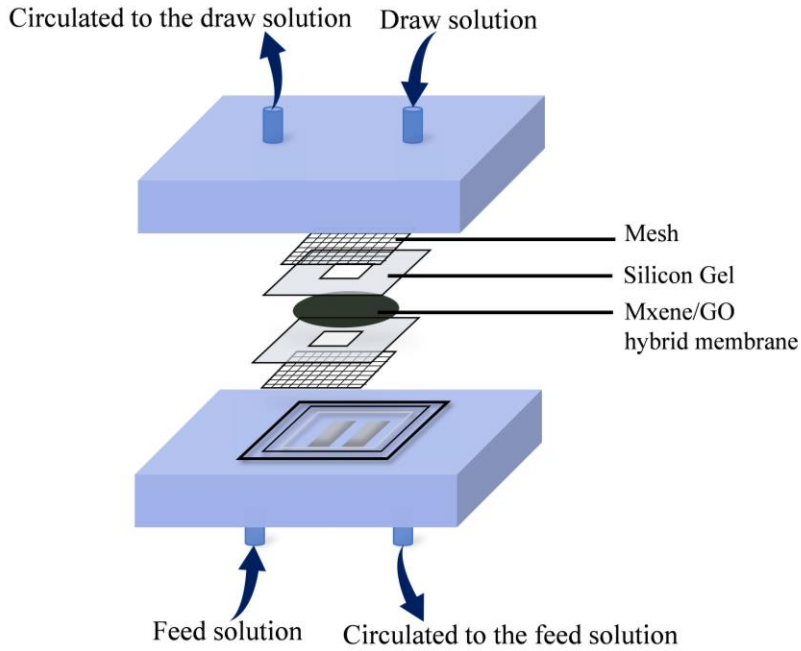


**Figure 19 - The schematic of PRO testing cell.**

In the osmotically driven membrane processes, the non-ideal semi-permeable membranes suffer from reverse solute diffusion, that is, a small portion of the salt permeating the membrane from the draw solution to the feed solution driven by the chemical potential arising from the salt concentration difference. The reverse salt permeation results in a reduced effective osmotic pressure difference across the membrane. The reverse salt flux,  $J_s$ , is the product of the draw solution concentration at the active layer interface and the membrane parameter B. Thus,  $J_s$  is defined as follows [149]:

$$J_s = BC_{D,b} \exp\left(-\frac{J_w S}{D}\right) \quad (29)$$

where  $C_{D,b}$  is the bulk concentration of the draw solution,  $S$  is the structural parameter of the support layer, and  $D$  is the diffusion coefficient of the NaCl in the draw solution.

The structural parameter  $S$  is obtained as follows [150]:

$$S = \left(\frac{D}{J_w}\right) \ln\left(\frac{B+A\pi_{D,b}}{A\pi_{F,b}+B+J_w}\right) \quad (30)$$

where  $\pi_{D,b}$  is the osmotic pressure of the bulk draw solution, and  $\pi_{F,b}$  is the osmotic pressure of the bulk feed solution. In this work, DI water was used as the feed solution and the osmotic pressure was 0 bar.

### 5.3.6. Water flux and the projected power density

With water diffusing across the active layer of the salt-rejecting membrane, the solutes in draw solution transport across the membrane to compensate the diluted draw solution, resulting in an increased local concentration at the active layer-support layer interface, termed as the concentrative internal concentration polarization (ICP). Alternatively, the permeating water from the feed solution dilutes the draw solution at the active layer, resulting in the dilutive external concentration polarization (ECP). A schematic diagram of the salt concentration profile across a PRO membrane is shown in Figure 20. By incorporating the performance-limiting factors, ICP and ECP, as well as reverse salt diffusion, the water flux in PRO can be expressed by [35]:

$$J_w = A \left\{ \frac{\pi_{D,b} \exp\left(-\frac{J_w}{k}\right) - \pi_{F,b} \exp(J_w K)}{1 + \frac{B}{J_w} [\exp(J_w K) - \exp\left(-\frac{J_w}{k}\right)]} - \Delta P \right\} \quad (31)$$

where  $\pi_{D,b}$  and  $\pi_{F,b}$  are the osmotic pressure of the bulk draw and feed solutions, respectively.  $K$  is the resistance to diffusion (solute resistivity) of the membrane support

layer, which can be expressed as  $SD^{-1}$ , and  $k$  is the mass transfer coefficient related to the concentration polarization near the membrane surface in the feed channel.

The PRO power density is the product of the water flux through the membrane and the applied hydraulic pressure difference across the membrane as shown in Equation 32. The maximum power density was achieved at  $\Delta P = \Delta\pi/2$  [10].

$$W = J_w \Delta P \quad (32)$$

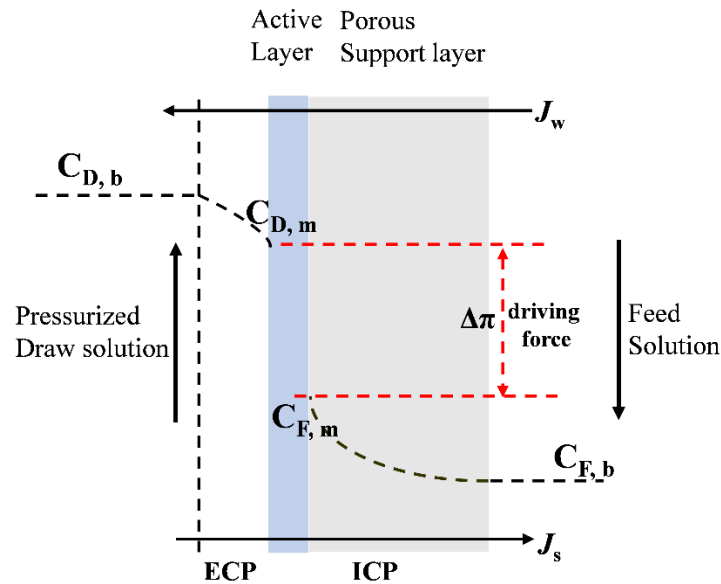


**Figure 20 - A schematic diagram of the salt concentration profile across a PRO membrane.**

### 5.3.7. Determination of antifouling potential of the membranes

The membrane anti-organic fouling was investigated with humic acid (HA) as the model foulant. The membranes under investigation were first compacted for 2 h under an applied hydraulic pressure of 3.45 bar to reach a steady water flux. The water flux was recorded for another hour to obtain the pure water flux ( $J_0$ ). Subsequently, the pure water was converted to the HA solution of 30 mg L<sup>-1</sup> and remained running for 5 h at the same flow rate and applied hydraulic pressure. The steady flux with HA solution as feed was recorded as  $J_t$ . Then, the fouled membrane was physically cleaned with DI water. After physical cleaning, the recovered pure water flux ( $J_r$ ) was recorded for 1h with DI water. The flux decline ration (FDR) coupled with water flux recovery ratio (FRR) are used to evaluate the membrane anti-fouling potential as calculated based on the following equations. Generally, the lower FDR and the higher FRR indicate a better antifouling potential of the membranes [151].

$$FDR = \left(1 - \frac{J_t}{J_w}\right) \times 100\% \quad (33)$$

$$FRR = \frac{J_r}{J_w} \times 100\% \quad (34)$$

The antibacterial activity of the membrane was evaluated against the Gram-negative bacterium, *Escherichia coli* (ATCC 10798) by a colony-forming unit (CFU) enumeration assay. Briefly, the membranes were exposed to the bacterial suspension ( $10^7$  CFU mL<sup>-1</sup>) for 5 h at room temperature. Afterwards, the excess bacterial suspension was discarded, and the membranes were rinsed with 10 mL saline solution (0.9 wt %) to remove unattached cells from the membrane surface. The rinsed membranes were then transferred to a 20 mL saline solution to detach bacteria from the membrane surface via bath sonication

for 10 min. The resulting supernatant was immediately inoculated on a Luria-Bertani broth (LB) medium and cultured overnight at 37 °C.

## 5.4. Results and discussion

### 5.4.1. Characterization of 2D nanosheets and the membranes

Ti<sub>3</sub>C<sub>2</sub>T<sub>x</sub> MXene nanosheets were obtained by selective etching of the Al layer from the Ti<sub>3</sub>AlC<sub>2</sub> (MAX phase) using in-situ hydrofluoric (HF) forming etchant, lithium fluoride and HCl (hydrochloric acid) [152] (Figure 36). The TEM images of the delaminated MXene nanosheets (*d*-Ti<sub>3</sub>C<sub>2</sub>T<sub>x</sub>) shows a single layer or fewer layers as well as well-defined edges with no wrinkles at the surface (Figure 21a and 21c), which is different from GO nanosheets (Figure 21b). The high-resolution transmission electron microscopy (HRTEM) image and the selected-area electron diffraction pattern (SAED) confirmed the hexagonal structure and high crystallinity of the MXene nanosheets without apparent defects (Figure 21d). While, GO nanosheets show an amorphous structure. What's more, the lateral size of MXene and GO nanosheets were shown to be approximately 2 to 3 μm, which has been suggested to be feasible to construct ordered 2D lamellar membranes [153].

The rich terminating functional groups (-O, -OH and -F) for and groups (-COOH, -OH, -O-) for GO were identified by XPS analysis (Figure 22). These abundant functional groups render the nanosheets negative charge in aqueous solutions, as indicated by the negative ζ-potential of the colloidal solutions of MXenes and GO (Figure 37).

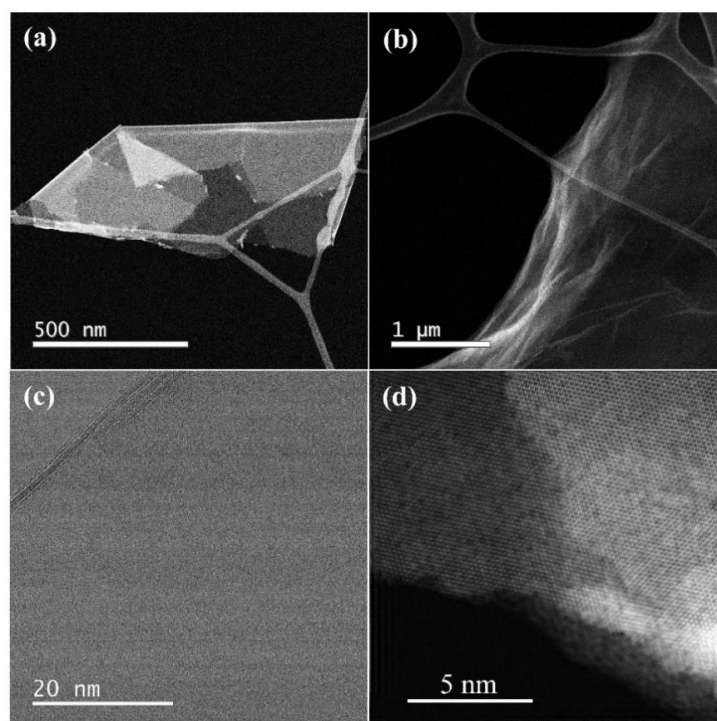


**Figure 21 - Morphology and structure of the  $d\text{-Ti}_3\text{C}_2\text{T}_x$  and GO nanosheets. TEM images of (a)  $d\text{-Ti}_3\text{C}_2\text{T}_x$  and (b) GO nanosheets. The HRTEM images of the (c) layers of the  $d\text{-Ti}_3\text{C}_2\text{T}_x$  nanosheets and (d) the high crystallinity of the  $d\text{-Ti}_3\text{C}_2\text{T}_x$ .**

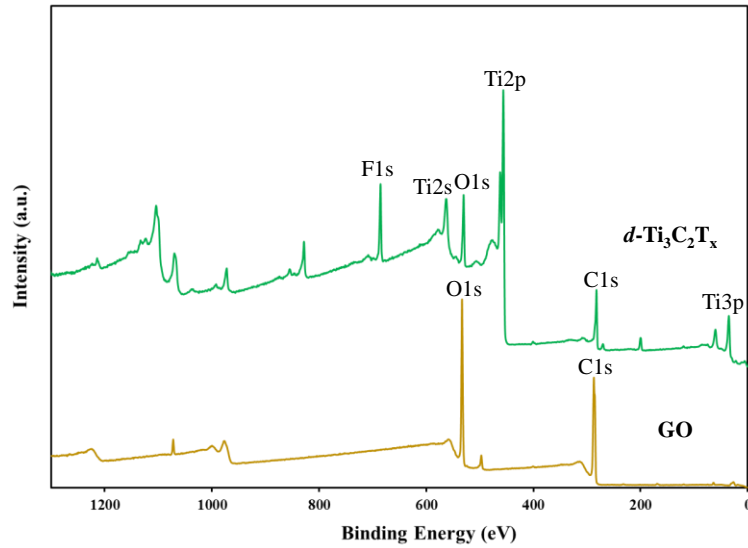


**Figure 22 - The XPS survey spectra of  $d\text{-Ti}_3\text{C}_2\text{T}_x$  and GO nanosheets.**

The shift of the diffraction peak from  $9.8^\circ$  (MAX power) to a lower angle  $6.3^\circ$  for MXenes in XRD patterns (Figure 23a) indicates the successful synthesis of delaminated MXene nanosheets ( $d\text{-Ti}_3\text{C}_2\text{T}_x$ ), which is in good agreement with results reported in the literatures [154, 155]. The XRD pattern with a sharp peak (002) at ( $2\theta = 6.3^\circ$ ) further confirms the well-ordered and uniform lamellar structure of the MXene membrane with an interlayer spacing of ( $d = 14.06 \text{ \AA}$ ). The single peak (001) with high intensity at ( $2\theta = 11.3^\circ$ ) of the pure GO membrane indicates the  $d$ -spacing of  $7.79 \text{ \AA}$ . The as-prepared  $d\text{-Ti}_3\text{C}_2\text{T}_x/\text{GO}$  hybrid membranes at varied ratios also show an ordered lamellar structure as displayed in XRD patterns. As demonstrated in Figure 23b, the shifting peaks originated

from the weight variations of GO in the hybrid membranes. The increasing weight ratio of GO in the hybrid membranes led to a  $d$ -spacing that is smaller than the pure MXene membranes while larger than the pure GO membrane, which could be attributed to the intercalation of  $d$ -Ti<sub>3</sub>C<sub>2</sub>T<sub>x</sub> nanosheets between the GO nanosheets. Also, more GO content resulted in a less uniform membrane structure due to the self-assembly of the nanoflakes during the vacuum-assisted filtration process. At a fully hydrated state, the intercalation of water molecules inside the interplanar channels of the membrane enlarged the  $d$ -spacing from 8.52 Å for the dry membrane to 9.73 Å.

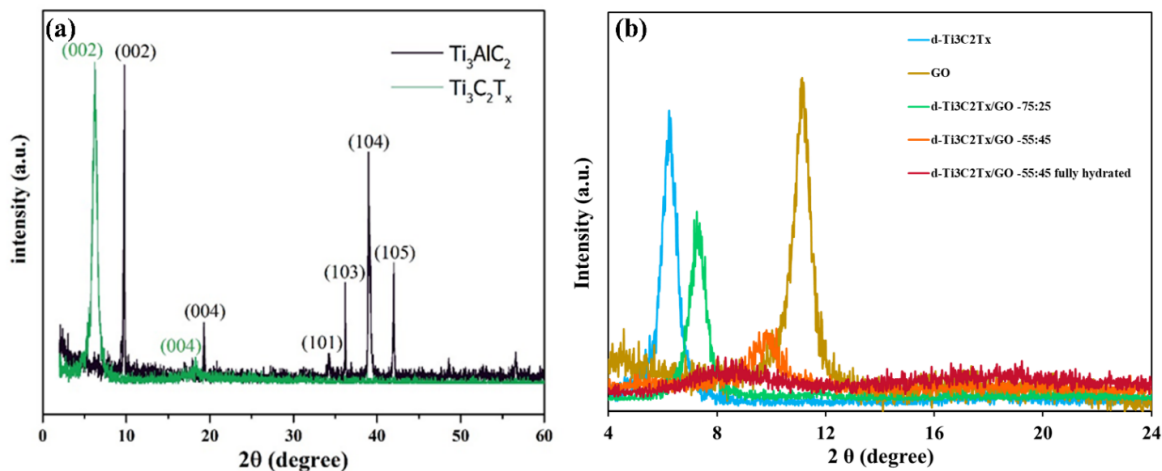


**Figure 23 - The XRD patterns of (a) MAX phase and  $d\text{-Ti}_3\text{C}_2\text{T}_x$  power and (b) pristine and hybrid MXene/GO membranes.**

#### 5.4.2. Water and salt permeability coefficients of the membranes

The influence of  $d\text{-Ti}_3\text{C}_2\text{T}_x/\text{GO}$  weight ratios on membrane water permeability coefficient (A) was investigated. The pristine MXene thin membrane offered a water permeability coefficient as high as  $18.11 \text{ L m}^{-2} \text{ h}^{-1} \text{ bar}^{-1}$  (LMH-bar). The high water permeability of MXene membranes has been confirmed in the literature [156]. As demonstrated in Figure 24a, with the increasing weight ratio of GO in the hybrid membranes, the water permeability coefficient largely decreased in comparison with the pure MXene membrane. However, even if the water permeability decreased to 7.76 LMH-bar for the membrane  $d\text{-Ti}_3\text{C}_2\text{T}_x/\text{GO}$  weight percentage ratio of 55:45 (termed as  $d\text{-}$

$\text{Ti}_3\text{C}_2\text{T}_x/\text{GO}$  -45), the water permeability is still much higher than that of a commercial CTA membrane (1.09 LMH-bar). To withstand the applied external hydraulic pressure in the PRO process, the membranes holding high burst pressure are favorable to the PRO performance. The pristine MXene membrane shows relatively low mechanical strength, which is primarily attributed to the poor interconnection between adjacent MXene nanosheets. In our previous work, the GO lamellar membrane was reported to show excellent mechanical strength. The  $d\text{-Ti}_3\text{C}_2\text{T}_x/\text{GO}$  hybrid membrane displayed remarkably enhanced mechanical property (Table 10). Due to the existence of active functional groups on MXene and GO nanosheets, it is supposed that there are sufficient hydrogen bonds formed between the  $d\text{-Ti}_3\text{C}_2\text{T}_x$  and GO nanosheets. The enhanced mechanical strength is beneficial to render membranes satisfying burst pressure. With the GO contents in the hybrid membranes increased to 45%, the burst pressure of the  $d\text{-Ti}_3\text{C}_2\text{T}_x/\text{GO}$  -45 membrane reached to 9.66 bar. While, further increment on GO contents up to 60% did not give rise to higher burst pressure. This phenomenon might be explained in the concept of the membrane water stability. GO membranes have been known to disintegrate in water due to the deprotonation of carboxyl groups. However, the MXene membranes can maintain integrity upon hydration. As a result, the membrane with higher GO content is assumed to have poor water stability.

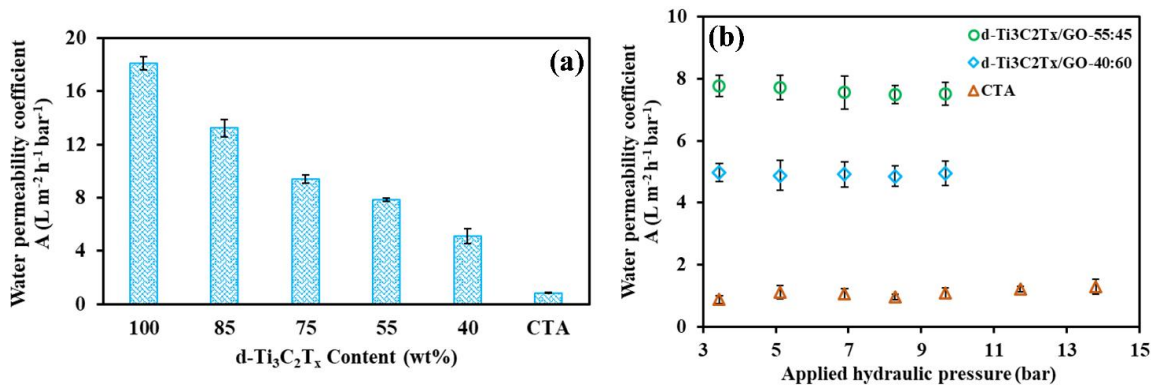


**Figure 24 - Water permeability coefficient,  $A$ , as a function of (a)  $d\text{-Ti}_3\text{C}_2\text{T}_x$  weight percentage in the hybrid membrane at an applied hydraulic pressure of 3.45 bar. (b) varied applied hydraulic pressure. For all the membranes, the parameter  $A$  was determined through the modified RO cell under crossflow mode.**

#### 5.4.3. Water flux and projected PRO power density

The water flux with respect to NaCl concentration in PRO was measured using the  $d\text{-Ti}_3\text{C}_2\text{T}_x/\text{GO}-45$  membrane as the optimal membrane. The commercial CTA membrane was also studied for comparison. As shown in Figure 25, for the  $d\text{-Ti}_3\text{C}_2\text{T}_x/\text{GO}-45$  membrane, the water flux showed an almost linear relationship with the concentrations of draw solution and substantially increased with the NaCl concentration ranging from 0.5 M to 2.0 M. The water flux reached a value up to  $185.37 \text{ L m}^{-2} \text{ h}^{-1}$  (LMH) at an NaCl concentration of 2.0 M, which is approximately 5 times higher than that obtained with a

commercial CTA membrane (38.61 LMH). With the freestanding  $d\text{-Ti}_3\text{C}_2\text{T}_x/\text{GO-45}$  membrane, due to the significant reduction of the internal concentration polarization (ICP), the maximized osmotic pressure drive force leads to a substantial increase of the water flux. In terms of the reverse draw solute flux, a similar trend to that of the water flux was observed as expected. The increased reverse salt flux with the increasing draw solution concentration was induced by the higher Nernst potential difference at high draw solution concentration. The reverse flux selectivity, i.e., the ratio of water flux and reverse salt flux,  $J_w/J_s$ , has been acknowledged as an important parameter to evaluate PRO membrane performance [157]. For the  $d\text{-Ti}_3\text{C}_2\text{T}_x/\text{GO-45}$  membrane, the average reverse flux selectivity was determined as approximately  $838.7 \pm 53.9 \text{ L mol}^{-1}$ , which is higher than the results reported in the literature [132]. The high reverse flux selectivity suggests the feasibility of the  $d\text{-Ti}_3\text{C}_2\text{T}_x/\text{GO-45}$  membrane for high PRO performance.

By incorporating the measured pure water permeability (A) and salt permeability (B), the membrane structural parameter (S) was calculated to be  $57 \mu\text{m}$ , which is remarkably smaller than that of a commercial CTA membrane (Table 11). The parameter S is an intrinsic characteristic related to the ion transport in the membrane support layer [35]. The freestanding  $d\text{-Ti}_3\text{C}_2\text{T}_x/\text{GO-45}$  membrane with mitigation of ICP offered the membrane a much lower structural parameter. The higher water permeability coupled with a lower structural parameter is favorable for PRO power output. However, it was found that the salt permeability of the  $d\text{-Ti}_3\text{C}_2\text{T}_x/\text{GO-45}$  membrane is larger than that of the commercial CTA membrane, which will potentially sacrifice the power performance to some extent. The dense active layer of the CTA membrane renders a membrane high salt rejection. For the  $d\text{-Ti}_3\text{C}_2\text{T}_x/\text{GO-45}$  membrane, the  $d$ -spacing is larger than the radius of

the salt ions, especially with the  $d$ -spacing becoming enlarged upon hydration, which was responsible for the relatively low salt rejection.

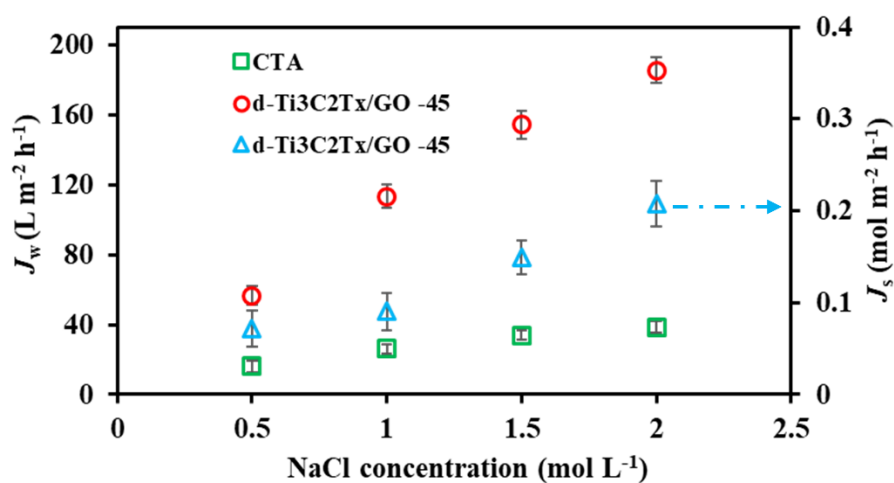


**Figure 25 - Water flux ( $J_w$ ) and reverse draw salt flux ( $J_s$ ) of  $d$ -Ti<sub>3</sub>C<sub>2</sub>Tx/GO-45 and commercial CTA membranes. Tests were performed in an FO cell with effective membrane area of 1 cm<sup>2</sup> and a crossflow velocity of 27.8 cm s<sup>-1</sup> with different concentrations of NaCl as the draw solution and DI as the feed solution for 2h. At least three membranes testing were conducted at room temperature.**

The theoretical power density of the  $d\text{-Ti}_3\text{C}_2\text{T}_x/\text{GO-45}$  membrane under different applied hydraulic pressures showed a difference in NaCl draw solution concentrations varying from 0.5 M to 2.0 M as illustrated in Figure 26. The feed solution of 0.0017 M NaCl was used to simulate river water. As the applied hydraulic pressure difference increased, the power density was substantially enhanced. A higher power density can also be achieved with a higher concentration of NaCl in the draw solution at the same hydraulic pressure difference. The  $d\text{-Ti}_3\text{C}_2\text{T}_x/\text{GO-45}$  membrane was able to withstand a hydraulic pressure difference of up to 9.66 bar in our case. The power density was calculated to be  $19.4 \text{ W m}^{-2}$ ,  $38.1 \text{ W m}^{-2}$ ,  $48.8 \text{ W m}^{-2}$ , and  $56.4 \text{ W m}^{-2}$  for the draw solution concentration of 0.5 M, 1.0 M, 1.5 M, and 2.0 M, respectively. The maximum power density can be obtained at an applied external hydraulic pressure difference equivalent to approximately half of the osmotic pressure. Since, the burst pressure of the  $d\text{-Ti}_3\text{C}_2\text{T}_x/\text{GO-45}$  membrane is lower than half the osmotic pressure, the calculated power density for a  $d\text{-Ti}_3\text{C}_2\text{T}_x/\text{GO-45}$  membrane is lower than the maximum value (as shown in Figure 38). The economical commercialization benchmark of PRO power density has been reported at  $5 \text{ W m}^{-2}$ . With the  $d\text{-Ti}_3\text{C}_2\text{T}_x/\text{GO-45}$  membrane, this goal can be achieved at a fairly low applied hydraulic pressure difference, indicating an apparent saving in pumping energy and a more obtainable net PRO power output.

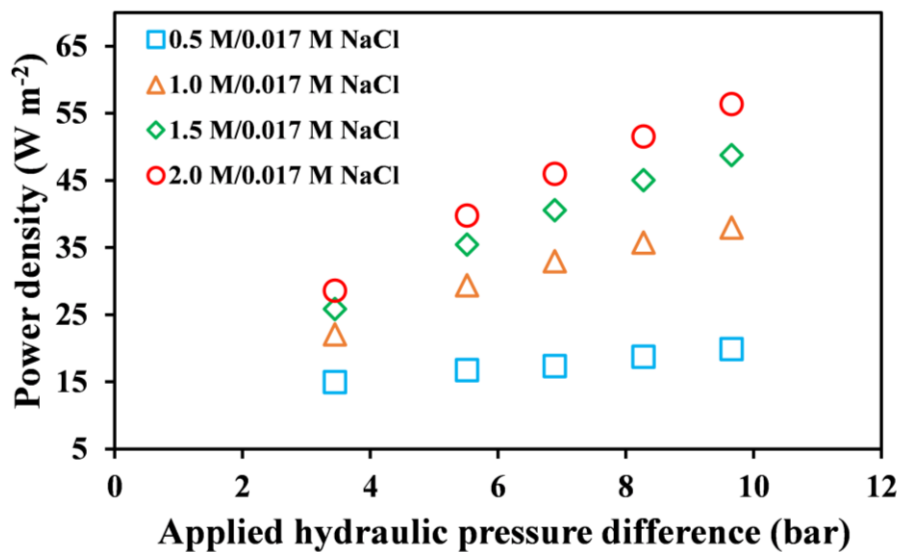


Figure 26 - The projected power density of the  $d\text{-Ti}_3\text{C}_2\text{T}_x/\text{GO-45}$  membrane as a function of the applied hydraulic pressure difference in a PRO system. Different concentrations of NaCl solution worked as draw solution and river water (0.0017 M NaCl) as feed solution.

#### 5.4.4. Antifouling potential of the membranes

The antifouling potential of the  $d\text{-Ti}_3\text{C}_2\text{T}_x/\text{GO}$  hybrid membrane in terms of the natural organic matter (NOM) was investigated by the HA filtration in the revised RO cell. The fouling behaviors of the membranes are displayed in Figure 27a. As shown in Stage II, with the feed solution shifting from pure water to HA solution, all the investigated membranes suffered an apparent decrease in permeate flux. The FDR of the  $d\text{-Ti}_3\text{C}_2\text{T}_x/\text{GO-}$

25,  $d\text{-Ti}_3\text{C}_2\text{T}_x/\text{GO}$ -45, and the commercial cellulose triacetate (CTA) membranes were determined to be 13.5%, 22.1% and 5.0%, respectively. The results indicate an improved HA fouling resistance of the membrane with incorporation of more GO contents in the hybrid membranes. After the membranes were cleaned thoroughly, the FRR values of the  $d\text{-Ti}_3\text{C}_2\text{T}_x/\text{GO}$ -25,  $d\text{-Ti}_3\text{C}_2\text{T}_x/\text{GO}$ -45, and the commercial CTA membranes were 69.3%, 86.3%, and 74.5%, respectively. The larger FRR value of the  $d\text{-Ti}_3\text{C}_2\text{T}_x/\text{GO}$ -45 membrane indicates a greater cleaning efficiency. The higher FDR and FRR results indicate that the  $d\text{-Ti}_3\text{C}_2\text{T}_x/\text{GO}$  membrane with higher GO content outperformed both the hybrid membrane holding a lower GO content and the commercial membrane.

The enhanced hydrophilicity and negative surface charge were primarily responsible for the improved antifouling potential of the  $d\text{-Ti}_3\text{C}_2\text{T}_x/\text{GO}$  -45 membrane. The addition of hydrophilic GO gave rise to a more hydrophilic membrane surface, which strengthened the binding capacity for water molecules on that surface enabling the formation of a hydrated layer to better resist hydrophobic organic foulants [158]. Moreover, the increased surface negative charge introduced by the incorporation of GO contributed to the electrostatic repulsion between the negatively charged HA and the membrane surface resulting in a reduced adhesion of HA on the membrane surface [159]. Additionally, a larger surface roughness had a negative effect on the membrane antifouling property. As shown in Figure 39, the membrane surface roughness became smoother with increased GO content in the hybrid membranes. Thus, the reduced membrane surface roughness of the  $d\text{-Ti}_3\text{C}_2\text{T}_x/\text{GO}$  - 45 positively contributed to the enhanced antifouling control.

The membrane antimicrobial property was evaluated against the adhesive interactions of *E. coli* with the membrane surface using a CFU enumeration assay. Figure 27b shows the abundance of attached *E. coli* cells on the *d*-Ti<sub>3</sub>C<sub>2</sub>T<sub>x</sub>/GO-45 membrane surface was reduced by 59.4% in comparison with the pure *d*-Ti<sub>3</sub>C<sub>2</sub>T<sub>x</sub> membrane after a 5-h exposure. While, for the *d*-Ti<sub>3</sub>C<sub>2</sub>T<sub>x</sub>/GO-25 membrane, there was only a 21.2 % attachment reduction compared with the pristine *d*-Ti<sub>3</sub>C<sub>2</sub>T<sub>x</sub> membrane. Both MXene and GO have been shown to hold high antibacterial activity due to the physical damage and chemical oxidation to *E. coli* [160-162]. However, the bacterial colonization formed with the detached *E. coli* from the pristine GO membrane is much less than the CFU formed with that from pristine MXene membrane. Thus, in terms of membranes, the adhesive interaction between the *E. coli* and the membrane surface relationship to the membrane surface properties is a potential explanation for the CFU abundance difference [163]. The improved surface hydrophilicity and smoother surface roughness arising from the increased GO loading enabled the *d*-Ti<sub>3</sub>C<sub>2</sub>T<sub>x</sub>/GO-45 membrane to become less prone to the fouling induced by hydrophobic *E. coli* cells. The enhanced antibacterial performance of membrane with a higher GO contents could increase the membrane biofouling potential by restricting bacterial attachment and biofilm formation on the membrane surface.

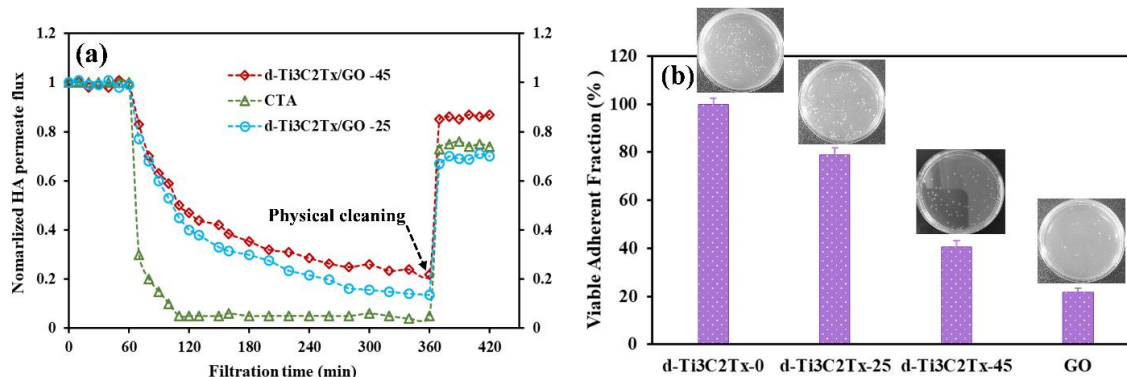


**Figure 27 - The antifouling potential of the membrane against (a) the NOM (HA) and (b) the bacterium (*E. coli*). Stage I: The membrane under investigation was first compacted with DI water at 3.45 bar for 2 h to reach a steady water flux. Stage II: The feed solution was switched to an HA solution of 30 ppm, and the filtration was conducted for another 5 h under the same hydraulic pressure difference. Stage III: The fouled membrane was physically cleaned, and the pure DI water filtration was then performed for 1h.**

## 5.5. Conclusions

We have demonstrated that the freestanding MXene/GO lamellar membrane is an attractive candidate to capture osmotic power as a form of sustainable energy through a PRO system. Benefiting from the combination of MXene and GO, the hybrid membrane

exhibited enhanced mechanical strength and water stability, which allowed the membrane to withstand a relatively high burst pressure of up to 9.66 bar. The support-free membrane with the elimination of ICP gave the composite membrane an elevated water permeability and record-high power density of  $56.4 \text{ W m}^{-2}$  with 2.0 M NaCl and 0.017 M NaCl as the draw solution and feed solution, respectively. Additionally, the enhanced surface hydrophilicity and negative surface charge is favorable to membrane fouling control in terms of both NOM and bacteria. Our findings advanced the prospect of further development of 2D materials-based lamellar membranes to facilitate osmotically driven membrane processes such as osmotic energy harvesting, but they are not limited to this application.

## CHAPTER 6. MAJOR CONCLUSIONS AND FUTURE WORK

### 6.1. Major Conclusions

The key conclusions throughout the dissertation are as following:

- The intricate relationship of the permselectivity and ionic resistance (referred to membrane conductance in this work) of IEMs with its underlying characteristics was explored. With the help of the statistical modelling of membrane microstructure by employing the membrane three-phase model coupled with the percolation theory, the dependency of permselectivity and membrane conductivity changes on membrane thickness and water content has been successfully simulated and validated with experimental data from a set of SPPO membranes and commercial FKS membranes. The modeling and simulation results from this work enable the fine-tuning approaches for the fabrication of IEMs with desired properties for high performance output in a IEMs-based electrochemical system.
- Monovalent-ions selective AEMs with enhanced antifouling potential were fabricated with the LBL modification of standard AEMs. By alternatively introducing negatively charged polyelectrolytes and positively charged polyelectrolytes, a pretty thin film with negative charge as well as improved hydrophilicity was form at the surface of standard AEMs. The enhancements on these surface properties render membrane monovalent-ion selectivity as well as membrane antifouling potential. The monovalent-ions selectivity is primarily attributed to the much smaller Donnan exclusive force between the monovalent ions with the surface charge than that between multivalent ions with the surface charge.

Due to the enhanced electrostatic repulsion and hydrophobic interaction of organic foulants with the optimized surface, the membranes showed increased anti-fouling potential. Benefiting from the simultaneous enhancement on monovalent-ion selectivity and anti-fouling potential, the power density achieved in a RED system with the presence of multivalent ions and foulants containing in the feed streams was apparently elevated. Based on the results in this work, the monovalent-ions selective membranes obtained from LBL optimization was suggested to be favorable to practical application viability of chemical potential driven membrane technologies like RED.

- The freestanding of MXene/GO composite membranes were fabricated and employed in the PRO system for osmotic power harvesting. By combining the 2D materials, MXene and GO, the hybrid membranes hold largely enhanced mechanical strength in comparison to the pristine MXene membrane and improved water stability compared to pure GO membrane. The freestanding thin membranes exhibited satisfactory water permeability and record-high output power density due to the mitigation of the ICP during PRO process. The facile fabrication of MXene/GO lamellar membrane, couple with its versatile chemical tunability and scale-up viability, sheds light on a new membrane development platform for high-performance osmotic power harvesting technologies. In addition, the findings on the simultaneously improved antifouling potential and antibacterial activity further advance the practical application feasibility of the 2D materials-based composite membranes.

## 6.2. Future Work

Based on the findings from this dissertation, future works on further advancing of membrane -based technologies to harvest clean and renewable energy may include:

- Designing new types of monovalent-ions selective membranes for more efficient SGP harvesting in RED system. In our work, we have demonstrated that LBL modification of standard IEMs with polyelectrolytes is a promising approach to develop monovalent-ions selective membranes with enhanced antifouling potential. However, the introduction of the thin layer on standard membrane surface by LBL assembly of polyelectrolytes potentially increase the membrane ionic resistance, which is not favorable for RED power output since membrane area resistance plays a critical role on better RED power output. Thus, it is critically essential to develop IEMs with monovalent-ions selectivity with no increase in membrane area resistance. The zwitterionic groups have been acknowledged to hold potential in ions selectivity. To synthesize IEMs with zwitterionic functional groups at membrane surface or through the membrane matrix might be a promising candidate for high-performance monovalent-ions selective membranes.
- Recently, the combination of different 2D materials to overcome the limitation of individual 2D materials have attracted increasing interests in various fields. In our work, we highlight the promise in the scale-up application of MXene/GO hybrid membranes for osmotic power harvesting through PRO technology. A better understanding on the interactions between two different 2D materials based on modelling or first-principle calculation will provide pathways to tune the membrane fabrication. In terms of the application in osmotically driven membrane process for

SGP generation, to achieve the maximal power density, it is necessary to develop freestanding membranes with further enhanced mechanical strength and water stability to withstand the burst pressure no less than half of the osmotic pressure difference for a given pair of draw and feed solution.

## APPENDIX A. SUPPORTING INFORMATION FOR CHAPTER 3

### A.1 Detailed description of membrane characterization

#### A.1.1 Permselectivity and ionic resistance

Membrane permselectivity is the ability of an IEM to selectively allow cation permeation while repulsing anions. The apparent permselectivity ( $\alpha$ ) of the series SPPO membranes was determined via a static potential measurement method. In detail, a two-compartment cell was filled with 500 mL of 0.5 M NaCl and 0.1 M NaCl, respectively. The membrane under investigation was placed in between to separate the two solutions. The effective testing area of the membrane is 4.8 cm<sup>2</sup>. Two Ag/AgCl reference electrodes (Hanna Instruments, USA) were utilized to measure the potential difference across the membrane, and the potential was recorded with a Tektronix DMM4050 multimeter (Tektronix, Beaverton, OR, USA). The apparent permselectivity was calculated by the ratio of the measured membrane potential ( $\Delta V_{\text{measured}}$ ) over the theoretical potential of 0.5 M NaCl over 0.1 M NaCl ( $\Delta V_{\text{theoretical}} = 37.91$  mV), as follows:

$$\alpha(\%) = \frac{\Delta V_{\text{measured}}}{\Delta V_{\text{theoretical}}} \times 100\% \quad (35)$$

where  $\alpha$  is the apparent permselectivity (%), and  $\Delta V_{\text{measured}}$  and  $\Delta V_{\text{theoretical}}$  are the measured and theoretical membrane potentials, respectively.

The ionic resistance was measured via the electrochemical impedance spectroscopy (EIS) method in a custom-built four-compartment module. The effective testing area for all the investigated membranes was 7.91 cm<sup>2</sup>. The two outer compartments were supplied with 0.3 M Na<sub>2</sub>SO<sub>4</sub> and the solutions were circulated through a Masterflex L/S peristaltic

pump (Cole-Parmer Instrument Company, Chicago, IL, USA). The working solution of 0.5 M NaCl was pumped into the two inner compartments separated by the membrane under investigation and circulated through another Masterflex L/S peristaltic pump (Cole-Parmer Instrument Company, USA). The working solutions and the electrode solutions were separated by two commercial Fumasep anion exchange membranes (AEMs) ((FuMA-Tech GmbH, Bietigheim-Bissingen, Germany). Two titanium electrodes coated with platinum were applied as the working and counter electrodes, which were connected to a Vertex potentiostat (Ivium Technologies, Eindhoven, The Netherlands). Two Ag/AgCl reference electrodes were placed in two custom-made Luggin-Haber capillaries and were employed to monitor the impedance across the membrane. The obtained membrane ionic resistance was corrected by subtracting the blank resistance measured without membranes in between.

#### *A.1.2 Ion exchange capacity (IEC)*

IEC represents the number of functional groups per unit weight of the dried membrane, which can be determined through acid-base titration. In detail, the investigated membrane sample was first immersed in HCl solution of 1.0 M for 24 h. After rinsing with D.I. water, the membrane sample was then immersed into NaCl solution of 0.5 M for another 24 h to completely fulfill the ion exchange (i.e., the replacement of  $H^+$  by  $Na^+$ ). Subsequently, the resultant NaCl solutions containing exchanged protons were titrated with 0.01 M NaOH with phenolphthalein as an indicator. The IEC of the membrane can be calculated as follows:

$$IEC = \frac{C_{NaOH} \times V_{NaOH}}{W_{dry}} \quad (36)$$

where  $C_{NaOH}$  is the concentration of NaOH used, and  $V_{NaOH}$  is the volume of NaOH consumed.

## A.2 The properties for all the membrane.

**Table 8 - The properties for all the membranes.**

<b>Solvent</b>	<b>Membrane thickness (μm)</b>	<b>Apparent permselectivity (%)</b>	<b>Void ratio (%)</b>	<b>Membrane conductance (S cm<sup>-2</sup>)</b>	<b>Simulated percolated Volume ratio</b>	<b>Simulated non-percolated volume ratio</b>
<b>NMP</b>	2.5	55.2	87.4	-	0.873	0.127
	3.3	60.2	81.9	-	0.818	0.182
	8.7	81.0	42.6	7.23	0.757	0.643
	13.2	90.4	46.6	11.3	0.412	0.588
	14.0	90.2	40.4	-	0.315	0.685
	14.1	85.2	53.4	6.69	0.521	0.479
	29.5	92.5	40.0	3.22	0.313	0.687
	33.0	93.3	43.4	2.22	0.375	0.625
	48.7	94.5	42.6	1.61	0.358	0.642
<b>DMF</b>	3.5	67.6	84.0	13.6	0.830	0.170
	7.2	76.1	77.0	-	0.760	0.240
	20.2	94.5	39.6	5.29	0.331	0.669
	20.3	92.6	54.6	4.59	0.540	0.460
	27.4	95.3	45.7	-	0.409	0.591
	39.8	95.4	41.3	2.39	0.329	0.671
	49.5	97.4	42.5	2.32	0.348	0.652
<b>FKS</b>	9.8	98.3	0.30	1.84	0.00	1.00
	13.7	98.6	0.27	1.54	0.00	1.00
	30.2	98.7	0.25	0.93	0.00	1.00
	52.7	99.0	0.22	0.66	0.00	1.00

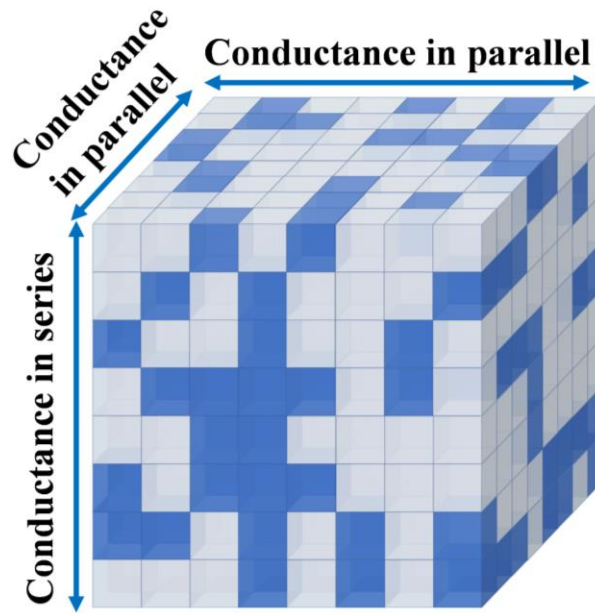


**Figure 28 - The scheme for membrane conductance distribution on a 3D lattice.**

### **A.3 Java codes for the Monte Carlo simulation**

An implementation of percolation theory simulation is provided in Java code. Additional functions are implemented to obtain numbers of site of different interest, which are well commented.

```

import java.io.*;
import java.util.Random;

public class Percolation3D {
    private final UnionFind matrix, full, fullBottom; // must be UnionFind data
    structure
    private final boolean [] opened; // record whether a site is open or not
    private final int nCol, nRow, nDep, size;
    private int openCount = 0;

    public Percolation3D(int row, int col, int dep) {
        // create row-by-col-by-dep grid, with all sites blocked
        nCol = col;
        nRow = row;
        nDep = dep;
        size = nCol * nRow * nDep;
        opened = new boolean[size];
        for (int i = 0; i < size; i++) {
            opened[i] = false;
        }
        matrix = new UnionFind(size+2);
        full = new UnionFind(size+1);
        fullBottom = new UnionFind(size+1);
    }

    public Percolation3D(int n) {
        // create n-by-n-by-n grid, with all sites blocked
        checkIndices(n);
        nCol = n;
        nRow = n;
        nDep = n;
        size = n * n * n;
        opened = new boolean[size];
        for (int i = 0; i < size; i++) {
            opened[i] = false;
        }
        matrix = new UnionFind(size+2);
        full = new UnionFind(size+1);
        fullBottom = new UnionFind(size+1);
    }

    private void printMatrix() {
        // visualization of matrix for debugging; only intuitive on 2-D
        for (int i = 0; i < size; i++) {
            if (opened[i]) {
                System.out.print(" o ");
            } else {
                System.out.print(" * ");
            }
            if ((i + 1) % nCol == 0) {
                System.out.println();
            }
        }
    }

    private void checkIndices(int row, int col, int dep) {
        if (row <= 0 || row > nRow) throw new IllegalArgumentException("row index i
out of bounds");
        if (col <= 0 || col > nCol) throw new IllegalArgumentException("column index i
out of bounds");
        if (dep <= 0 || dep > nDep) throw new IllegalArgumentException("depth index i
out of bounds");
    }
}

```

```

public int numberOfPercolatedSites() {
    // returns number of sites that are part of percolated pathway
    if (percolates()) {
        int fullOrPercolate = Math.max(matrix.numberInUnion(0),
matrix.numberInUnion(size+1)) - 2;
        int bottomDeadEnd = fullOrPercolate - numberOfTopFullSites();
        int topDeadEnd = fullOrPercolate - numberOfBottomFullSites();
        return fullOrPercolate - topDeadEnd - bottomDeadEnd;
    }
    else {return 0;}
}

protected int numberOfInertSites() {
    // returns number of sites that are not part of percolated pathway
    if (percolates()) {
        return openCount - Math.max(matrix.numberInUnion(0),
matrix.numberInUnion(size+1)) + 2;
    } else return openCount - matrix.numberInUnion(0) - matrix.numberInUnion(size
+ 1) + 2;
}

int numberOfOpenSites() {
    // number of open sites
    return openCount;
}

boolean percolates() {
    return matrix.connected(0, size+1);
}

// used for calculation of different types of sites
public int numberOfTopFullSites() { return full.numberInUnion(0) - 1; }
// used for calculation of different types of sites
public int numberOfBottomFullSites() { return fullBottom.numberInUnion(0) - 1; }

public int getSize() {
    return size;
}

public void outputPercolation(String filename) {
    // output site array mark only sites belongs to percolation pathways
    try {
        File file = new File(filename);
        PrintWriter pw = new PrintWriter(file);
        pw.print(nCol);
        pw.print(",");
        pw.print(nRow);
        pw.print(",");
        pw.print(nDep);
        pw.print(",");
        for (int i=1; i<= size; i++) {
            if (full.connected(0, i) && fullBottom.connected(0, i)) {
                pw.print(1);
                pw.print(",");
            } else {
                pw.print(0);
                pw.print(",");
            }
        }
        pw.close();
    } catch (FileNotFoundException ex) {

```

```

        System.out.print(ex.fillInStackTrace());
    }
}

public int checkOpenType(int position) {
    // checks whether an open site is surrounded by all open sites (void) or not
    int[] pos = indexToPosition(position);
    int row = pos[0]; int col = pos[1]; int dep = pos[2];
    int openNeighbors = 0;
    // count the number of legal neighbor open sites
    if (opened[indexing(row + 1, col, dep) - 1]) { openNeighbors++;}
    if (opened[indexing(row, col + 1, dep) - 1]) { openNeighbors++;}
    if (opened[indexing(row - 1, col, dep) - 1]) { openNeighbors++;}
    if (opened[indexing(row, col - 1, dep) - 1]) { openNeighbors++;}
    if (isLegalSite(row, col, dep - 1)) {if (isOpen(row, col, dep - 1))
{ openNeighbors++;}}
    if (isLegalSite(row, col, dep + 1)) {if (isOpen(row, col, dep + 1))
{ openNeighbors++;}}

    return openNeighbors;
}

public int[] indexToPosition(int ind){
    // utility function to translate index to 3-D coordinates
    int[] position = new int[3];
    position[2] = (ind - 1) / (nRow*nCol) + 1; // depth
    int remainder = (ind - 1) % (nRow*nCol);
    position[0] = remainder / nCol + 1; // row
    position[1] = remainder % nCol + 1; // column

    return position;
}

public int getVoidSites(int voidNeighborNumber) {
    int countVoid = 0;
    // loop through all sites to find open sites with more than
@voidNeighborNumber of open neighbors
    for (int i=1; i<= size; i++){
        if (full.connected(0, i) && fullBottom.connected(0, i)) {
            if(checkOpenType(i)>=voidNeighborNumber) countVoid++;
        }
    }

    return countVoid;
}

public int numberOfSurfacePercolatedSites() {
    int count = 0;
    // loop through all "surface" sites to find open sites belongs to percolation
pathways
    for (int i=1; i<= nRow*nCol; i++){
        if (full.connected(0, i) && fullBottom.connected(0, i)) {
            count ++;
        }
    }

    for (int i=(nDep-1)*nCol*nRow+1; i<=size; i++) {
        if (full.connected(0, i) && fullBottom.connected(0, i)) {
            count ++;
        }
    }
}

```

```

    return count / 2; // average surface area that belongs to percolated sites
}

public double normalConductivity(int membraneKappa, int solutionKappa) {
    // explicit calculation of conductivity along the dep dimension
    double conduc = 0, conducTemp = 0;
    for (int i = 1; i <= nRow * nCol; i++) {
        for (int d = 1; d <= nDep; d++) {
            int ind = (d - 1) * nRow * nCol + i;
            if (opened[ind - 1]) {
                conducTemp += (double) 1 / solutionKappa;
            } else {
                conducTemp += (double) 1 / membraneKappa;
            }
        }
        conduc += 1 / conducTemp;
    }

    return conduc;
}

public static void main(String[] args) {
    // test client (showing an exemplary usage
    int nRow = 32, nCol = 32, nDep = 5000;
    Percolation3D p = new Percolation3D(nRow, nCol, nDep);
    double freeRatio = 0.40;

    Random rand = new Random();
    // while (!p.percolates()) {
    //     int row = rand.nextInt(nRow) + 1;
    //     int col = rand.nextInt(nCol) + 1;
    //     int dep = rand.nextInt(nDep) + 1;
    //     p.open(row, col, dep);
    // }
    while (p.openCount < p.size * freeRatio) {
        // int row = rand.nextInt(nRow) + 1;
        // int col = rand.nextInt(nCol) + 1;
        // int dep = rand.nextInt(nDep) + 1;
        p.open(row, col, dep);
    }

    System.out.println((float)p.numberOfSurfacePercolatedSites() / (nRow*nCol));
    System.out.println(p.openCount);
    System.out.println((float)p.openCount/p.size);
    System.out.println(p.percolates());

    // p.printMatrix();
}

public class UnionFind {
    private int[] root; // root
    private int[] size; // number of children rooted
    // private int count; // number of components

    /**
     * Initializes an empty union-find data structure with {@code n} sites
     * {@code 0} through {@code n-1}. Each site is initially in its own

```

```

    * component.
    *
    * @param n the number of sites
    * @throws IllegalArgumentException if {@code n < 0}
    */
    public UnionFind(int n) {
        // count = n;
        root = new int[n];
        size = new int[n];
        for (int i = 0; i < n; i++) {
            root[i] = i;
            size[i] = 1;
        }
    }

    public int findRoot(int i) {
        validate(i);
        while(i != root[i]) {
            root[i] = root[root[i]];
            i = root[i];
        }
        return i;
    }

    // validate that p is a valid index
    private void validate(int p) {
        int n = root.length;
        if (p < 0 || p >= n) {
            throw new IllegalArgumentException("index " + p + " is not between 0 and "
+ (n-1));
        }
    }

    /**
     * Returns number of inter isolated unions
     * @return
     */
    // public int count() { return count; }

    /**
     * Returns true if two sites are in union
     * @return
     */
    public boolean connected(int p, int q) { return findRoot(p) == findRoot(q); }

    public void union(int p, int q){
        int i = findRoot(p);
        int j = findRoot(q);
        if (i == j) return;
        if (size[i] < size[j]) {root[i] = j; size[j] += size[i]; }
        else {root[j] = i; size[i] += size[j]; }
    // count--;
    }

    /**
     * Returns the number of unioned sites for special applications
     * @return
     */
    public int numberInUnion(int element){
        return size[findRoot(element)];
    }
}

```



## B.2 Surface zeta potential, membrane area resistance and permselectivity

Before treating the membranes with PSS and PEI solutions, the zeta potential of PSS and PEI solutions were firstly determined using zetasizer nano ZS (ZEN 3600, Malvern Instruments). The PSS and PEI solutions were prepared by dissolving PSS and PEI into 1.0 M NaCl solution (working as the supporting electrolyte to make its concentration of 1.0 g/L. The pH values of PSS and PEI solutions was adjusted by 1.0 M NaOH and 1.0 M HCl, respectively. As shown in Figure 30, the relatively high zeta potential for PSS and PEI solutions could be obtained at pH around 5.0.

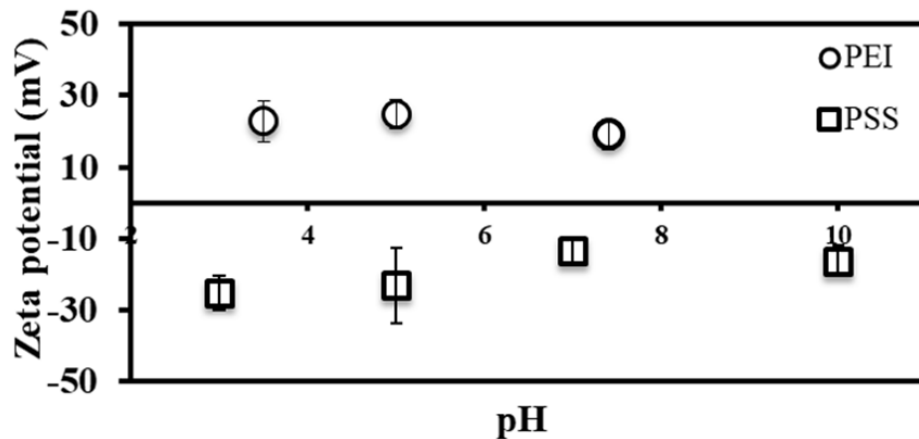


Figure 30 - Zeta potential of 1 g/L of PSS and 1 g/L of PEI as a function of pH.

Field emission scanning electron microscopy (FE-SEM, Hitachi SU8230, Hitachi High Technologies, Corp., Japan) was used to determine membrane cross-sections. The membranes were vacuum-dried before performing the SEM test. Sharp cross-sections were obtained by soaking dried membranes into liquid nitrogen.

X-ray photoelectron spectroscopy (XPS, Thermo K-Alpha) was performed to detect elements (C, O, N, S) on the membrane surface. The surface sensitivity of XPS goes up to 5 nm. The membranes were dried in an oven under vacuum overnight.

Atomic force microscopy (AFM, Agilent 5500, Agilent Technologies, Inc., USA) was utilized to characterize the surface topography. The average surface roughness was obtained. At least five random positions were measured for each membrane sample.

Zetasizer along with surface zeta potential electrode (Malvern Zetasizer Nano ZS, Malvern Instruments Ltd., UK) was used to determine the surface zeta potential of membrane samples based on the particle electrophoresis. The silica particle standards (ThermoFisher Scientific) were dispersed in DI water to work as tracers. The membranes were rinsed thoroughly with DI water several times before measurements, and then dried at room temperature. At least three samples were measured for each membrane.

Ramé-hart standard contact angle Goniometer (Model 250, Ramé-hart Instrument Co., USA) was used to perform water contact angle measurements. The hydrophilic properties of the membranes were evaluated based on water contact angle. Before testing, the membranes were thoroughly rinsed with DI water and then dried in a vacuum oven. The static water contact angle was obtained by placing 4  $\mu$ L of DI water droplets onto the vacuum-dried membrane surface. The measurements were carried out at least three locations for each membrane sample.

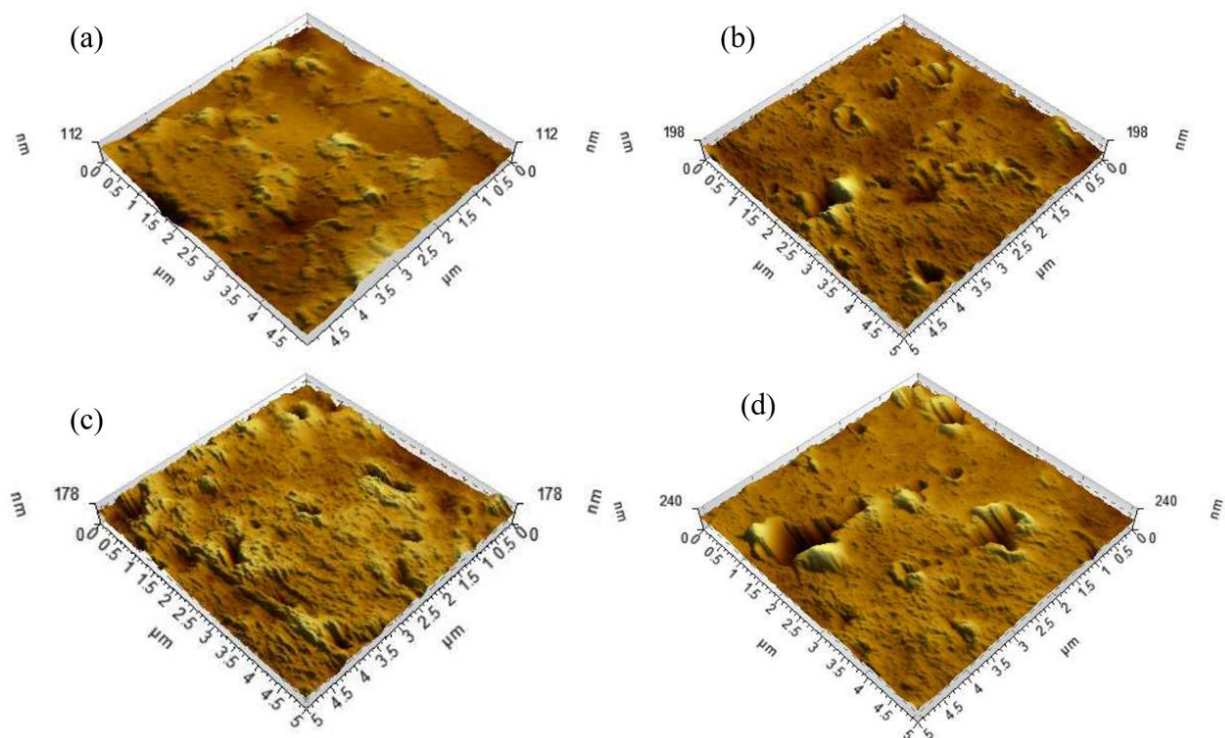
The membrane area resistance was measured by the custom-built four-cell module as shown in Figure 11. Electrochemical impedance spectroscopy (EIS) technique was used to characterize the membrane resistance based on the literature [164]. The effective area for all the membranes was 7.91 cm<sup>2</sup>. The compartments 2 and 3 were supplied with 0.5 M NaCl circulating through both compartments at a flow rate of 100 mL/min by a Masterflex L/S peristaltic pump (Cole-Parmer Instrument Company, USA). The electrode solution of 0.5 M Na<sub>2</sub>SO<sub>4</sub> was pumped into compartments 1 and 4 and was circulated through both compartments under a flow rate of 100 mL/min by a Masterflex L/S peristaltic pump (Cole-Parmer Instrument Company, USA). Two titanium electrodes coated with platinum were used as working and counter electrodes connected to a Vertex potentiostat (Ivium Technologies, The Netherlands). The Ag/AgCl electrodes placed in two custom-made Luggin-Haber capillaries were used as reference electrodes to monitor the impedance over the membranes. The membrane area resistance was corrected by subtracted the solution resistance measured without membranes.

The apparent permselectivity ( $\alpha$ ) of the membranes were determined by the ratio of measured membrane potential over the theoretical one (listed in Table 9). The membrane potential was measured using a static potential measurement reported in previous work [114]. The membrane was placed between two cells. 500 mL of 0.5 M and 0.1 M NaCl solutions were filled into the two cells. The solutions were vigorously stirred via stir bars to minimize concentration polarization. The Ag-AgCl electrodes were used to measure the potential difference over the membrane, and was recorded by a multimeter (Tektronix, USA). Based on the Nernst equation, the theoretical potential in this case is calculated to be 37.91 mV.

**Table 9 - Membrane hydrated thicknesses and permselectivity.**

<b>Membranes</b>	<b>Thickness (<math>\mu\text{m}</math>)</b>	<b>Permselectivity (<math>\alpha</math>, %)</b>
CJMA-2	89.0	91.17
CJMA-2-2.5	90.0	91.62
CJMA-2-3.5	91.5	91.45
CJMA-2-4.5	94.3	91.33
CJMA-2-5.5	97.4	91.17
CJMA-2-7.5	102.7	91.05
CJMA-2-10.5	108	90.68
ACS	119	93.16

### B.3 AFM topography images of the membranes



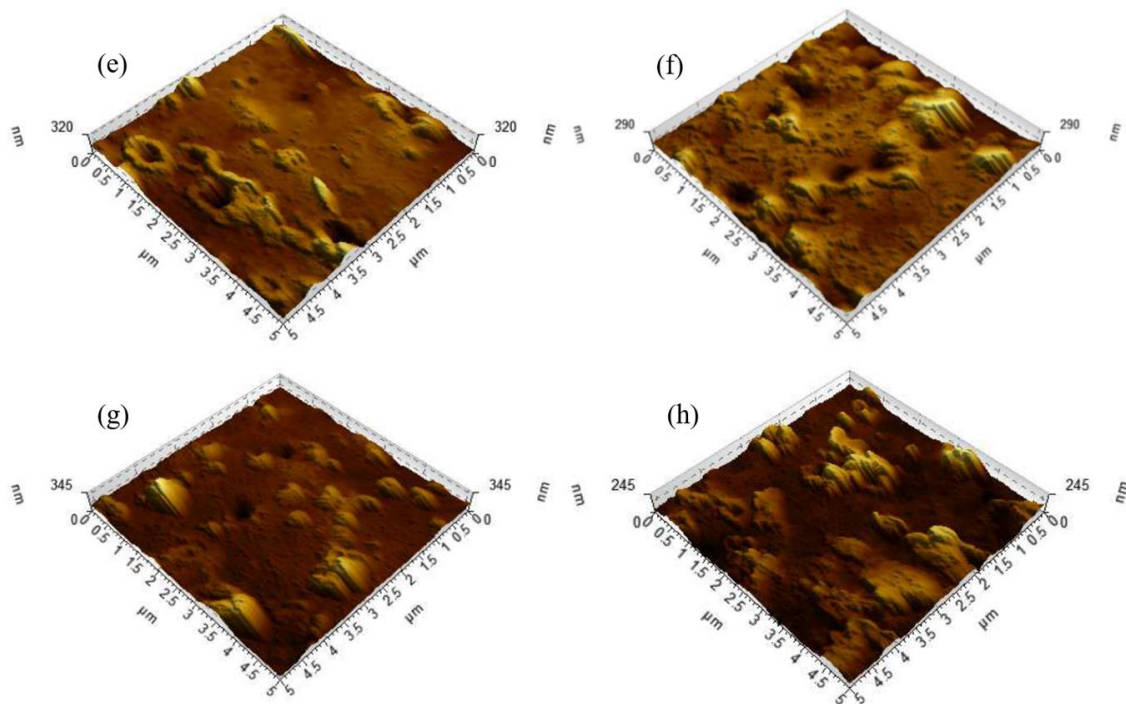


**Figure 31 - AFM images of membrane surface: (a) ACS membrane, (b) pristine CJMA-2 membrane, (c) CJMA-2-2.5 membrane, (d) CJMA-2-3.5 membrane, (e) CJMA-2-4.5 membrane, (f) CJMA-2-5.5 membrane, (g) CJMA-2-7.5 membrane, and (h) CJMA-2-10.5 membrane.**

#### B.4 Current-voltage (*I-V*) curves and the limiting current density

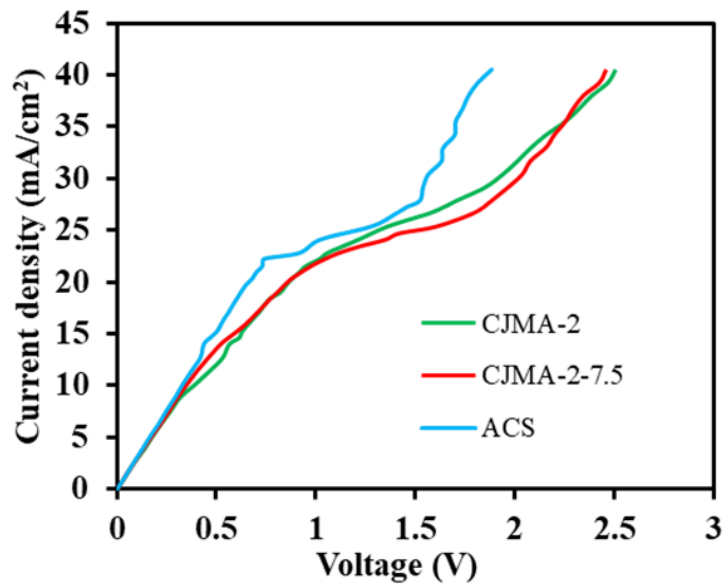


Figure 32 - Current-voltage (*I-V*) curves obtained with mixtures of 0.05 M NaCl and 0.05 M Na<sub>2</sub>SO<sub>4</sub>.

## B.5 Transport numbers and measured OCV in a RED system

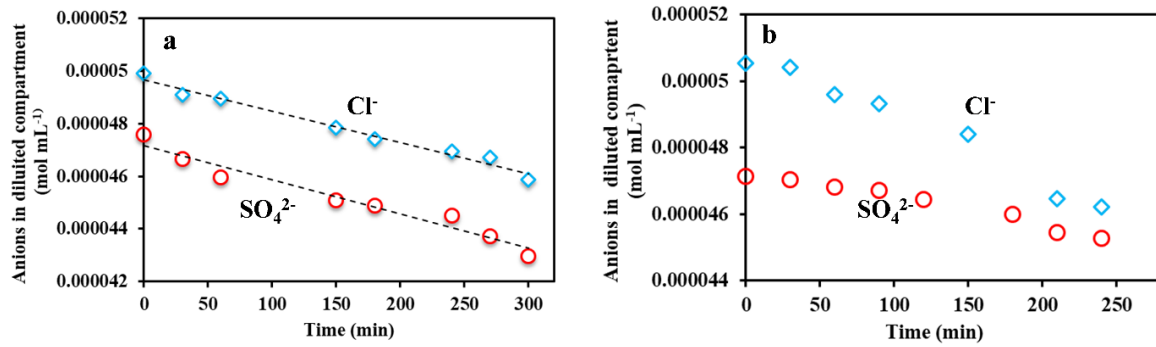
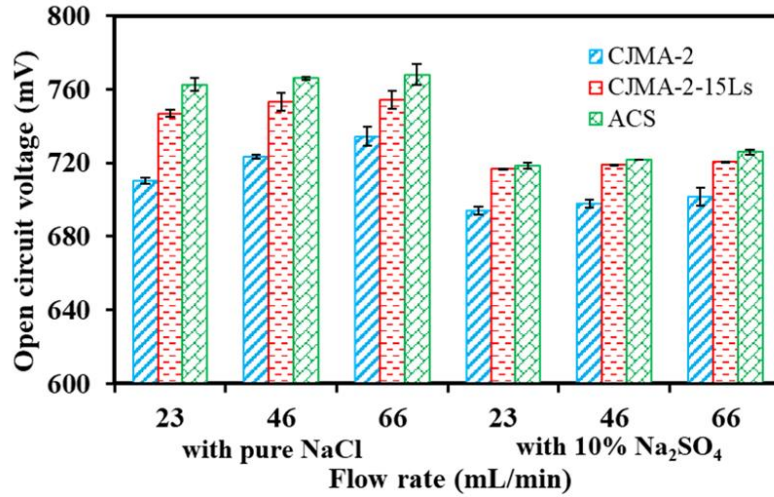


Figure 33 - Time-dependent amounts of Cl<sup>-</sup> and SO<sub>4</sub><sup>2-</sup> in the diluted compartment, for (a) pristine CJMA-2 membrane, and (b) CJMA-2-7.5 membrane.



**Figure 34 - Open circuit voltage with pure NaCl (0.5 M) and with NaCl containing 10 % of Na<sub>2</sub>SO<sub>4</sub> (total concentration of 0.5 M) as feed solutions, respectively, under different flow velocities.**

## **B.6 Energy conversion efficiency**

The energy conversion efficiency is defined by the fraction of the harvestable energy to the Gibbs free energy released by mixing of solutions containing NaCl and Na<sub>2</sub>SO<sub>4</sub> as follows [123]:

$$\eta = \frac{EI}{RT \left( \ln \frac{a_{i,c}}{a_{i,d}} \right) (J_{Cl^-} + J_{SO_4^{2-}})} \quad (37)$$

Where, E and I are the electric potential generated in a RED system and the current carried by the anions in the system. In a system with feedwaters containing NaCl and Na<sub>2</sub>SO<sub>4</sub>, the current *I* can be expressed as follows:

$$I = z_i F (J_{Cl^-} - J_{SO_4^{2-}}) \quad (38)$$

In a RED system with feedwaters containing mixture of NaCl and Na<sub>2</sub>SO<sub>4</sub>, the membrane potential difference  $E_{OCV}$  can be defined as follows [165, 166]:

$$E_{OCV} = (t_{SO_4^{2-}} - t_{Cl^-}) \frac{RT}{z_i F} \left( \ln \frac{a_{i,c}}{a_{i,d}} \right) \quad (39)$$

In this work, the assumption was made that the co-ions effect is negligible. Thus, the following relationship could be obtained:

$$t_{Cl^-} + t_{SO_4^{2-}} = 1 \quad (40)$$

It has been proven that the maximum energy conversion efficiency corresponding to the maximum power generation can be achieved when *E* is equal to half of the  $E_{OCV}$  [167]. Then, by combining Equations 38 - 40 and Equation 25, the energy conversion efficiency can be derived as Equation 37.

## APPENDIX C. SUPPORTING INFORMATION FOR CHAPTER 5

### C.1 The membrane fabrication procedure and testing cell.

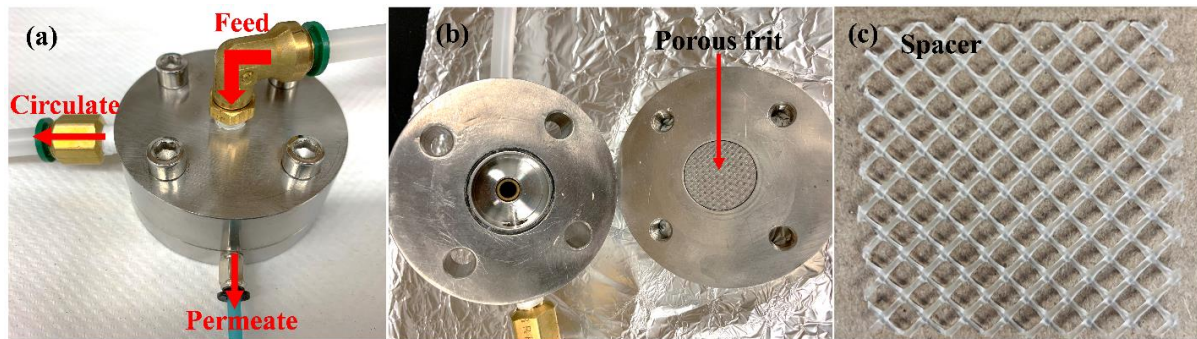


Figure 35 - The revised RO cell used to determine the membrane water and salt permeability coefficients.

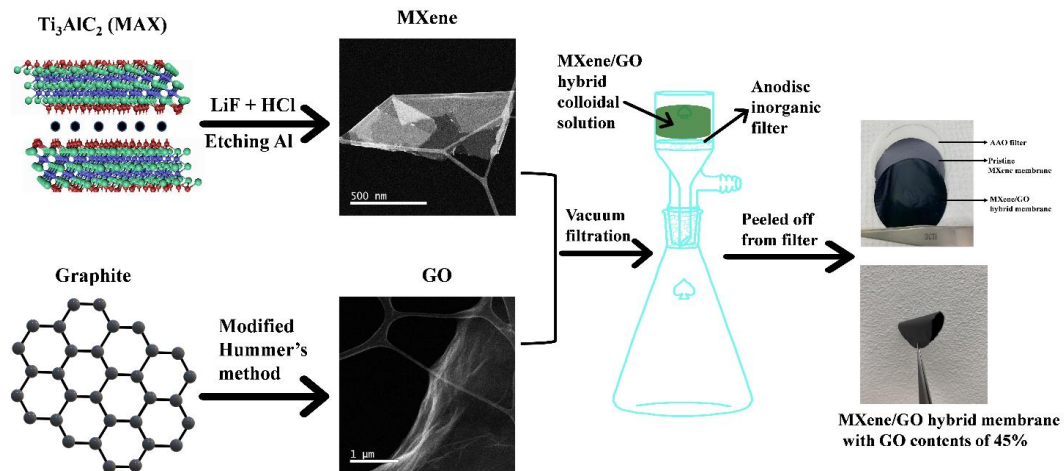


Figure 36 - The fabrication procedure of the MXene/GO hybrid membranes.

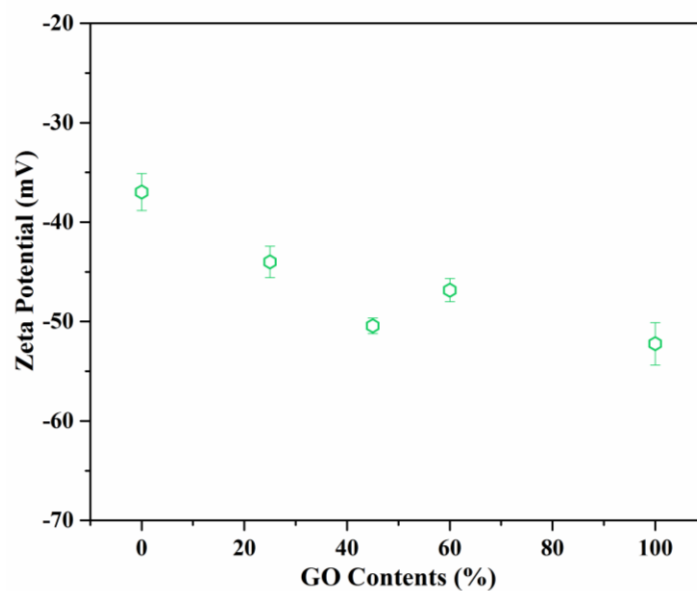


Figure 37 - zeta potential of MXene/GO colloidal solutions as a function of GO contents.

## C.2 The membrane properties and the maximum power density.

**Table 10 - The mechanical properties of the membranes.**

<b>Membrane</b>	<b>Tensile strength (Mpa)</b>	<b>Young's Modulus (Gpa)</b>	<b>Strain to failure (%)</b>
<i>d</i> -Ti <sub>3</sub> C <sub>2</sub> T <sub>x</sub> -0	19.3±1.5	3.47±0.1	1.2 ± 0.2
<i>d</i> -Ti <sub>3</sub> C <sub>2</sub> T <sub>x</sub> -25	33.1 ± 2.0	2.58 ± 0.3	2.0 ± 0.3
<i>d</i> -Ti <sub>3</sub> C <sub>2</sub> T <sub>x</sub> -45	94.0 ± 4.2	4.1 ± 0.5	9.1 ± 0.1

**Table 11 - The intrinsic characteristics of the membranes.**

<b>Membranes</b>	<b>A (L m<sup>-2</sup> h<sup>-1</sup>)</b>	<b>B (L m<sup>-2</sup> h<sup>-1</sup>)</b>	<b>S (μm)</b>
<i>d</i> -Ti <sub>3</sub> C <sub>2</sub> T <sub>x</sub> -45	7.76	17.47	57.0 ± 2.1
CTA	1.09	1.06	476.1 ± 10.5

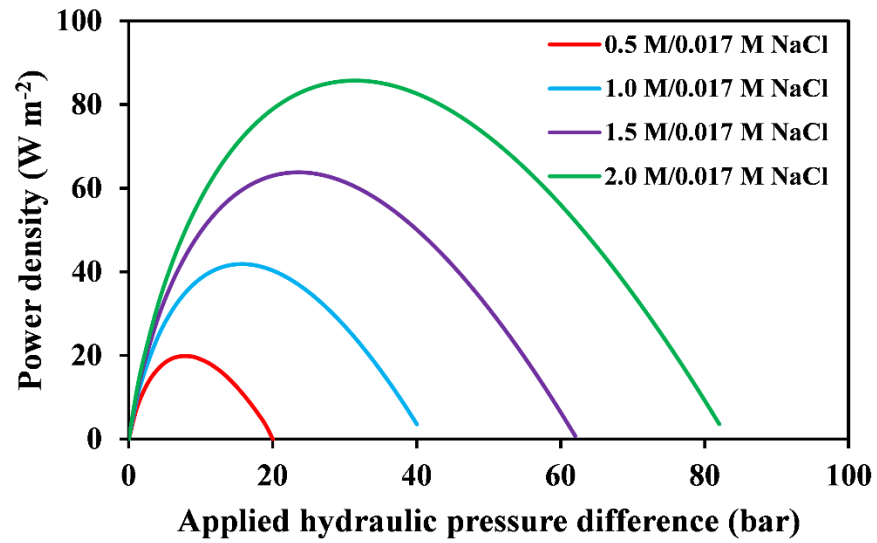


**Figure 38 - The theoretical power density as a function of applied hydraulic pressure difference.**

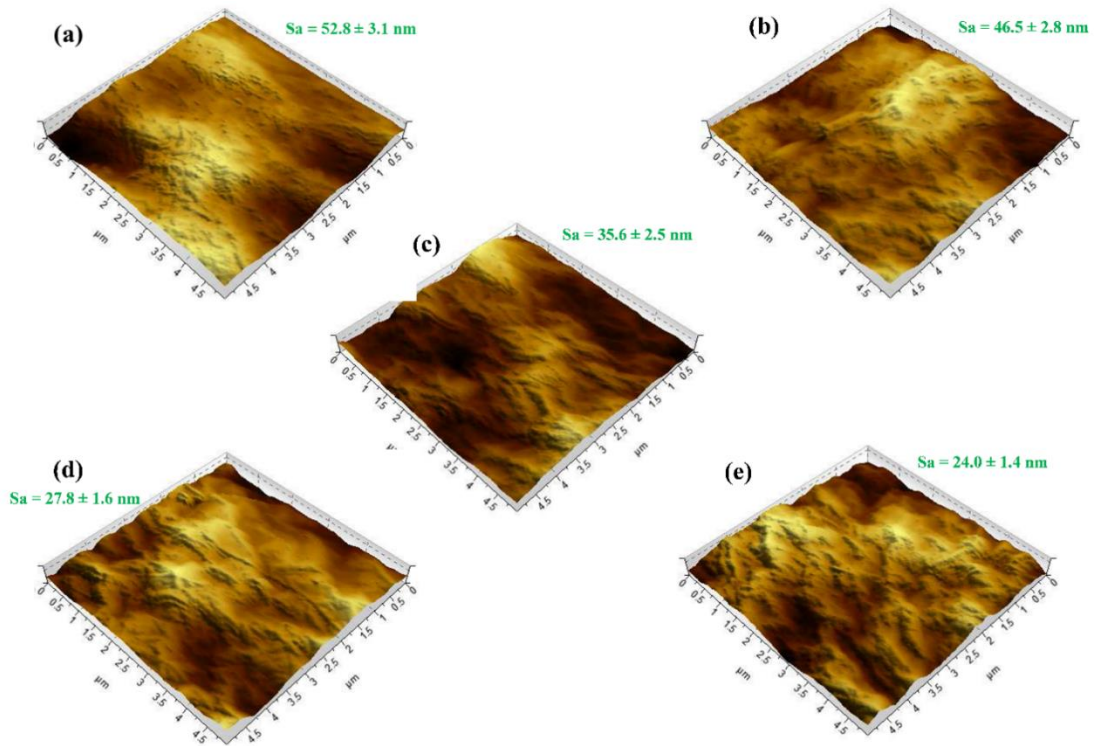


**Figure 39 - AFM images of membrane surface roughness (a) *d*-Ti<sub>3</sub>C<sub>2</sub>Tx/GO-0, (b) *d*-Ti<sub>3</sub>C<sub>2</sub>Tx/GO-15, (c) *d*-Ti<sub>3</sub>C<sub>2</sub>Tx/GO-25, (d) *d*-Ti<sub>3</sub>C<sub>2</sub>Tx/GO-45, and (e) *d*-Ti<sub>3</sub>C<sub>2</sub>Tx/GO-60.**

## REFERENCES

- [1] A. Evans, V. Strezov, T.J. Evans, Assessment of sustainability indicators for renewable energy technologies, *Renewable and Sustainable Energy Reviews*, 13 (2009) 1082-1088.
- [2] R. Pattle, Production of electric power by mixing fresh and salt water in the hydroelectric pile, *Nature*, 174 (1954) 660.
- [3] N.Y. Yip, M. Elimelech, Thermodynamic and energy efficiency analysis of power generation from natural salinity gradients by pressure retarded osmosis, *Environmental science & technology*, 46 (2012) 5230-5239.
- [4] T. Thorsen, T. Holt, The potential for power production from salinity gradients by pressure retarded osmosis, *Journal of Membrane Science*, 335 (2009) 103-110.
- [5] S. Loeb, F. Van Hessen, D. Shahaf, Production of energy from concentrated brines by pressure-retarded osmosis: II. Experimental results and projected energy costs, *Journal of Membrane Science*, 1 (1976) 249-269.
- [6] T.-S. Chung, L. Luo, C.F. Wan, Y. Cui, G. Amy, What is next for forward osmosis (FO) and pressure retarded osmosis (PRO), *Separation and Purification Technology*, 156 (2015) 856-860.
- [7] D.I. Kim, J. Kim, H.K. Shon, S. Hong, Pressure retarded osmosis (PRO) for integrating seawater desalination and wastewater reclamation: energy consumption and fouling, *Journal of membrane science*, 483 (2015) 34-41.
- [8] K. Saito, M. Irie, S. Zaitso, H. Sakai, H. Hayashi, A. Tanioka, Power generation with salinity gradient by pressure retarded osmosis using concentrated brine from SWRO system and treated sewage as pure water, *Desalination and Water Treatment*, 41 (2012) 114-121.
- [9] B.E. Logan, M. Elimelech, Membrane-based processes for sustainable power generation using water, *Nature*, 488 (2012) 313.
- [10] A. Achilli, T.Y. Cath, A.E. Childress, Power generation with pressure retarded osmosis: An experimental and theoretical investigation, *Journal of membrane science*, 343 (2009) 42-52.
- [11] T. Xu, W. Yang, B. He, The insulator-to-conductor transition in sulphonated poly (phenylene oxide) polymer membranes: Percolation theory approach, *Chinese Journal of Chemical Engineering*, 6 (1998) 283-289.

- [12] J.N. Weinstein, F.B. Leitz, Electric Power from Differences in Salinity: The Dialytic Battery, *Science*, 191 (1976) 557-559.
- [13] J.W. Post, H.V.M. Hamelers, C.J.N. Buisman, Energy Recovery from Controlled Mixing Salt and Fresh Water with a Reverse Electrodialysis System, *Environmental Science & Technology*, 42 (2008) 5785-5790.
- [14] S. Loeb, R.S. Norman, Osmotic Power Plants, *Science*, 189 (1975) 654-655.
- [15] A. Achilli, A.E. Childress, Pressure retarded osmosis: from the vision of Sidney Loeb to the first prototype installation, *Desalination*, 261 (2010) 205-211.
- [16] D. Brogioli, Extracting renewable energy from a salinity difference using a capacitor, *Physical review letters*, 103 (2009) 058501.
- [17] F. La Mantia, M. Pasta, H.D. Deshazer, B.E. Logan, Y. Cui, Batteries for efficient energy extraction from a water salinity difference, *Nano letters*, 11 (2011) 1810-1813.
- [18] A. Siria, P. Poncharal, A.-L. Bianco, R. Fulcrand, X. Blase, S.T. Purcell, L. Bocquet, Giant osmotic energy conversion measured in a single transmembrane boron nitride nanotube, *Nature*, 494 (2013) 455.
- [19] N.Y. Yip, M. Elimelech, Comparison of Energy Efficiency and Power Density in Pressure Retarded Osmosis and Reverse Electrodialysis, *Environmental Science & Technology*, 48 (2014) 11002-11012.
- [20] R.E. Pattle, Production of Electric Power by mixing Fresh and Salt Water in the Hydroelectric Pile, *Nature*, 174 (1954) 660-660.
- [21] J. Wang, P. Chen, B. Shi, W. Guo, M. Jaroniec, S.-Z. Qiao, A Regularly Channeled Lamellar Membrane for Unparalleled Water and Organics Permeation, *Angewandte Chemie International Edition*, 57 (2018) 6814-6818.
- [22] J. Veerman, J. Post, M. Saakes, S. Metz, G. Harmsen, Reducing power losses caused by ionic shortcut currents in reverse electrodialysis stacks by a validated model, *Journal of Membrane Science*, 310 (2008) 418-430.
- [23] P. Długołęcki, A. Gambier, K. Nijmeijer, M. Wessling, Practical potential of reverse electrodialysis as process for sustainable energy generation, *Environmental science & technology*, 43 (2009) 6888-6894.
- [24] D.A. Vermaas, M. Saakes, K. Nijmeijer, Doubled power density from salinity gradients at reduced intermembrane distance, *Environmental science & technology*, 45 (2011) 7089-7095.
- [25] G.M. Geise, A.J. Curtis, M.C. Hatzell, M.A. Hickner, B.E. Logan, Salt concentration differences alter membrane resistance in reverse electrodialysis stacks, *Environmental Science & Technology Letters*, 1 (2013) 36-39.

- [26] B. Zhang, J.G. Hong, S. Xie, S. Xia, Y. Chen, An integrative modeling and experimental study on the ionic resistance of ion-exchange membranes, *Journal of Membrane Science*, 524 (2017) 362-369.
- [27] D.A. Vermaas, M. Saakes, K. Nijmeijer, Power generation using profiled membranes in reverse electrodialysis, *Journal of Membrane Science*, 385–386 (2011) 234-242.
- [28] D.A. Vermaas, J. Veerman, M. Saakes, K. Nijmeijer, Influence of multivalent ions on renewable energy generation in reverse electrodialysis, *Energy & Environmental Science*, 7 (2014) 1434-1445.
- [29] J.W. Post, H.V.M. Hamelers, C.J.N. Buisman, Influence of multivalent ions on power production from mixing salt and fresh water with a reverse electrodialysis system, *Journal of Membrane Science*, 330 (2009) 65-72.
- [30] E. Fontananova, D. Messina, R.A. Tufa, I. Nicotera, V. Kosma, E. Curcio, W. van Baak, E. Drioli, G. Di Profio, Effect of solution concentration and composition on the electrochemical properties of ion exchange membranes for energy conversion, *Journal of Power Sources*, 340 (2017) 282-293.
- [31] A.H. Avci, P. Sarkar, R.A. Tufa, D. Messina, P. Argurio, E. Fontananova, G. Di Profio, E. Curcio, Effect of  $Mg^{2+}$  ions on energy generation by Reverse Electrodialysis, *Journal of Membrane Science*, 520 (2016) 499-506.
- [32] D.A. Vermaas, D. Kunteng, M. Saakes, K. Nijmeijer, Fouling in reverse electrodialysis under natural conditions, *Water Research*, 47 (2013) 1289-1298.
- [33] H. Susanto, M. Fitrianingtyas, A.M. Samsudin, A. Syakur, Experimental study of the natural organic matters effect on the power generation of reverse electrodialysis, *International Journal of Energy Research*, (2017) n/a-n/a.
- [34] G.Z. Ramon, B.J. Feinberg, E.M. Hoek, Membrane-based production of salinity-gradient power, *Energy & environmental science*, 4 (2011) 4423-4434.
- [35] N.Y. Yip, A. Tiraferri, W.A. Phillip, J.D. Schiffman, L.A. Hoover, Y.C. Kim, M. Elimelech, Thin-Film Composite Pressure Retarded Osmosis Membranes for Sustainable Power Generation from Salinity Gradients, *Environmental Science & Technology*, 45 (2011) 4360-4369.
- [36] A. Tiraferri, N.Y. Yip, W.A. Phillip, J.D. Schiffman, M. Elimelech, Relating performance of thin-film composite forward osmosis membranes to support layer formation and structure, *Journal of membrane science*, 367 (2011) 340-352.
- [37] G. Han, S. Zhang, X. Li, T.-S. Chung, Progress in pressure retarded osmosis (PRO) membranes for osmotic power generation, *Progress in Polymer science*, 51 (2015) 1-27.

- [38] S.-P. Sun, T.-S. Chung, Outer-selective pressure-retarded osmosis hollow fiber membranes from vacuum-assisted interfacial polymerization for osmotic power generation, *Environmental science & technology*, 47 (2013) 13167-13174.
- [39] S. Chou, R. Wang, L. Shi, Q. She, C. Tang, A.G. Fane, Thin-film composite hollow fiber membranes for pressure retarded osmosis (PRO) process with high power density, *Journal of membrane science*, 389 (2012) 25-33.
- [40] N.-N. Bui, J.R. McCutcheon, Nanofiber supported thin-film composite membrane for pressure-retarded osmosis, *Environmental science & technology*, 48 (2014) 4129-4136.
- [41] P.G. Ingole, W. Choi, K.H. Kim, C.H. Park, W.K. Choi, H.K. Lee, Synthesis, characterization and surface modification of PES hollow fiber membrane support with polydopamine and thin film composite for energy generation, *Chemical Engineering Journal*, 243 (2014) 137-146.
- [42] N.Y. Yip, A. Tiraferri, W.A. Phillip, J.D. Schiffman, M. Elimelech, High performance thin-film composite forward osmosis membrane, *Environmental science & technology*, 44 (2010) 3812-3818.
- [43] X. Song, Z. Liu, D.D. Sun, Nano Gives the Answer: Breaking the Bottleneck of Internal Concentration Polarization with a Nanofiber Composite Forward Osmosis Membrane for a High Water Production Rate, *Advanced Materials*, 23 (2011) 3256-3260.
- [44] A. Achilli, A.E. Childress, Pressure retarded osmosis: From the vision of Sidney Loeb to the first prototype installation — Review, *Desalination*, 261 (2010) 205-211.
- [45] W.R. Thelin, E. Sivertsen, T. Holt, G. Brekke, Natural organic matter fouling in pressure retarded osmosis, *Journal of membrane science*, 438 (2013) 46-56.
- [46] Y. Liu, B. Mi, Combined fouling of forward osmosis membranes: Synergistic foulant interaction and direct observation of fouling layer formation, *Journal of membrane science*, 407 (2012) 136-144.
- [47] Y. Kim, M. Elimelech, H.K. Shon, S. Hong, Combined organic and colloidal fouling in forward osmosis: Fouling reversibility and the role of applied pressure, *Journal of Membrane Science*, 460 (2014) 206-212.
- [48] G. Han, Z.L. Cheng, T.-S. Chung, Thin-film composite (TFC) hollow fiber membrane with double-polyamide active layers for internal concentration polarization and fouling mitigation in osmotic processes, *Journal of Membrane Science*, 523 (2017) 497-504.
- [49] X. Li, T. Cai, T.-S. Chung, Anti-fouling behavior of hyperbranched polyglycerol-grafted poly (ether sulfone) hollow fiber membranes for osmotic power generation, *Environmental science & technology*, 48 (2014) 9898-9907.

- [50] M. Hu, S. Zheng, B. Mi, Organic fouling of graphene oxide membranes and its implications for membrane fouling control in engineered osmosis, *Environmental science & technology*, 50 (2016) 685-693.
- [51] J.Y. Xiong, Z.L. Cheng, C.F. Wan, S.C. Chen, T.-S. Chung, Analysis of flux reduction behaviors of PRO hollow fiber membranes: experiments, mechanisms, and implications, *Journal of membrane science*, 505 (2016) 1-14.
- [52] P. Dlugolecki, K. Nymeijer, S. Metz, M. Wessling, Current status of ion exchange membranes for power generation from salinity gradients, *Journal of Membrane Science*, 319 (2008) 214-222.
- [53] J.G. Hong, B. Zhang, S. Glabman, N. Uzal, X. Dou, H. Zhang, X. Wei, Y. Chen, Potential ion exchange membranes and system performance in reverse electro dialysis for power generation: A review, *Journal of Membrane Science*, 486 (2015) 71-88.
- [54] T. Sata, Studies on anion exchange membranes having permselectivity for specific anions in electro dialysis — effect of hydrophilicity of anion exchange membranes on permselectivity of anions, *J Membrane Sci*, 167 (2000) 1-31.
- [55] H. Strathmann, Electro dialysis, a mature technology with a multitude of new applications, *Desalination*, 264 (2010) 268-288.
- [56] X.F. Li, H.M. Zhang, Z.S. Mai, H.Z. Zhang, I. Vankelecom, Ion exchange membranes for vanadium redox flow battery (VRB) applications, *Energy & Environmental Science*, 4 (2011) 1147-1160.
- [57] W. Wang, Q.T. Luo, B. Li, X.L. Wei, L.Y. Li, Z.G. Yang, Recent Progress in Redox Flow Battery Research and Development, *Advanced Functional Materials*, 23 (2013) 970-986.
- [58] P. Dlugolecki, B. Anet, S.J. Metz, K. Nijmeijer, M. Wessling, Transport limitations in ion exchange membranes at low salt concentrations, *Journal of Membrane Science*, 346 (2010) 163-171.
- [59] B.E. Logan, M. Elimelech, Membrane-based processes for sustainable power generation using water, *Nature*, 488 (2012) 313-319.
- [60] H. Strathmann, A. Grabowski, G. Eigenberger, Ion-Exchange Membranes in the Chemical Process Industry, *Industrial & Engineering Chemistry Research*, 52 (2013) 10364-10379.
- [61] N.Y. Yip, D.A. Vermaas, K. Nijmeijer, M. Elimelech, Thermodynamic, Energy Efficiency, and Power Density Analysis of Reverse Electro dialysis Power Generation with Natural Salinity Gradients, *Environ Sci Technol*, 48 (2014) 4925-4936.

- [62] T. Xu, W.H. Yang, B.L. He, Ionic conductivity threshold in sulfonated poly (phenylene oxide) matrices: a combination of three-phase model and percolation theory, *Chemical Engineering Science*, 56 (2001) 5343-5350.
- [63] V.I. Zabolotsky, V.V. Nikonenko, Effect of Structural Membrane Inhomogeneity on Transport-Properties, *Journal of Membrane Science*, 79 (1993) 181-198.
- [64] G.M. Geise, M.A. Hickner, B.E. Logan, Ionic Resistance and Permselectivity Tradeoffs in Anion Exchange Membranes, *Acs Appl Mater Inter*, 5 (2013) 10294-10301.
- [65] W.Y. Hsu, J.R. Barkley, P. Meakin, Ion percolation and insulator-to-conductor transition in Nafion perfluorosulfonic acid membranes, *Macromolecules*, 13 (1980) 198-200.
- [66] L.V. Karpenko-Jereb, N.P. Berezina, Determination of structural, selective, electrokinetic and percolation characteristics of ion-exchange membranes from conductive data, *Desalination*, 245 (2009) 587-596.
- [67] V.I. Zabolotsky, V.V. Nikonenko, Effect of structural membrane inhomogeneity on transport properties, *Journal of Membrane Science*, 79 (1993) 181-198.
- [68] T. Sata, *Ion exchange membranes: preparation, characterization, modification and application*, Royal Society of chemistry, 2007.
- [69] R.G. Larson, L.E. Scriven, H.T. Davis, Percolation Theory of Residual Phases in Porous-Media, *Nature*, 268 (1977) 409-413.
- [70] P. Dean, A New Monte Carlo Method for Percolation Problems on a Lattice, *P Camb Philos Soc*, 59 (1963) 397-&.
- [71] P. Sotta, D. Long, The crossover from 2D to 3D percolation: Theory and numerical simulations, *Eur Phys J E*, 11 (2003) 375-387.
- [72] A. Sur, J.L. Lebowitz, J. Marro, M.H. Kalos, S. Kirkpatrick, Monte-Carlo Studies of Percolation Phenomena for a Simple Cubic Lattice, *J Stat Phys*, 15 (1976) 345-353.
- [73] H. Strathmann, ScienceDirect (Online service), Ion-exchange membrane separation processes, in: *Membrane science and technology series*, Elsevier, Amsterdam ; Boston, 2004, pp. xi, 348 p.
- [74] X. Tong, B. Zhang, Y. Fan, Y. Chen, Mechanism Exploration of Ion Transport in Nanocomposite Cation Exchange Membranes, *ACS Applied Materials & Interfaces*, 9 (2017) 13491-13499.
- [75] H. Gao, B. Zhang, X. Tong, Y. Chen, Monovalent-anion selective and antifouling polyelectrolytes multilayer anion exchange membrane for reverse electrodialysis, *Journal of Membrane Science*, 567 (2018) 68-75.

- [76] N.P. Berezina, N.A. Kononenko, O.A. Dyomina, N.P. Gnusin, Characterization of ion-exchange membrane materials: Properties vs structure, *Adv Colloid Interfac*, 139 (2008) 3-28.
- [77] M.A. Mohammad, A. Alhalaweh, S.P. Velaga, Hansen solubility parameter as a tool to predict cocrystal formation, *International journal of pharmaceutics*, 407 (2011) 63-71.
- [78] R. Guan, H. Dai, C. Li, J. Liu, J. Xu, Effect of casting solvent on the morphology and performance of sulfonated polyethersulfone membranes, *Journal of Membrane Science*, 277 (2006) 148-156.
- [79] C. Gong, R. Guan, Y.-C. Shu, F.-S. Chuang, W.-C. Tsen, Effect of sulfonic group on solubility parameters and solubility behavior of poly(2,6-dimethyl-1,4-phenylene oxide), *Polymers for Advanced Technologies*, 18 (2007) 44-49.
- [80] C.M. Hansen, A.L. Smith, Using Hansen solubility parameters to correlate solubility of C60 fullerene in organic solvents and in polymers, *Carbon*, 42 (2004) 1591-1597.
- [81] F. Gharagheizi, New procedure to calculate the Hansen solubility parameters of polymers, *Journal of applied polymer science*, 103 (2007) 31-36.
- [82] R. Guan, H. Dai, C.H. Li, J.H. Liu, J. Xu, Effect of casting solvent on the morphology and performance of sulfonated polyethersulfone membranes, *J Membrane Sci*, 277 (2006) 148-156.
- [83] B.P. Zhang, J.G. Hong, S.H. Xie, S.M. Xia, Y.S. Chen, An integrative modeling and experimental study on the ionic resistance of ion-exchange membranes, *Journal of Membrane Science*, 524 (2017) 362-369.
- [84] G.L. Wick, W.R. Schmitt, PROSPECTS FOR RENEWABLE ENERGY FROM THE SEA, *Marine Technology Society Journal*, 11 (1977) 16-21.
- [85] G.Z. Ramon, B.J. Feinberg, E.M.V. Hoek, Membrane-based production of salinity-gradient power, *Energy & Environmental Science*, 4 (2011) 4423-4434.
- [86] R.S. Norman, Water Salination: A Source of Energy, *Science*, 186 (1974) 350-352.
- [87] J.D. Isaacs, R.J. Seymour, The ocean as a power resource, *International Journal of Environmental Studies*, 4 (1973) 201-205.
- [88] International Energy Outlook 2017, <https://www.eia.gov/outlooks/ieo/>, (2017).
- [89] R.E. Lacey, Energy by reverse electrodialysis, *Ocean Engineering*, 7 (1980) 1-47.
- [90] S.J. Klaine, P.J.J. Alvarez, G.E. Batley, T.F. Fernandes, R.D. Handy, D.Y. Lyon, S. Mahendra, M.J. McLaughlin, J.R. Lead, Nanomaterials in the environment: Behavior, fate, bioavailability, and effects, *Environmental Toxicology and Chemistry*, 27 (2008) 1825-1851.

- [91] B. Tansel, Significance of thermodynamic and physical characteristics on permeation of ions during membrane separation: Hydrated radius, hydration free energy and viscous effects, *Separation and Purification Technology*, 86 (2012) 119-126.
- [92] T. Sata, T. Yamaguchi, K. Matsusaki, Interaction between anionic polyelectrolytes and anion exchange membranes and change in membrane properties, *Journal of Membrane Science*, 100 (1995) 229-238.
- [93] M. Vasselbehagh, H. Karkhanechi, S. Mulyati, R. Takagi, H. Matsuyama, Improved antifouling of anion-exchange membrane by polydopamine coating in electro dialysis process, *Desalination*, 332 (2014) 126-133.
- [94] E. Güler, W. van Baak, M. Saakes, K. Nijmeijer, Monovalent-ion-selective membranes for reverse electro dialysis, *Journal of Membrane Science*, 455 (2014) 254-270.
- [95] S. Mulyati, R. Takagi, A. Fujii, Y. Ohmukai, T. Maruyama, H. Matsuyama, Improvement of the antifouling potential of an anion exchange membrane by surface modification with a polyelectrolyte for an electro dialysis process, *Journal of Membrane Science*, 417–418 (2012) 137-143.
- [96] S. Mulyati, R. Takagi, A. Fujii, Y. Ohmukai, H. Matsuyama, Simultaneous improvement of the monovalent anion selectivity and antifouling properties of an anion exchange membrane in an electro dialysis process, using polyelectrolyte multilayer deposition, *Journal of Membrane Science*, 431 (2013) 113-120.
- [97] L. Hou, J. Pan, D. Yu, B. Wu, A.N. Mondal, Q. Li, L. Ge, T. Xu, Nanofibrous composite membranes (NFCMs) for mono/divalent cations separation, *Journal of Membrane Science*, 528 (2017) 243-250.
- [98] J.J. Richardson, M. Björnmalm, F. Caruso, Technology-driven layer-by-layer assembly of nanofilms, *Science*, 348 (2015).
- [99] Y. Wang, S. Wang, M. Xiao, D. Han, M.A. Hickner, Y. Meng, Layer-by-layer self-assembly of PDDA/PSS-SPFEK composite membrane with low vanadium permeability for vanadium redox flow battery, *RSC Advances*, 3 (2013) 15467-15474.
- [100] S. Abdu, M.-C. Martí-Calatayud, J.E. Wong, M. García-Gabaldón, M. Wessling, Layer-by-Layer Modification of Cation Exchange Membranes Controls Ion Selectivity and Water Splitting, *ACS Applied Materials & Interfaces*, 6 (2014) 1843-1854.
- [101] N. White, M. Misovich, A. Yaroshchuk, M.L. Bruening, Coating of Nafion Membranes with Polyelectrolyte Multilayers to Achieve High Monovalent/Divalent Cation Electro dialysis Selectivities, *ACS Applied Materials & Interfaces*, 7 (2015) 6620-6628.
- [102] Y. Xue, S. Chan, Layer-by-layer self-assembly of CHI/PVS–Nafion composite membrane for reduced methanol crossover and enhanced DMFC performance, *International Journal of Hydrogen Energy*, 40 (2015) 1877-1885.

- [103] P. Zhang, J. Qian, Y. Yang, Q. An, X. Liu, Z. Gui, Polyelectrolyte layer-by-layer self-assembly enhanced by electric field and their multilayer membranes for separating isopropanol–water mixtures, *Journal of Membrane Science*, 320 (2008) 73-77.
- [104] Y. Zhao, J. Zhu, J. Ding, B. Van der Bruggen, J. Shen, C. Gao, Electric-pulse layer-by-layer assembled of anion exchange membrane with enhanced monovalent selectivity, *Journal of Membrane Science*, 548 (2018) 81-90.
- [105] T. Sata, T. Sata, W. Yang, Studies on cation-exchange membranes having permselectivity between cations in electrodialysis, *Journal of Membrane Science*, 206 (2002) 31-60.
- [106] H.-J. Lee, M.-K. Hong, S.-D. Han, J. Shim, S.-H. Moon, Analysis of fouling potential in the electrodialysis process in the presence of an anionic surfactant foulant, *Journal of Membrane Science*, 325 (2008) 719-726.
- [107] B. Zhang, H. Gao, Y. Chen, Enhanced Ionic Conductivity and Power Generation Using Ion-Exchange Resin Beads in a Reverse-Electrodialysis Stack, *Environmental Science & Technology*, 49 (2015) 14717-14724.
- [108] J.B. Schlenoff, S.T. Dubas, Mechanism of Polyelectrolyte Multilayer Growth: Charge Overcompensation and Distribution, *Macromolecules*, 34 (2001) 592-598.
- [109] Y. Zhao, K. Tang, H. Liu, B. Van der Bruggen, A. Sotto Díaz, J. Shen, C. Gao, An anion exchange membrane modified by alternate electro-deposition layers with enhanced monovalent selectivity, *Journal of Membrane Science*, 520 (2016) 262-271.
- [110] S.M. Hosseini, S.S. Madaeni, A.R. Khodabakhshi, The Electrochemical Characterization of Ion Exchange Membranes in Different Electrolytic Environments: Investigation of Concentration and pH Effects, *Separation Science and Technology*, 47 (2012) 455-462.
- [111] N. Dizge, R. Epsztein, W. Cheng, C.J. Porter, M. Elimelech, Biocatalytic and salt selective multilayer polyelectrolyte nanofiltration membrane, *Journal of Membrane Science*, 549 (2018) 357-365.
- [112] G. Decher, Fuzzy Nanoassemblies: Toward Layered Polymeric Multicomposites, *Science*, 277 (1997) 1232-1237.
- [113] L. Ouyang, R. Malaisamy, M.L. Bruening, Multilayer polyelectrolyte films as nanofiltration membranes for separating monovalent and divalent cations, *Journal of Membrane Science*, 310 (2008) 76-84.
- [114] E. Guler, Y. Zhang, M. Saakes, K. Nijmeijer, Tailor-Made Anion-Exchange Membranes for Salinity Gradient Power Generation Using Reverse Electrodialysis, *ChemSusChem*, 5 (2012) 2262-2270.

- [115] X. Tong, B. Zhang, Y. Chen, Fouling resistant nanocomposite cation exchange membrane with enhanced power generation for reverse electrodialysis, *Journal of Membrane Science*, 516 (2016) 162-171.
- [116] L. Krasemann, B. Tieke, Selective Ion Transport across Self-Assembled Alternating Multilayers of Cationic and Anionic Polyelectrolytes, *Langmuir*, 16 (2000) 287-290.
- [117] M.R. Teixeira, M.J. Rosa, M. Nyström, The role of membrane charge on nanofiltration performance, *Journal of Membrane Science*, 265 (2005) 160-166.
- [118] G. Saracco, M.C. Zanetti, Ion transport through monovalent-anion-permselective membranes, *Industrial & engineering chemistry research*, 33 (1994) 96-101.
- [119] V. Vatanpour, S.S. Madaeni, R. Moradian, S. Zinadini, B. Astinchap, Fabrication and characterization of novel antifouling nanofiltration membrane prepared from oxidized multiwalled carbon nanotube/polyethersulfone nanocomposite, *Journal of Membrane Science*, 375 (2011) 284-294.
- [120] M.S. Rahaman, H. Therien-Aubin, M. Ben-Sasson, C.K. Ober, M. Nielsen, M. Elimelech, Control of biofouling on reverse osmosis polyamide membranes modified with biocidal nanoparticles and antifouling polymer brushes, *Journal of Materials Chemistry B*, 2 (2014) 1724-1732.
- [121] E.M. Vrijenhoek, S. Hong, M. Elimelech, Influence of membrane surface properties on initial rate of colloidal fouling of reverse osmosis and nanofiltration membranes, *Journal of Membrane Science*, 188 (2001) 115-128.
- [122] V. Lindstrand, G. Sundström, A.-S. Jönsson, Fouling of electrodialysis membranes by organic substances, *Desalination*, 128 (2000) 91-102.
- [123] D.-K. Kim, C. Duan, Y.-F. Chen, A. Majumdar, Power generation from concentration gradient by reverse electrodialysis in ion-selective nanochannels, *Microfluidics and Nanofluidics*, 9 (2010) 1215-1224.
- [124] S. Lee, H. Kim, D.-K. Kim, Power Generation from Concentration Gradient by Reverse Electrodialysis in Dense Silica Membranes for Microfluidic and Nanofluidic Systems, *Energies*, 9 (2016) 49.
- [125] N.Y. Yip, M. Elimelech, Performance limiting effects in power generation from salinity gradients by pressure retarded osmosis, *Environmental science & technology*, 45 (2011) 10273-10282.
- [126] O. Ellabban, H. Abu-Rub, F. Blaabjerg, Renewable energy resources: Current status, future prospects and their enabling technology, *Renewable and Sustainable Energy Reviews*, 39 (2014) 748-764.
- [127] G.L. Wick, Power from salinity gradients, *Energy*, 3 (1978) 95-100.

- [128] J.W. Post, J. Veerman, H.V.M. Hamelers, G.J.W. Euverink, S.J. Metz, K. Nymeijer, C.J.N. Buisman, Salinity-gradient power: Evaluation of pressure-retarded osmosis and reverse electrodialysis, *Journal of Membrane Science*, 288 (2007) 218-230.
- [129] A. Achilli, J.L. Prante, N.T. Hancock, E.B. Maxwell, A.E. Childress, Experimental results from RO-PRO: a next generation system for low-energy desalination, *Environmental Science & Technology*, 48 (2014) 6437-6443.
- [130] A.P. Straub, A. Deshmukh, M. Elimelech, Pressure-retarded osmosis for power generation from salinity gradients: is it viable?, *Energy & Environmental Science*, 9 (2016) 31-48.
- [131] K. Lee, R. Baker, H. Lonsdale, Membranes for power generation by pressure-retarded osmosis, *Journal of Membrane Science*, 8 (1981) 141-171.
- [132] M. Li, V. Karanikola, X. Zhang, L. Wang, M. Elimelech, A self-standing, support-free membrane for forward osmosis with no internal concentration polarization, *Environmental Science & Technology Letters*, 5 (2018) 266-271.
- [133] E. Bar-Zeev, F.o. Perreault, A.P. Straub, M. Elimelech, Impaired performance of pressure-retarded osmosis due to irreversible biofouling, *Environmental science & technology*, 49 (2015) 13050-13058.
- [134] G. Han, J. Zhou, C. Wan, T. Yang, T.-S. Chung, Investigations of inorganic and organic fouling behaviors, antifouling and cleaning strategies for pressure retarded osmosis (PRO) membrane using seawater desalination brine and wastewater, *Water research*, 103 (2016) 264-275.
- [135] C.Y. Tang, Q. She, W.C. Lay, R. Wang, A.G. Fane, Coupled effects of internal concentration polarization and fouling on flux behavior of forward osmosis membranes during humic acid filtration, *Journal of membrane science*, 354 (2010) 123-133.
- [136] N.Y. Yip, M. Elimelech, Influence of natural organic matter fouling and osmotic backwash on pressure retarded osmosis energy production from natural salinity gradients, *Environmental science & technology*, 47 (2013) 12607-12616.
- [137] H.-C. Flemming, J. Wingender, The biofilm matrix, *Nature reviews microbiology*, 8 (2010) 623.
- [138] R.K. Joshi, P. Carbone, F.C. Wang, V.G. Kravets, Y. Su, I.V. Grigorieva, H.A. Wu, A.K. Geim, R.R. Nair, Precise and Ultrafast Molecular Sieving Through Graphene Oxide Membranes, *Science*, 343 (2014) 752-754.
- [139] B. Mi, Graphene oxide membranes for ionic and molecular sieving, *Science*, 343 (2014) 740-742.

- [140] M. Naguib, M. Kurtoglu, V. Presser, J. Lu, J. Niu, M. Heon, L. Hultman, Y. Gogotsi, M.W. Barsoum, Two - dimensional nanocrystals produced by exfoliation of  $Ti_3AlC_2$ , *Advanced Materials*, 23 (2011) 4248-4253.
- [141] M. Alhabeab, K. Maleski, B. Anasori, P. Lelyukh, L. Clark, S. Sin, Y. Gogotsi, Guidelines for Synthesis and Processing of Two-Dimensional Titanium Carbide ( $Ti_3C_2T_x$  MXene), *Chemistry of Materials*, 29 (2017) 7633-7644.
- [142] L. Ding, Y. Wei, Y. Wang, H. Chen, J. Caro, H. Wang, A Two-Dimensional Lamellar Membrane: MXene Nanosheet Stacks, *Angewandte Chemie International Edition*, 56 (2017) 1825-1829.
- [143] X. Tong, X. Wang, S. Liu, H. Gao, C. Xu, J. Crittenden, Y. Chen, A freestanding graphene oxide membrane for efficiently harvesting salinity gradient power, *Carbon*, 138 (2018) 410-418.
- [144] E. Pomerantseva, Y. Gogotsi, Two-dimensional heterostructures for energy storage, *Nature Energy*, 2 (2017) 17089.
- [145] M.-Q. Zhao, N. Trainor, C.E. Ren, M. Torelli, B. Anasori, Y. Gogotsi, Scalable Manufacturing of Large and Flexible Sheets of MXene/Graphene Heterostructures, *Advanced Materials Technologies*, 4 (2019) 1800639.
- [146] M. Ghidui, M.R. Lukatskaya, M.-Q. Zhao, Y. Gogotsi, M.W. Barsoum, Conductive two-dimensional titanium carbide 'clay' with high volumetric capacitance, *Nature*, 516 (2014) 78.
- [147] Y.C. Kim, M. Elimelech, Adverse impact of feed channel spacers on the performance of pressure retarded osmosis, *Environmental science & technology*, 46 (2012) 4673-4681.
- [148] T.Y. Cath, A.E. Childress, M. Elimelech, Forward osmosis: principles, applications, and recent developments, *Journal of membrane science*, 281 (2006) 70-87.
- [149] A. Deshmukh, N.Y. Yip, S. Lin, M. Elimelech, Desalination by forward osmosis: Identifying performance limiting parameters through module-scale modeling, *Journal of membrane science*, 491 (2015) 159-167.
- [150] S. Loeb, L. Titelman, E. Korngold, J. Freiman, Effect of porous support fabric on osmosis through a Loeb-Sourirajan type asymmetric membrane, *Journal of Membrane Science*, 129 (1997) 243-249.
- [151] L. Bai, Y. Liu, N. Bossa, A. Ding, N. Ren, G. Li, H. Liang, M.R. Wiesner, Incorporation of Cellulose Nanocrystals (CNCs) into the Polyamide Layer of Thin-Film Composite (TFC) Nanofiltration Membranes for Enhanced Separation Performance and Antifouling Properties, *Environmental science & technology*, 52 (2018) 11178-11187.
- [152] C. Liang, Z.-S. Wang, C.J. Bruell, Influence of pH on persulfate oxidation of TCE at ambient temperatures, *Chemosphere*, 66 (2007) 106-113.

- [153] J. Shen, G. Liu, K. Huang, W. Jin, K.R. Lee, N. Xu, Membranes with fast and selective gas - transport channels of laminar graphene oxide for efficient CO<sub>2</sub> capture, *Angewandte Chemie*, 127 (2015) 588-592.
- [154] L. Ding, Y. Wei, L. Li, T. Zhang, H. Wang, J. Xue, L.-X. Ding, S. Wang, J. Caro, Y. Gogotsi, MXene molecular sieving membranes for highly efficient gas separation, *Nature Communications*, 9 (2018) 155.
- [155] W.-T. Cao, F.-F. Chen, Y.-J. Zhu, Y.-G. Zhang, Y.-Y. Jiang, M.-G. Ma, F. Chen, Binary strengthening and toughening of MXene/cellulose nanofiber composite paper with nacre-inspired structure and superior electromagnetic interference shielding properties, *ACS nano*, 12 (2018) 4583-4593.
- [156] C.E. Ren, K.B. Hatzell, M. Alhabeab, Z. Ling, K.A. Mahmoud, Y. Gogotsi, Charge- and size-selective ion sieving through Ti<sub>3</sub>C<sub>2</sub>T<sub>x</sub> MXene membranes, *The journal of physical chemistry letters*, 6 (2015) 4026-4031.
- [157] W.A. Phillip, J.S. Yong, M. Elimelech, Reverse draw solute permeation in forward osmosis: modeling and experiments, *Environmental science & technology*, 44 (2010) 5170-5176.
- [158] L. Fan, Q. Zhang, Z. Yang, R. Zhang, Y.-n. Liu, M. He, Z. Jiang, Y. Su, Improving permeation and antifouling performance of polyamide nanofiltration membranes through the incorporation of arginine, *ACS applied materials & interfaces*, 9 (2017) 13577-13586.
- [159] X. Fan, Y. Liu, X. Quan, S. Chen, Highly permeable thin-film composite forward osmosis membrane based on carbon nanotube hollow fiber scaffold with electrically enhanced fouling resistance, *Environmental science & technology*, 52 (2018) 1444-1452.
- [160] K. Rasool, K.A. Mahmoud, D.J. Johnson, M. Helal, G.R. Berdiyrov, Y. Gogotsi, Efficient antibacterial membrane based on two-dimensional Ti<sub>3</sub>C<sub>2</sub>T<sub>x</sub> (MXene) nanosheets, *Scientific reports*, 7 (2017) 1598.
- [161] S. Liu, T.H. Zeng, M. Hofmann, E. Burcombe, J. Wei, R. Jiang, J. Kong, Y. Chen, Antibacterial activity of graphite, graphite oxide, graphene oxide, and reduced graphene oxide: membrane and oxidative stress, *ACS nano*, 5 (2011) 6971-6980.
- [162] K. Rasool, M. Helal, A. Ali, C.E. Ren, Y. Gogotsi, K.A. Mahmoud, Antibacterial Activity of Ti<sub>3</sub>C<sub>2</sub>T<sub>x</sub> MXene, *ACS nano*, 10 (2016) 3674-3684.
- [163] M. Kaneda, X. Lu, W. Cheng, X. Zhou, R. Bernstein, W. Zhang, K. Kimura, M. Elimelech, Photografting Graphene Oxide to Inert Membrane Materials to Impart Antibacterial Activity, *Environmental Science & Technology Letters*, 6 (2019) 141-147.
- [164] P. Długołęcki, P. Ogonowski, S.J. Metz, M. Saakes, K. Nijmeijer, M. Wessling, On the resistances of membrane, diffusion boundary layer and double layer in ion exchange membrane transport, *Journal of Membrane Science*, 349 (2010) 369-379.

- [165] J.G. Hong, W. Zhang, J. Luo, Y. Chen, Modeling of power generation from the mixing of simulated saline and freshwater with a reverse electrodialysis system: The effect of monovalent and multivalent ions, *Applied Energy*, 110 (2013) 244-251.
- [166] L. Giorno, E. Drioli, H. Strathmann, Permselectivity of Ion-Exchange Membranes, in: E. Drioli, L. Giorno (Eds.) *Encyclopedia of Membranes*, Springer Berlin Heidelberg, Berlin, Heidelberg, 2016, pp. 1490-1493.
- [167] S.W. Lee, H.J. Kim, D.-K. Kim, Power generation from concentration gradient by reverse electrodialysis in dense silica membranes for microfluidic and nanofluidic systems, *Energies*, 9 (2016) 49.
- [168] J.R. McCutcheon, M. Elimelech, Influence of concentrative and dilutive internal concentration polarization on flux behavior in forward osmosis, *Journal of Membrane Science*, 284 (2006) 237-247.
- [169] J.R. McCutcheon, R.L. McGinnis, M. Elimelech, Desalination by ammonia–carbon dioxide forward osmosis: influence of draw and feed solution concentrations on process performance, *Journal of membrane science*, 278 (2006) 114-123.